

UNCLASSIFIED

AD 295 556

*Reproduced
by the*

**ARMED SERVICES TECHNICAL INFORMATION AGENCY
ARLINGTON HALL STATION
ARLINGTON 12, VIRGINIA**



UNCLASSIFIED

**Best
Available
Copy**

NOTICE: When government or other drawings, specifications or other data are used for any purpose other than in connection with a definitely related government procurement operation, the U. S. Government thereby incurs no responsibility, nor any obligation whatsoever; and the fact that the Government may have formulated, furnished, or in any way supplied the said drawings, specifications, or other data is not to be regarded by implication or otherwise as in any manner licensing the holder or any other person or corporation, or conveying any rights or permission to manufacture, use or sell any patented invention that may in any way be related thereto.

63-2-3

294556

AFCRL-62-515

UNIVERSITY OF PITTSBURGH
PHYSICS DEPARTMENT

CATALOGUE OF ASTIA

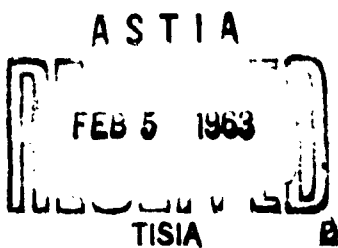
DEFECT PRODUCTION, INTERNAL FRICTION,
AND YOUNG'S MODULUS IN
DEUTERON IRRADIATED TUNGSTEN

BY D. R. MUSS

SCIENTIFIC REPORT NO. 1
CONTRACT NO. AF 19(604)-3906
ELECTRONICS RESEARCH DIRECTORATE, AFCRL

295 556

AUGUST, 1961
PITTSBURGH, PA.



AFCRL-62-515

University of Pittsburgh
Department of Physics

DEFECT PRODUCTION, INTERNAL FRICTION, AND
YOUNG'S MODULUS IN DEUTERON IRRADIATED TUNGSTEN*

by

Daniel R. Muss

December, 1961

Scientific Report No. 1

Contract No. AF19(604)-3906
Project 5620 Task 562002

Prepared for: Electronic Research Directorate
Air Force Cambridge Research Laboratories
Office of Aerospace Research
United States Air Force
Bedford, Massachusetts

Submitted to the Graduate Faculty in the Division of the Natural
Sciences in partial fulfillment of the requirements for the degree of
Doctor of Philosophy.

Requests for additional copies by Agencies of the Department of Defense, their contractors, and other Government agencies should be directed to the:

ARMED SERVICES TECHNICAL INFORMATION AGENCY
ARLINGTON HALL STATION
ARLINGTON 12, VIRGINIA

Department of Defense contractors must be established for ASTIA services or have their 'need-to-know' certified by the cognizant military agency of their project or contract.

All other persons and organizations should apply to the:

U. S. DEPARTMENT OF COMMERCE
OFFICE OF TECHNICAL SERVICES
WASHINGTON 25, D. C.

TABLE OF CONTENTS

	Page
FOREWORD	11
I. INTRODUCTION	1
A. Defect Production	1
B. Radiation Effects on the Mechanical Properties of	
Tungsten	6
1. Strain Independent Damping	7
2. Strain Dependent Damping	7
3. The Bordoni Peak	8
II. EXPERIMENTAL PROCEDURE	16
A. The Cryostat	17
B. The Irradiation Facility	18
C. Determination of Beam Flux and Energy	20
1. Measurement of Beam Flux	20
2. Uncertainty in the Beam Flux Measurement	22
3. Incident Deuteron Energy Determination	23
4. Uncertainty in the Incident Deuteron Energy	25
D. Electrical Resistance	25
1. Measurement Technique	25
2. Uncertainties in the Measurement of Electrical	
Resistance	28
3. Sample Mounting Technique for Electrical	
Measurements	28

	Page
II. Mechanical Properties	30
1. Measurement of Internal Friction and Elastic Modulus	30
2. Uncertainty in the Measurement of Internal Friction and Elastic Modulus	35
3. Temperature Measurement	38
4. Sample Mounting Technique for Mechanical Measurements	39
a. The Sample Holder	39
b. The Sample Mounting Operation	39
c. The Drive Plate	41
d. Assembly Procedure	41
III. THE ENERGY DEPENDENCE OF RADIATION DAMAGE IN TUNGSTEN	44
A. Results	44
B. Discussion of the Energy Dependence Results	48
IV. EFFECTS OF RADIATION ON THE MECHANICAL PROPERTIES OF TUNGSTEN	53
A. Results	53
1. The Pre-Irradiation Bordoni Peak	53
2. The Effect of Irradiation at 300°K on Internal Friction and Young's Modulus	54
3. Irradiation at 79°K and the Effect of Annealing on Internal Friction	55
4. The Temperature Dependence of the Resonant Frequency	56

	Page
D. Discussion	57
1. The Pre-Irradiation Bordoni Peak	58
2. The Effect of Room Temperature Irradiation on the Bordoni Peak	59
3. The Effect of Room Temperature on the Background (Strain Independent) Internal Friction	63
4. The Effect of Irradiation at 79°K on Internal Friction	65
APPENDIX A. VIBRATION OF A CANTILEVERED ROD	118
APPENDIX B. THE RELAXATION PROCESS	124
APPENDIX C. LOW TEMPERATURE VACUUM TIGHT SEALS FOR ALUMINUM FOIL TO COPPER	126
APPENDIX D. EFFECT OF AN RLC FILTER ON THE TRANSIENT SIGNAL	128
APPENDIX E. CORRECTION FOR THE ENERGY LOSS IN THE SAMPLE	131
BIBLIOGRAPHY	135

I. INTRODUCTION

The study of radiation effects in solids is a relatively new one, dating from the growth of nuclear reactor technology during and just after the second World War. Although nuclear physicists have studied the passage of high energy radiation through solids, it was always from the point of view of the bombarding ray, the target being of interest only for its stopping power. The interest in the bombarded solid was at first concerned with reactor technology. A high energy charged particle passing through a solid loses almost all its kinetic energy by ionization, i.e. collisions with orbital electrons of the host atom. Neutrons are stopped in a solid by making nuclear interactions. The charged high energy products of this interaction then lose their energy primarily by ionization. The occasional elastic coulomb collisions of the nuclear reaction products with lattice atoms, negligible as far as competing the stopping power of the solid was concerned, became important in the high neutron fluxes of reactors. Displacement of lattice atoms by radiation caused gross physical changes in reactor materials. Soon the problem of radiation damage became of interest for itself as a means of studying the solid state.

A. Defect Production

When a lattice atom, in collision with incident radiation, receives energy greater than some minimum energy (E_d) needed to remove it from its lattice site, it moves through the lattice with its residual kinetic energy. This knock-on atom will come to rest in general at an interstitial site; it becomes an interstitial defect, and leaves behind

a vacancy defect. The knock-on atom may lose its kinetic energy by creating further displacements of lattice atoms or by making collisions involving energy transfers of less than E_d . The energies of these latter collisions are carried off as phonons. It was the purpose of this work in part to study the process of defect production by bombarding tungsten with 15 mev deuterons from the University of Pittsburgh cyclotron facility of the Sarah Mellon Scaife Radiation Laboratory.

The cross section (σ) for defect production in a metal due to irradiation can be taken as

$$\sigma = \sigma_d \bar{\nu} , \quad (1)$$

where σ_d is the cross section for creation of the primary knock-on atom, and $\bar{\nu}$ is the number of secondary displacements made per primary knock-on atom. The quantity σ_d , for the case of irradiation by several mev deuterons, is just the unscreened coulomb cross section for a transfer of energy to the knock-on atom between E_d and the maximum energy transfer (T_m) of a head-on collision¹. From energy and momentum conservation it follows that

$$T_m = \frac{4M_1 M_2}{(M_1 + M_2)^2} E , \quad (2)$$

where M_1 and M_2 are the masses of the incident and bombarded atoms respectively, and E is the energy of the incident particle. For coulomb

¹F. Seitz and J. S. Koehler, "Displacement of Atoms during Irradiation", in Solid State Physics (F. Seitz and D. Turnbull editors), Academic Press, New York, 1956, Vol. 2, pp. 316-319.

collisions, the differential cross section for energy transfer from T to $T + dE$ is²

$$d\sigma = \frac{c}{E} \frac{dE}{T^2} , \quad (3)$$

where

$$c = 4\pi a_0^2 \left(\frac{Z_1}{E_R} \right) Z_1^2 Z_2^2 E_R^2 . \quad (4)$$

Here a_0 is the Bohr radius, Z_1 and Z_2 are the atomic numbers of the incident and bombarded atoms respectively, and E_R is the Rydberg energy. We may now write that

$$\sigma_d = \frac{c}{E} \int_{E_d}^{T_M} \frac{dE}{T^2} = \frac{c}{E} \left(\frac{1}{E_d} - \frac{1}{T_M} \right) \quad (5)$$

The minimum energy for a displacement (E_d) has not been measured for tungsten; a value of 25 ev will be assumed here based on a rough average of measured values of E_d for several elements³. For 15 mev deuterons incident on tungsten, $T_M = .64$ mev, and the last term of equation 5 may be neglected. Therefore

$$\sigma_d = \left(\frac{c}{E_d} \right) \frac{1}{E} . \quad (6)$$

We see from equation (6) that for a given bombarding particle and bombarded element the cross section for creation of a primary knock-on should vary simply as $1/E$.

²Ibid., p. 314.

³G. J. Dienes and G. H. Vineyard, Radiation Effects in Solids, Interscience Publishers Inc., New York, 1957, Table 3.2, p. 61.

Except for some uncertainty in the parameter E_d , the expression of (6) can be used to compute σ_d with some confidence. The theoretical situation for the yield function $\bar{\nu}$, the number of displacements made for each knock-on atom, is not nearly so good. The average knock-on atom energy ($\bar{\mathcal{E}}$) is easily found from equations (3) and (6):

$$\bar{\mathcal{E}} = \frac{1}{\sigma_d} \int_{E_d}^{T_m} T d\sigma = \frac{E_d T_m}{T_m - E_d} \ln \frac{T_m}{E_d} \approx E_d \ln \frac{T_m}{E_d} . \quad (7)$$

Using the values we have for T_m and E_d , we get that $\bar{\mathcal{E}} \approx 250$ ev. At this energy atomic collisions are not unscreened coulomb repulsions as in the case of the high energy primary collisions⁴. The usual approximation used for these low energy collisions is some kind of hard sphere interaction potential. Several theories based on hard sphere models all give essentially the same result for $\bar{\nu}$, namely⁵:

$$\bar{\nu} = \frac{1}{2} \left(\frac{T_m}{T_m - E_d} \right) \left(1 + \ln \frac{T_m}{2E_d} \right) .$$

Neglecting E_d in the first factor we get that

$$\bar{\nu} = \frac{1}{2} \left(1 + \ln \frac{T_m}{2E_d} \right) . \quad (8)$$

Recent calculations indicate that the dependence of the yield function on incident particle energy is relatively insensitive to the interaction potential⁶. For the case of 15 mev deuterons incident on tungsten $\bar{\nu} = 5.0$

⁴Ibid, p. 11.

⁵Ibid, pp. 17-24.

⁶E. Brown and G. H. Goldecke, *J. Appl. Phys.* **31**, 932 (1960).

Combining equations (8) and (2) we get that

$$\bar{\nu} = \frac{1}{2}(1 + \ln \xi E) , \quad (9)$$

where

$$\xi = \frac{2M_1 M_2}{E_d (M_1 + M_2)^2} . \quad (10)$$

Combining equations (9), (6) and (1) we may now write the expression for the cross section for making a displacement:

$$\sigma = \frac{c}{2E_d} \left(\frac{1}{E} \right) \left(1 + \ln \xi E \right) . \quad (11)$$

The value of ξ for our problem is $.85 \times 10^3 \text{ mev}^{-1}$.

A test of the predicted energy dependence for defect production expressed in equation 11 was the first aim of this work, but a direct measurement of this cross section is not possible at this time. It is not possible because there is no physical property of the metal whose dependence on the volume density of defects is known quantitatively. However, we may measure the change in electrical resistivity with bombardment and expect the residual resistance of the metal to increase monotonically with defect density. Therefore, we can measure the change in electrical resistance with incident flux for small flux increments, a quantity proportional to σ , at various values of incident deuteron energy and test the energy dependence of equation 11.

Since the logarithmic term of equation 11 varies slowly with incident energy, the predicted slope of a radiation damage curve varies with incident energy almost as $1/E$.

Pearlstein and coworkers found an almost linear increase in the damage rate of tungsten with incident energy for protons in the energy range 100-400 mev⁷. This was in sharp contrast to the expected $1/E$ dependence. These observers suggested that the unexpected increase in damage rate in tungsten with incident energy was due to the importance at these higher energies of nuclear spallations. It was therefore the purpose of the first part of this work to look for the expected predominant $1/E$ dependence at lower incident energies where nuclear reactions are less important. For incident energies of 15 mev and lower, deviations from the $1/E$ dependence could also give information about the yield function.

F. Radiation Effects on the Mechanical Properties of Tungsten

In the first part we are interested in the mechanism of defect production in tungsten by 15 mev deuterons. In the second part we are interested in the effects of these radiation induced defects on the mechanical properties of tungsten.

It has been well established that mechanical properties of metals such as yield strength are determined not only by the lattice structure but also by the density of dislocations and other lattice defects. T. A. Read suggested in 1940 that in certain temperature and frequency ranges the internal friction in metals is due at least in part to the irreversible motion of dislocation lines⁸. Since then much

⁷E. A. Pearlstein, H. Ingham and R. Smoluchowski, Phys. Rev. 98, 530(A) (1955).

⁸T. A. Read, Phys. Rev. 58, 371 (1940).

experimental evidence has supported the hypothesis of dislocation damping in metals⁹. Other sources of internal friction in metals are well understood largely through the work of C. Zener¹⁰. For example, he studied grain boundary viscosity at about 600°K and .1 cps and thermo-elasticity at about 600°K and 10^4 cps. Dislocation damping in metals is complicated by the fact that the dislocations contribute to the internal friction by several mechanisms. The present understanding of the situation will be described briefly as follows.

1. Strain Independent Damping

Strain independent damping is associated with the bowing motion of the dislocation under a small applied stress. The dislocation is pictured as fixed on the ends by the surface of the sample or by jogs in the line, and pinned at places along its length by impurity atoms and point defects. (Cottrell has shown that these point imperfections tend to cluster around dislocations¹¹.) This damping is characterized experimentally by being strain amplitude independent, with the damping increasing slowly and monotonically with temperature from 4°K to room temperature¹².

2. Strain Dependent Damping

Strain dependent damping is associated with the bowing of the dislocation under an applied stress large enough to free the dislocation

⁹For a review of this work, see D. H. Niblett and J. Wilks, *Adv. in Phys.* 9, 1 (1960).

¹⁰C. Zener, Elasticity and Anelasticity of Metals, University of Chicago Press, Chicago, 1948.

¹¹A. H. Cottrell, Report of a Conference on the Strength of Solids, London: Phys. Soc., p. 30, 1948.

¹²H. L. Caswell, J. Appl. Phys. 29, 1210 (1958).

from its pinning sites. This damping is characterized experimentally by being highly strain amplitude dependent with a temperature dependence as in paragraph 1. The strain amplitude for the inception of this strain dependent damping shifts slowly and monotonically to lower values with increasing temperature¹².

3. The Bordoni Peak

P. G. Bordoni¹³ measured internal friction in several face centered cubic metals as a function of temperature from 4 to 300°K at constant frequency. He found distinct peaks in the internal friction dependence on temperature. Extensive work has been done on these Bordoni peaks; they have been observed in face centered cubic metals at frequencies from 10^3 to 10^6 cps and temperatures from 4 to 300°K. There is usually more than one peak and the main peak usually occurs around 100°K. These peaks have been studied as a function of the cold work state, the impurity content of the metal, and the applied frequency. Niblett and Wilks⁹ summarize the properties of Bordoni peaks as follows:

- (a) The Bordoni peak appears in both single crystal¹⁴ and polycrystalline samples.
- (b) The peak is generally not observed in fully annealed samples.
- (c) The height of the peak increases rapidly with increasing cold work.
- (d) The height of the peak and the peak temperature is almost independent of strain amplitude.

¹²op. cit. H. L. Caswell et al.

¹³P. G. Bordoni, J. Acous. Soc. Amer., 26, 495 (1954).

⁹op. cit., D. H. Niblett et al.

- (e) Impurities reduce the height of the peak.
- (f) The peak temperature increases with an increase in the applied frequency.
- (g) For a given applied frequency the peak temperature is unaffected by the state of cold work.

Niblett and Wilkes⁹ suggest that the Bordoni peak should also exist in body centered cubic metals. I. J. Bruner¹⁴ found no obvious Bordoni peak in cold worked iron of high purity, but Chambers and Schultz¹⁵ have recently reported Bordoni peaks in cold worked molybdenum and tungsten at frequencies of from 15 to 80 kc.

The general phenomenology of the effect of thermal friction in solids¹ postulates that when an applied stress is applied to a solid, the solid responds instantaneously with an elastic strain ϵ_1 , and the non-elastic strain ϵ_2 lags the applied stress. For sinusoidal applied stresses the non-elastic strain behaves viscously and lags the stress by 90°. Therefore one can write that

$$\epsilon = \epsilon_1 + i\epsilon_2 \quad (12)$$

or

$$\epsilon = \epsilon_1(1 + i \tan\phi)$$

where

$$\tan\phi = \epsilon_2/\epsilon_1$$

Since ϵ_2/ϵ_1 is always $< 10^{-2}$ for metals, one can take

$$\tan\phi = \phi$$

and

$$\epsilon = \epsilon_1(1 + i\phi) \quad (13)$$

⁹op. cit., D. H. Niblett et al.

¹⁴I. J. Bruner, Phys. Rev. Letters, 3, 411 (1959).

¹⁵R. H. Chambers and T. Schultz, Phys. Rev. Letters, 6, 273, (1961).

¹⁰op. cit., C. Zener.

where

$$\phi = \epsilon_2/\epsilon_1$$

The quantity ϕ for systems described by a second order linear differential equation of motion is just $1/Q$ where Q is defined in the usual way¹⁶.

The appropriate elastic modulus Y is then

$$Y \approx \sigma_1/\epsilon \approx \sigma_1/\epsilon_1(1 - i\phi). \quad (14)$$

Thus there is a non-elastic part of the "elastic" modulus associated with the internal friction. This is called the "modulus defect", and can be used along with internal friction to study non-elastic properties of solids.

The sample geometry used in these experiments was that of a cantilevered bar whose wave equation is a 4th order differential equation; the solution of this equation is given in Appendix A.

Values of internal friction will be given in this work in terms of the logarithmic decrement δ ¹⁷, which is related to Q by¹⁸

$$\delta = \pi/Q \quad (15)$$

The amplitude independent friction due to the bowing of dislocation lines arises from the work done in moving the dislocation through the Peierls potential. Figure 1a shows the situation for small

¹⁶A. A. Nowick, *Progress in Metal Physics*, 4, 1 (1953).

¹⁷The logarithmic decrement is defined for an underdamped system responding to a transient as $\delta = \ln(A_n/A_{n+1})$, where A_n is the maximum amplitude of the n^{th} cycle.

¹⁸See Appendix A.

applied stresses where the bowing of the dislocation is limited by the pinning points. When the applied stress gets large enough, the situation shown in Figure 1b and 1c obtains. This breaking away from pinning sites leads to the amplitude dependent friction. The bowing of a dislocation line in its slip plane is shown in Figure 2. Here the solid lines represent Peierls minima, and the dashed lines represent Peierls maxima. Consider a dislocation AB lying parallel to a Peierls well as in figure 2a. This dislocation is hard to move; it would take a stress of the order of the yield stress to bow it. In figure 2b the dislocation AB is made up of linear dislocations parallel to the Peierls wells and kinks perpendicular to the Peierls wells. The Peierls forces on the kinks largely cancel out and the kinks can be moved parallel to the wells quite easily¹⁹. Thus a shear stress in the plane of figure 2a will cause the dislocation to bow as shown.

The existence of the Bordoni peak has been explained by Seeger²⁰ in terms of the motion of dislocations as a result of thermal excitation. He suggests that the dislocations will form kinks due to the random thermal motion of their constituent atoms. Such a thermal bulge is depicted for a linear dislocation in figure 3. The kinks in this line are mutually attracted with a small force¹⁹, and the bulge will in general be unstable and collapse. If a stress is present it will either aid this collapse, or spread the kinks far enough apart to maintain the line in a bowed configuration if the length of the bulge is large enough. This is a dissipative process and concomitantly loss not

¹⁹A. H. Cottrell, Dislocations and Plastic Flow in Crystals, Clarendon Press, Oxford, 1953.

²⁰A. Seeger, Phil. Mag., 1, 651 (1956).

AFCRL-62-515

University of Pittsburgh
Department of Physics

DEFECT PRODUCTION, INTERNAL FRICTION, AND
YOUNG'S MODULUS IN DEUTERON IRRADIATED TUNGSTEN*

by

Daniel R. Muss

December, 1961

Scientific Report No. 1

Contract No. AF19(604)-3906
Project 5620 Task 562002

Prepared for: Electronic Research Directorate
Air Force Cambridge Research Laboratories
Office of Aerospace Research
United States Air Force
Bedford, Massachusetts

Submitted to the Graduate Faculty in the Division of the Natural
Sciences in partial fulfillment of the requirements for the degree of
Doctor of Philosophy.

Requests for additional copies by Agencies of the Department of Defense, their contractors, and other Government agencies should be directed to the:

ARMED SERVICES TECHNICAL INFORMATION AGENCY
ARLINGTON HALL STATION
ARLINGTON 12, VIRGINIA

Department of Defense contractors must be established for ASTIA services or have their 'need-to-know' certified by the cognizant military agency of their project or contract.

All other persons and organizations should apply to the:

U. S. DEPARTMENT OF COMMERCE
OFFICE OF TECHNICAL SERVICES
WASHINGTON 25, D. C.

TABLE OF CONTENTS

	Page
FOREWORD	11
I. INTRODUCTION	1
A. Defect Production	1
B. Radiation Effects on the Mechanical Properties of Tungsten	6
1. Strain Independent Damping	7
2. Strain Dependent Damping	7
3. The Bordoni Peak	8
II. EXPERIMENTAL PROCEDURE	16
A. The Cryostat	17
B. The Irradiation Facility	18
C. Determination of Beam Flux and Energy	20
1. Measurement of Beam Flux	20
2. Uncertainty in the Beam Flux Measurement	22
3. Incident Deuteron Energy Determination	23
4. Uncertainty in the Incident Deuteron Energy	25
D. Electrical Resistance	25
1. Measurement Technique	25
2. Uncertainties in the Measurement of Electrical Resistance	28
3. Sample Mounting Technique for Electrical Measurements	28

	Page
II. Mechanical Properties	30
1. Measurement of Internal Friction and Elastic Modulus	30
2. Uncertainty in the Measurement of Internal Friction and Elastic Modulus	35
3. Temperature Measurement	38
4. Sample Mounting Technique for Mechanical Measurements	39
a. The Sample Holder	39
b. The Sample Mounting Operation	39
c. The Drive Plate	41
d. Assembly Procedure	41
III. THE ENERGY DEPENDENCE OF RADIATION DAMAGE IN TUNGSTEN	44
A. Results	44
B. Discussion of the Energy Dependence Results	48
IV. EFFECTS OF RADIATION ON THE MECHANICAL PROPERTIES OF TUNGSTEN	53
A. Results	53
1. The Pre-Irradiation Bordoni Peak	53
2. The Effect of Irradiation at 300°K on Internal Friction and Young's Modulus	54
3. Irradiation at 79°K and the Effect of Annealing on Internal Friction	55
4. The Temperature Dependence of the Resonant Frequency	56

	Page
B. Discussion	57
1. The Pre-Irradiation Bordoni Peak	58
2. The Effect of Room Temperature Irradiation on the Bordoni Peak	59
3. The Effect of Room Temperature on the Background (Strain Independent) Internal Friction	63
4. The Effect of Irradiation at 79°K on Internal Friction	65
APPENDIX A. VIBRATION OF A CANTILEVERED ROD	118
APPENDIX B. THE RELAXATION PROCESS	124
APPENDIX C. LOW TEMPERATURE VACUUM TIGHT SEALS FOR ALUMINUM FOIL TO COPPER	126
APPENDIX D. EFFECT OF AN RLC FILTER ON THE TRANSIENT SIGNAL	128
APPENDIX E. CORRECTION FOR THE ENERGY LOSS IN THE SAMPLE	131
BIBLIOGRAPHY	135

I. INTRODUCTION

The study of radiation effects in solids is a relatively new one, dating from the growth of nuclear reactor technology during and just after the second World War. Although nuclear physicists have studied the passage of high energy radiation through solids, it was always from the point of view of the bombarding ray, the target being of interest only for its stopping power. The interest in the bombarded solid was at first concerned with reactor technology. A high energy charged particle passing through a solid loses almost all its kinetic energy by ionization, i.e. collisions with orbital electrons of the host atom. Neutrons are stopped in a solid by making nuclear interactions. The charged high energy products of this interaction then lose their energy primarily by ionization. The occasional elastic coulomb collisions of the nuclear reaction products with lattice atoms, negligible as far as computing the stopping power of the solid was concerned, became important in the high neutron fluxes of reactors. Displacement of lattice atoms by radiation caused gross physical changes in reactor materials. Soon the problem of radiation damage became of interest for itself as a means of studying the solid state.

A. Defect Production

When a lattice atom, in collision with incident radiation, receives energy greater than some minimum energy (E_d) needed to remove it from its lattice site, it moves through the lattice with its residual kinetic energy. This knock-on atom will come to rest in general at an interstitial site; it becomes an interstitial defect, and leaves behind

a vacancy defect. The knock-on atom may lose its kinetic energy by creating further displacements of lattice atoms or by making collisions involving energy transfers of less than E_d . The energies of these latter collisions are carried off as phonons. It was the purpose of this work in part to study the process of defect production by bombarding tungsten with 15 mev deuterons from the University of Pittsburgh cyclotron facility of the Sarah Mellon Scaife Radiation Laboratory.

The cross section (σ) for defect production in a metal due to irradiation can be taken as

$$\sigma = \sigma_d \bar{\nu} \quad , \quad (1)$$

where σ_d is the cross section for creation of the primary knock-on atom, and $\bar{\nu}$ is the number of secondary displacements made per primary knock-on atom. The quantity σ_d , for the case of irradiation by several mev deuterons, is just the unscreened coulomb cross section for a transfer of energy to the knock-on atom between E_d and the maximum energy transfer (T_m) of a head-on collision¹. From energy and momentum conservation it follows that

$$T_m = \frac{4M_1 M_2}{(M_1 + M_2)^2} E \quad , \quad (2)$$

where M_1 and M_2 are the masses of the incident and bombarded atoms respectively, and E is the energy of the incident particle. For coulomb

¹F. Seitz and J. S. Koehler, "Displacement of Atoms during Irradiation", in Solid State Physics (F. Seitz and D. Turnbull editors), Academic Press, New York, 1956, Vol. 2, pp. 316-319.

collisions, the differential cross section for energy transfer from T to $T + dT$ is²

$$d\sigma = \frac{c}{E} \frac{dT}{T^2} , \quad (3)$$

where

$$c = 4\pi r_0^2 \left(\frac{Z_1}{E_R} \right) Z_1^2 Z_2^2 Z_R^2 . \quad (4)$$

Here r_0 is the Bohr radius, Z_1 and Z_2 are the atomic numbers of the incident and bombarded atoms respectively, and E_R is the Rydberg energy.

We may now write that

$$\sigma_t = \frac{c}{E} \int_{E_d}^{T_R} \frac{dT}{T^2} = \frac{c}{E} \left(\frac{1}{E_d} - \frac{1}{E_R} \right) \quad (5)$$

The minimum energy for a displacement (E_d) has not been measured for tungsten; a value of 25 ev will be assumed here based on a rough average of measured values of E_d for several elements³. For 15 mev deuterons incident on tungsten, $T_R = .64$ mev, and the last term of equation 5 may be neglected. Therefore

$$\sigma_t = \left(\frac{c}{E_d} \right) \frac{1}{E} . \quad (6)$$

We see from equation (6) that for a given bombarding particle and bombarded element the cross section for creation of a primary knock-on should vary simply as $1/E$.

²Ibid, p. 314.

³G. J. Dienes and G. H. Vineyard, Radiation Effects in Solids, Interscience Publishers Inc., New York, 1957, Table 3.2, p. 61.

Except for some uncertainty in the parameter E_d , the expression of (6) can be used to compute σ_d with some confidence. The theoretical situation for the yield function $\bar{\nu}$, the number of displacements made for each knock-on atom, is not nearly so good. The average knock-on atom energy (\bar{T}) is easily found from equations (3) and (6):

$$\bar{T} = \frac{1}{\sigma_d} \int_{E_d}^{T_m} T d\sigma = \frac{E_d T_m}{T_m - E_d} \ln \frac{T_m}{E_d} \approx E_d \ln \frac{T_m}{E_d} . \quad (7)$$

Using the values we have for T_m and E_d , we get that $\bar{T} \approx 250$ ev. At this energy atomic collisions are not unscreened coulomb repulsions as in the case of the high energy primary collisions⁴. The usual approximation used for these low energy collisions is some kind of hard sphere interaction potential. Several theories based on hard sphere models all give essentially the same result for $\bar{\nu}$, namely⁵:

$$\bar{\nu} = \frac{1}{2} \left(\frac{T_m}{T_m - E_d} \right) \left(1 + \ln \frac{T_m}{2E_d} \right) .$$

Neglecting E_d in the first factor we get that

$$\bar{\nu} = \frac{1}{2} \left(1 + \ln \frac{T_m}{2E_d} \right) . \quad (8)$$

Recent calculations indicate that the dependence of the yield function on incident particle energy is relatively insensitive to the interaction potential⁶. For the case of 15 mev deuterons incident on tungsten $\bar{\nu} = 5.0$

⁴Ibid, p. 11.

⁵Ibid, pp. 17-24.

⁶E. Brown and G. H. Goldeck, *J. Appl. Phys.*, 31, 932 (1960).

Combining equations (8) and (2) we get that

$$\bar{\nu} = \frac{1}{2}(1 + \ln \xi E) , \quad (9)$$

where

$$\xi = \frac{2M_1 M_2}{E_d (M_1 + M_2)^2} . \quad (10)$$

Combining equations (9), (6) and (1) we may now write the expression for the cross section for making a displacement:

$$\sigma = \frac{c}{2E_d} \left(\frac{1}{E} \right) \left(1 + \ln \xi E \right) . \quad (11)$$

The value of ξ for our problem is $.85 \times 10^3 \text{ mev}^{-1}$.

A test of the predicted energy dependence for defect production expressed in equation 11 was the first aim of this work, but a direct measurement of this cross section is not possible at this time. It is not possible because there is no physical property of the metal whose dependence on the volume density of defects is known quantitatively. However, we may measure the change in electrical resistivity with bombardment and expect the residual resistance of the metal to increase monotonically with defect density. Therefore, we can measure the change in electrical resistance with incident flux for small flux increments, a quantity proportional to σ , at various values of incident deuteron energy and test the energy dependence of equation 11.

Since the logarithmic term of equation 11 varies slowly with incident energy, the predicted slope of a radiation damage curve varies with incident energy almost as $1/E$.

Pearlstein and coworkers found an almost linear increase in the damage rate of tungsten with incident energy for protons in the energy range 100-400 mev⁷. This was in sharp contrast to the expected $1/E$ dependence. These observers suggested that the unexpected increase in damage rate in tungsten with incident energy was due to the importance at these higher energies of nuclear spallations. It was therefore the purpose of the first part of this work to look for the expected predominant $1/E$ dependence at lower incident energies where nuclear reactions are less important. For incident energies of 15 mev and lower, deviations from the $1/E$ dependence could also give information about the yield function.

E. Radiation Effects on the Mechanical Properties of Tungsten

In the first part we are interested in the mechanism of defect production in tungsten by 15 mev deuterons. In the second part we are interested in the effects of these radiation induced defects on the mechanical properties of tungsten.

It has been well established that mechanical properties of metals such as yield strength are determined not only by the lattice structure but also by the density of dislocations and other lattice defects. T. A. Read suggested in 1940 that in certain temperature and frequency ranges the internal friction in metals is due at least in part to the irreversible motion of dislocation lines⁸. Since then much

⁷E. A. Pearlstein, R. Ingham and R. Smoluchowski, Phys. Rev. 98, 1530(A) (1955).

⁸T. A. Read, Phys. Rev. 58, 371 (1940).

experimental evidence has supported the hypothesis of dislocation damping in metals⁹. Other sources of internal friction in metals are well understood largely through the work of C. Zener¹⁰. For example, he studied grain boundary viscosity at about 600°K and .1 cps and thermoelasticity at about 600°K and 10^4 cps. Dislocation damping in metals is complicated by the fact that the dislocations contribute to the internal friction by several mechanisms. The present understanding of the situation will be described briefly as follows.

1. Strain Independent Damping

Strain independent damping is associated with the bowing motion of the dislocation under a small applied stress. The dislocation is pictured as fixed on the ends by the surface of the sample or by jogs in the line, and pinned at places along its length by impurity atoms and point defects. (Cottrell has shown that these point imperfections tend to cluster around dislocations¹¹.) This damping is characterized experimentally by being strain amplitude independent, with the damping increasing slowly and monotonically with temperature from 4°K to room temperature¹².

2. Strain Dependent Damping

Strain dependent damping is associated with the bowing of the dislocation under an applied stress large enough to free the dislocation

⁹For a review of this work, see D. H. Niblett and J. Wilks, *Adv. in Phys.* 9, 1 (1960).

¹⁰C. Zener, Elasticity and Anelasticity of Metals, University of Chicago Press, Chicago, 1948.

¹¹A. H. Cottrell, Report of a Conference on the Strength of Solids, London: Phys. Soc., p. 30, 1948.

¹²H. L. Caswell, *J. Appl. Phys.* 29, 1210 (1958).

from its pinning sites. This damping is characterized experimentally by being highly strain amplitude dependent with a temperature dependence as in paragraph 1. The strain amplitude for the inception of this strain dependent damping shifts slowly and monotonically to lower values with increasing temperature¹².

3. The Bordoni Peak

P. G. Bordoni¹³ measured internal friction in several face centered cubic metals as a function of temperature from 4 to 300°K at constant frequency. He found distinct peaks in the internal friction dependence on temperature. Extensive work has been done on these Bordoni peaks; they have been observed in face centered cubic metals at frequencies from 10^3 to 10^6 cps and temperatures from 4 to 300°K. There is usually more than one peak and the main peak usually occurs around 100°K. These peaks have been studied as a function of the cold work state, the impurity content of the metal, and the applied frequency. Niblett and Wilks⁹ summarize the properties of Bordoni peaks as follows:

- (a) The Bordoni peak appears in both single crystal and polycrystalline samples.
- (b) The peak is generally not observed in fully annealed samples.
- (c) The height of the peak increases rapidly with increasing cold work.
- (d) The height of the peak and the peak temperature is almost independent of strain amplitude.

¹²op. cit., H. L. Caswell *et al.*

¹³P. G. Bordoni, *J. Acous. Soc. Amer.*, 26, 495 (1954).

⁹op. cit., D. H. Niblett *et al.*

- (e) Impurities reduce the height of the peak.
- (f) The peak temperature increases with an increase in the applied frequency.
- (g) For a given applied frequency the peak temperature is unaffected by the state of cold work.

Niblett and Wilks⁹ suggest that the Bordoni peak should also exist in body centered cubic metals. L. J. Bruner¹⁴ found no obvious Bordoni peak in cold worked iron of high purity, but Chambers and Schultz¹⁵ have recently reported Bordoni peaks in cold worked molybdenum and tungsten at frequencies of from 15 to 80 kc.

The general phenomenological theories of internal friction in solids¹⁶ postulate that when a stress is applied to a solid, the solid responds instantaneously with an elastic strain ϵ_1 , and the non-elastic strain ϵ_2 lags the applied stress. For sinusoidal applied stresses the non-elastic strain behaves viscously and lags the stress by 90°.

Therefore one can write that

$$\epsilon = \epsilon_1 + i\epsilon_2 \quad , \quad (12)$$

or $\epsilon = \epsilon_1(1 + i \tan\phi) \quad ,$

where $\tan\phi = \epsilon_2/\epsilon_1 \quad .$

Since ϵ_2/ϵ_1 is always $< 10^{-2}$ for metals, one can take

$$\tan\phi = \phi \quad ,$$

and $\epsilon = \epsilon_1(1 + i\phi) \quad , \quad (13)$

⁹op. cit., D. H. Niblett et al.

¹⁴L. J. Bruner, Phys. Rev. Letters, 3, 411 (1959).

¹⁵R. H. Chambers and J. Schultz, Phys. Rev. Letters, 6, 273, (1961).

¹⁰op. cit., C. Zener.

where

$$\phi = \epsilon_2/\epsilon_1$$

The quantity ϕ for systems described by a second order linear differential equation of motion is just $1/Q$ where Q is defined in the usual way¹⁶.

The appropriate elastic modulus Y is then

$$Y \approx \sigma_1/\epsilon \approx \sigma_1/\epsilon_1(1 - i\phi). \quad (14)$$

Thus there is a non-elastic part of the "elastic" modulus associated with the internal friction. This is called the "modulus defect", and can be used along with internal friction to study non-elastic properties of solids.

The sample geometry used in these experiments was that of a cantilevered bar whose wave equation is a 4th order differential equation; the solution of this equation is given in Appendix A.

Values of internal friction will be given in this work in terms of the logarithmic decrement δ ¹⁷, which is related to Q by¹⁸

$$\delta = \pi/Q \quad (15)$$

The amplitude independent friction due to the bowing of dislocation lines arises from the work done in moving the dislocation through the Peierls potential. Figure 1a shows the situation for small

¹⁶A. A. Nowick, *Progress in Metal Physics*, 4, 1 (1953).

¹⁷The logarithmic decrement is defined for an underdamped system responding to a transient as $\delta \approx \ln(A_n/A_{n+1})$, where A_n is the maximum amplitude of the n^{th} cycle.

¹⁸See Appendix A.

applied stresses where the bowing of the dislocation is limited by the pinning points. When the applied stress gets large enough, the situation shown in Figure 1b and 1c obtains. This breaking away from pinning sites leads to the amplitude dependent friction. The bowing of a dislocation line in its slip plane is shown in Figure 2. Here the solid lines represent Peierls minima, and the dashed lines represent Peierls maxima. Consider a dislocation AB lying parallel to a Peierls well as in figure 2a. This dislocation is hard to move; it would take a stress of the order of the yield stress to bow it. In figure 2a the dislocation AB is made up of linear dislocations parallel to the Peierls wells and kinks perpendicular to the Peierls wells. The Peierls forces on the kinks largely cancel out and the kinks can be moved parallel to the wells quite easily¹⁹. Thus a shear stress in the plane of figure 2a will cause the dislocation to bow as shown.

The existence of the Bordoni peak has been explained by Seeger²⁰ in terms of the motion of dislocations as a result of thermal excitation. He suggests that the dislocations will form bulges due to the random thermal motion of their constituent atoms. Such a thermal bulge is depicted for a linear dislocation in figure 3. The kinks in this line are mutually attracted with a small force¹⁹, and the bulge will in general be unstable and collapse. If a stress is present it will either aid this collapse, or spread the kinks far enough apart to maintain the line in a bowed configuration, if the length of the bulge is large enough. This is a dissipative process and contributes a loss not

¹⁹A. H. Cottrell, Dislocations and Plastic Flow in Crystals, Clarendon Press, Oxford, 1953.

²⁰A. Seeger, Phil. Mag., 1, 651 (1956).

present without the thermal excitation. The same kind of process will produce additional damping for the dislocation of figure 2b.

Let us consider the contribution to the dislocation damping due only to this thermal bulging. At very low temperatures the thermal bulging rate is low and the bulging will contribute very slowly to the motion of a dislocation under an applied stress of a given frequency. Eventually the time constant of ϵ_2 in figure 4 will be much longer than the period of the applied stress and the strain will respond as in curve (c). This situation is described in the stress-strain plot of figure 5 by going from 0 to A and then back to 0 and the behaviour is elastic. At very high temperatures the bulging rate is high and the motion of the dislocation due to thermal bulging will respond immediately to the applied stress and the strain would behave as shown ideally in curve (a) of figure 4. In the stress-strain diagram this would be described by going elastically from 0 to C and then back to 0. The intermediate case of the time constant of ϵ_2 being of the order of the period of the applied stress is shown in curve (b). Here the solid goes from 0 to A in figure 5 instantaneously, then slowly approaches C. When the applied stress is removed it moves instantaneously from some point B to D and then slowly approaches 0. In this last case there is damping.

Seeger²⁰ assumes a simple relaxation process to describe the Bordoni peak:

$$\delta = 2\delta_{\max} \frac{f/f_0}{(1 + (f/f_0)^2)} . \quad (16)$$

This relationship is derived in Appendix B. The peak height is related to be

$$\delta_{\max} \approx N_0 L^3 / 8 , \quad (17)$$

²⁰ Op. cit., A. Seeger.

where N_0 is the volume density of dislocations, and L_0 is the average dislocation length. The bulge rate is taken to have an Arrhenius dependence with a single activation energy, namely:

$$f_0 = A \exp(-H/kT) . \quad (18)$$

This assumption is supported by calculations of Donth²¹, who considered the statistics of thermal bulging in dislocation lines. Here A is the attempt frequency, k is Boltzmann's constant, T is the absolute temperature, and H is the activation energy for the bulging process.

This relaxation theory is moderately successful in describing the experimental Bordoni peaks. It predicts the peak shift with frequency and it agrees roughly with the cold work effects. By measurement of the peak temperature shift with applied frequency, several workers have determined H and A for copper²². When these values of H and A were applied to the Bordoni peak shape, they give a theoretical peak width in temperature about half that observed. Although these measurements of H and A are not accurate, they suggest that the assumption of a single relaxation process is an oversimplification.

Studies of irradiation effects on internal friction in metals have not been extensive. Thompson and Holmes²³, Niblett and Wilks²⁴, and Barnes and Hancock²⁵ have studied the effects of neutron irradiation

²¹H. Donth, Z. Phys., 131, 156 (1957).

²²Composite values of H and A based on the work of several investigators are given in reference 9, p. 27.

²³D. O. Thompson and D. H. Holmes, J. Appl. Phys., 27, 713 (1956), 30, 525 (1959).

²⁴D. H. Niblett and J. Wilks, Phil. Mag., 2, 1427 (1957).

²⁵R. S. Barnes and N. H. Hancock, Phil. Mag. 3, 527 (1958).

on the strain amplitude independent friction and the Bordoni peaks in copper. They find that the strain independent friction is reduced by about a factor of 7 with relatively light irradiations (10^{12} nvt.), but the heights of the Bordoni peaks are reduced greatly by a heavy irradiation (10^{17-18} nvt.). This work is of great importance, but to date copper has been the only metal studied. The only studies of the effect of charged particle irradiation (1 mev electrons) on internal friction in copper were made by Dieckamp and Sosin²⁶. Their measurements show the same drastic reduction in the strain independent damping with irradiation observed by Thompson and Holmes.

We started out to extend this work, studying the effect of 15 mev deuteron bombardment on the strain independent damping. Our intention was to look first at tungsten, (the metal we studied in the first part of this investigation) and then proceed to other metals. The first results however showed an unmistakable Bordoni peak in tungsten. Since no Bordoni peak had been reported at this time in a body centered cubic metal, it seemed that tungsten deserved detailed attention. Therefore observations were made on the effects of deuteron irradiation on both the Bordoni peak and the strain independent background friction in tungsten, covering a temperature range from 77°K to 300°K. The mechanical properties observed were the internal friction and the elastic modulus of tungsten, and irradiations were made both at 77°K and 300°K.

Irradiation also has an effect on the elastic modulus apart from its non-elastic behaviour. Let us, for example, irradiate a metal at a temperature such that the interstitials produced are mobile

²⁶H. Dieckamp and A. Sosin, J. Appl. Phys., 27, 1416 (1956).

(and presumably migrate to dislocations and other sinks) and the vacancies are not mobile. Now the lattice will be sprinkled with vacancies, and a change in the average lattice spacing is expected. This is usually called the bulk effect, and Dienes²⁷ has calculated the expected change in the elastic constants of a metal for a given number of point defects. This experiment is reported here for tungsten, and the results compared with Dienes' predictions.

It has been found that non-elastic effects occur in substitutional alloys when the components are of different sizes^{28,29}. This effect has been attributed to the stress induced reorientation of pairs of solute atoms. Nowick³⁰ used this effect to support the idea that diffusion in metals takes place through the thermal motion of vacancies. Dienes³¹ suggested on the basis of this work that radiation induced defects could be studied using intercal fraction measurements. He also suggested that the annealing of these defects could be observed in the same way. Results of such an experiment are reported here.

²⁷ G. J. Dienes, Phys. Rev., 86, 228 (1951).

²⁸ J. Zener, A.I.M.E., 52, 122 (1943).

²⁹ A. S. Nowick, Phys. Rev., 82, 390(A) (1951).

³⁰ Ibid., p. 551.

³¹ G. J. Dienes, J. Appl. Phys., 24, 666 (1953).

II. EXPERIMENTAL PROCEDURE

All the irradiations described here were made in the external beam ductwork of the cyclotron, in the room housing the cyclotron. Measurements of the metal properties under investigation were made either in situ in the cyclotron room or on the laboratory bench, whichever was appropriate.

The external beam of the cyclotron spreads out rapidly in the horizontal plane due to the fringing field of the cyclotron magnet. This divergent beam is then magnetically focussed and sent through a water wall into another room where the apparatus for doing nuclear scattering experiments is located. To reduce the neutron background for scattering experiments the beam aperture is reduced to about one inch at a place where the beam is about 12 inches wide. This is accomplished by a pair of roughing slits located about 5 feet in front of the first focussing magnet. The radiation effects installation was placed between the roughing slits and the first focussing magnet, utilizing a portion of the beam previously blocked by one of the roughing slits. It was originally thought that this arrangement would allow both experiments to run at the same time making efficient use of cyclotron time. Although some data was taken this way, this arrangement turned out to be inconvenient. Cyclotron time used for data taking was small compared with the time needed to design and install new equipment plus the even greater time needed to get this new equipment working properly. The people involved in this work are exposed to much greater personal radiation than they would be if this experiment were carried out in the nuclear scattering room.

A. The Cryostat

The experiments reported here were done in a cryostat capable of maintaining temperatures between 77 and 300°K. The cryostat is connected by rubber vacuum hose to a pumping system capable of attaining pressures of from 10^{-4} to 10^{-3} mm. of Hg. The pumping system is mobile so the cryostat with its pump can be moved from the laboratory bench into the cyclotron room. Photographs of the cryostat as assembled are shown in figures 6 and 7. The cryostat is made of two parts and the region between them is evacuated. The inside part is shown in the photographs of figures 8 and 9. The well holding the coolant is made of a thin walled stainless steel cylinder closed at the bottom with a copper plug. The sample to be studied and associated parts are placed on a copper block which is soldered to the bottom of the coolant well with Wood's metal. The sample region is then sealed by a copper can soldered in place with Wood's metal. Two pipes go from the sample chamber through the cold well to the top flange of the cold well. Electrical connections are brought out through one of these pipes, and plumbing arrangements are made to either pump out the sample chamber or flow gas through the chamber at one atmosphere. The electrical leads come out through a straight, thin walled, stainless steel pipe. This pipe leads to a chamber mounted on the top flange of the cryostat. This chamber provides Stupakoff seals to bring the electrical leads out of the vacuum system. A vacuum gauge can be fitted to the lead-out chamber if it is needed. The other pipe is of copper which makes several turns at the bottom of the well then joins a straight, thin walled, stainless steel section to come out of the well.

The copper sample can has beam entrance and exit holes which are covered with .001 inch thick aluminum foils. The technique for making

vacuum tight seals for these foils is described in Appendix C. The outside section of the cryostat also has entrance and exit holes for the beam. The entrance hole is sealed by a .00025 inch nickel foil soldered in place with Wood's metal. The exit hole in the outside section leads into the Faraday cup chamber. Since the beam is dispersed by scattering in the foils as it leaves the cyclotron vacuum system, collimation is needed to insure that the beam flux incident on the sample is collected by the Faraday cup. This is accomplished by a set of water cooled slits on the front face of the cryostat and by a collimator located in the sample chamber immediately in front of the sample. The position of the front slits is set, and the alignment of the system is checked optically before the foils are mounted. A simplified cut-away sketch of the cryostat is shown in figure 10.

B. The Irradiation Facility

Figures 11 and 12 show side and top views respectively of the beam port and the mechanisms providing motion of the cryostat up-down, and in-out. Holes were cut in the existing ductwork (b) on top and bottom and additional working volume was provided by top flange (c) and bottom can (a). A hollow beam can in the shape of a rectangular parallelopiped (1) was fitted to the top plate (d) completing the vacuum system. All joints were sealed by "O" rings not shown in the drawings of figures 11 and 12. The beam can (1) has a horizontal beam port located near the central horizontal plane of the duct. Figure 13 shows a detail of this beam port. The face of the beam can is counter-bored to receive a plate containing the beam aperture. The location and area of the aperture can be changed by changing this plate. Both the can face and the aperture plate are pre-tinned with soft solder and a

.001 inch thick nickel foil is soft soldered in place. The nickel foil permits the deuterons to leave the vacuum system and enter the beam box. The beam port is cooled by 1/8 inch O.D. copper water lines shown in figure 13. The water lines come up along the side of the beam box (1), and out between the top flange of the beam box and the bottom of the base plate (e).

The base plate (e) moves on tracks mounted on the top plate (d). Motion is provided by a screw fixed to the shaft of motor (j) and a nut fixed to the base plate (e) as shown in figure 12. A pair of micro-switches mounted on the top plate (d) allow a traverse of about 1.5 inches. Three screws are fixed to the cryostat ring (h) at 120° intervals as shown in figure 12. These screws run in three geared nuts (g), and the geared nuts are fixed to the base by thrust bearings. The geared nuts are rotated together by motor (f) through a chain drive providing motion of the cryostat ring up and down. A pair of microswitches allow about one inch of up-down motion.

The top flange of the cryostat is fixed to the cryostat ring and the lower part of the cryostat sits down inside the beam box. There is a set of angle markings on the cryostat ring and a fiducial mark on the cryostat flange showing the proper beam direction through the cryostat. The cryostat is rotated 2° from the direction of the duct center line. This angular correction was determined by having the beam throw a shadow near the cryostat position. Since the beam flux density is highest at the center of the duct, outward motion provided a decrease in the flux density when needed by a factor of about 2. The beam height at our position is about 1/4 inch and the cryostat aperture was about 1/8 inch. The sample is positioned in the beam by raising and lowering the cryostat until the beam current in the cryostat Faraday cup is a maximum. Since

20

the Faraday cup aperture was appreciably smaller than the beam height, this maximum was quite broad. The circuits used for remote control of the cryostat position are shown in figure 14.

C. Determination of Beam Flux and Energy

1. Measurement of Beam Flux

The beam of deuterons incident on the sample in the cryostat is collected in a Faraday cup. The incident deuteron flux is then just the total number of deuterons collected in the Faraday cup divided by the area of the collimator opening located immediately in front of the sample. The Faraday cup chamber is shown in the scale section drawing of figure 15. The chamber is fixed to the back face of the cryostat with an "O" ring completing the cryostat vacuum system. Stupakoff seals provide both physical support and electrical contact to the Faraday cup and to a suppressor grid located inside the Faraday cup. The suppressor grid is maintained at about 1500 volts negative with respect to earth ground. This prevents the loss of secondary electrons produced by deuteron bombardment of the Faraday cup.

The suppressor power supply circuit is shown in figure 16; the one megohm series resistor is provided for safety reasons. The circuit used for beam current measurement in the first part of this work, (i.e. measurement of changes in electrical resistance with bombardment), is shown in figure 17. The Faraday cup is connected to ground through a known high resistance and the voltage drop across this resistor is used to drive two Varian strip chart recorders. The Varian recorder is a Δ -if-balancing potentiometer which plots the input signal as a function of time. The area under the curve plotted by the recorder is then proportional to the total charge entering the Faraday cup. The full

scale span of the recorder is .010 volts and it can be operated with one second full scale response time with a maximum allowable input resistance of .25 megohms. Therefore the most sensitive full scale beam current setting with this system was .040 microamperes. The first recorder is located in the cyclotron control room and it is used to monitor the beam current in the cryostat for cyclotron tuning purposes. The second recorder, located at the laboratory bench, does the plotting. The controls for remote positioning of the cryostat in the beam are also located at the laboratory bench, and the second recorder serves as a beam current monitor for positional tuning.

For the studies of changes in mechanical properties with bombardment, greater beam current measurement sensitivity was desired. This was accomplished with the measurement system shown in Figure 18. As before, the Faraday cup is connected to ground through a calibrated high resistance. The voltage drop across this resistor is measured by a Keithly d.c. electrometer. The Keithly indicates a voltage proportional to the beam current and also provides this signal at a gain of one with 400 ohms internal resistance. The Keithly is placed in the cyclotron control room and its output signal used to drive the second Varian recorder. The Keithly is used on its .020 volts scale and full scale beam current settings of .001 microamperes and higher are available. The strip chart recordings of the beam current were integrated using a polar planimeter. Then, knowing the full scale setting of beam current circuit and the speed of the chart motor, these areas were converted into the total number of deuterons entering the Faraday cup.

At the radiation effects installation the beam intensity is about 1 microampere/cm² or 6×10^{12} deuterons/sec/cm². The area of the

collimator opening was in general about $.1 \text{ cm}^2$ so that most data was taken with about $0.1\mu \text{ amp.}$ in the Faraday cup. When less beam was desired the cyclotron could be operated down to about $1/10$ its maximum beam, (the lower limit for stable operation), and the cryostat could be pulled out from the duct center to give a further reduction by a factor of 2 in the Faraday cup current.

The suppressor grid power supply and the beam current circuit have output and input resistances respectively of the order of one megohm. Therefore neither circuit could tolerate appreciable electrical leakage conductance to ground across the glass insulation of the Stupakoff seals. Such leakage was experienced when the beam was present in the humid atmosphere of the beam well. To prevent this leakage both suppressor and Faraday cup leads were brought up to the top flange of the cryostat and out of the well in sealed copper tubes ending in standard coaxial connectors.

2. The Uncertainty in the Beam Flux Measurement

The possible sources of random error in the first beam flux measurement system are (a) random calibration error in the recorder, (b) recorder zero shift during irradiation, (c) recorder dead space, and (d) planimeter area measurement error. The error introduced by (a) was eliminated by checking the recorder deflection for a calibrated input current between each irradiation exposure. The error introduced by (d) was found statistically to be about $.2\%$. The maximum error due to (c) is 1% of full scale deflection or an average of about 2% . The error due to (b) is estimated to be about 1% . (The error due to (b) is easily confused with that of (c).) The total probable random error in the beam flux measurement of the first part of this work is estimated to be about 2% .

The possible sources of systematic error in the resistivity measurements experiment are systematic calibration error in the recorder (eliminated as in (a) of the previous paragraph), and beam area change due to loss of collimation. The collimation is known to have remained unchanged in the following way. The beam, passing through the aluminum foil on the exit window of the sample can, leaves a light shadow on the foil. This shadow was always quite sharp and the area of the shadow was equal to the area of the collimator. Thus, the systematic error in the first part was essentially zero.

In measuring mechanical properties, sources of error in beam flux measurements are essentially the same as those encountered in the first part. The difference was that in the second system (b) became very much larger. When the cyclotron oscillator was turned on there was a change in the zero setting of the Keithly electrometer of about 1% of full scale. This change varied from day to day and from hour to hour. To minimize the error due to this shifting zero a beam gate on the cyclotron was closed and then reopened regularly during a radiation exposure to establish the zero setting on the recorder chart. The estimated probable error in beam flux measurement in the second system used is 6%. As before no systematic error is expected.

3. Incident Deuteron Energy Determination

The energy of the deuterons incident on the sample was determined in the following way. The energy of the external beam is known, and the energy losses caused by the beam passing through several foils was computed from standard Range-Energy curves³². Three cases were of

³²W. A. Aron, B. G. Hoffman, and F. C. Williams, Rept. ARCL-663, UCRL-121 (1949).

interest in studying the energy dependence of radiation damage. The first was the maximum energy attainable with our system. This maximum energy (E_0) resulted from the beam passing in sequence through a .0010 inch thick nickel foil upon entering the beam well, then through a .00025 inch thick nickel foil upon entering the cryostat, and then through a .00075 thick aluminum foil upon entering the sample chamber. In addition there is a small energy loss due to the passage of the beam through a gas atmosphere. The initial beam energy was taken to be 14.9 mev. The value of E_0 was computed to be 13.7 mev. The second case involved placing a .005 inch thick aluminum plate in the incident beam path. For this situation the beam passes in sequence through the .0010 inch nickel, the .0050 inch aluminum, the .00025 inch nickel, the .00075 inch aluminum and again the small correction for the atmosphere. The incident deuteron energy with the .0050 inch aluminum plate in place was found to be: $E_1 = 12.1$ mev. The incident deuteron energy with a .0100 inch aluminum plate in place was found to be: $E_2 = 10.3$ mev.

Changes in incident energy were accomplished in situ using a plate changer located just in front of the front slits on the cryostat. The plate changer was a frame that ran up and down in tracks fixed to the front slits. The frame had three positions, the first was open, the second and third placed the .0050 and the .0100 inch aluminum plates respectively in front of the entrance window of the cryostat. The frame was held in the first position by a spring attached to the bottom of the cryostat. The top of the frame was connected to a keyed position block on the top of the cryostat by a pair of nylon lines. Moving the position block from the first position to the second or third pulled the plate frame against the spring tension placing the .0050 or the .0100 inch plate in front of the entrance window.

4. Uncertainty in the Incident Deuteron Energy

The quantities that are of interest in the energy dependence work are the ratios E_1/E_0 and E_2/E_0 . The errors involved in computing the stopping powers of the foils present for all three energies E_0 , E_1 and E_2 are systematic; their contribution to the uncertainty in the ratios E_1/E_0 and E_2/E_0 tend to cancel out. The systematic uncertainty in the ratios E_1/E_0 and E_2/E_0 due to uncertainty in the calculation of the stopping powers of foils present for all three energies is less than $\frac{1}{2}\%$. The errors that are expected to be of importance are the systematic errors in the .005 and .010 inch aluminum plate stopping powers and the random uncertainty in the initial beam energy. The systematic uncertainty in the ratios E_1/E_0 and E_2/E_0 is about $1\%^{32}$. The uncertainty in the initial deuteron energy arises from variations in the cyclotron resonance situation. The value of the initial deuteron energy and its probable variation were arrived at on the basis of the long experience of the nuclear physicists using this cyclotron. The probable error in the value of the initial deuteron energy was estimated to be 2% . The total uncertainty in the ratios E_1/E_0 and E_2/E_0 is estimated to be about 3% .

D. Electrical Resistance

1. Measurement Technique

The electrical resistance of the metal under study was measured using the standard four terminal method. Connections were made to the ends of the sample wire and a known d.c. current passed through the wire. The voltage drop across a section of the sample wire between the current connections was measured using a type K-3, Leeds and Northrup

³²W. A. Aron, B. G. Hoffman, and F. C. Williams, Rept. ANOU-663, UCRL-121 (1949).

potentiometer. Thus, the potential contacts carry no current at potentiometer balance, and the resistance of the potential contacts affects only the sensitivity of the potential measurement.

The electrical resistance of a metal is due primarily to the scattering of conduction electrons by phonons; the residual resistance at absolute zero is due to lattice imperfections. This residual resistance is of the order of a few percent of the room temperature resistance, and it is this residual resistance that we expect to change with the introduction of radiation induced defects. In order to measure small changes in the residual resistance at high temperatures, it is necessary to either maintain the sample at a constant temperature or to be able to correct for temperature changes. The electrical resistance measurements on tungsten reported here were made at 195°K. The temperature coefficient of resistance in tungsten was measured to be 1.73%/°K between 77 and 300°K. In order to measure 1% changes in resistance with an uncertainty of less than 10%, the temperature variation had to be less than .05°K. With the experimental setup used for these measurements, this temperature constancy was impossible to achieve. Since the deuteron beam had to pass through the sample chamber, the sample chamber could not be immersed in the constant temperature bath. Instead, the sample chamber was placed in what was thought to be intimate thermal contact with the bath. In practice, ice formed at the bottom of the cold well and the temperature in the sample chamber would rise slowly with time. It was therefore decided to correct for temperature changes.

This temperature correction was accomplished by comparing the resistance of the tungsten wire sample under irradiation to that of an almost identical unirradiated tungsten wire. This unirradiated reference sample was mounted in such a way as to insure that the temperature

of the two samples were the same when there was no beam in the sample chamber. The measurement scheme is shown in figure 19. The sample (R) and the reference sample (RR) are placed in series. Contacts to R and RR were made as shown; metal A is Chromel and metal B is Alumel. The potentiometer could be switched to measure potentials V, VV, T_1 and T_2 . These measurements were made with the sample current I flowing first in one direction, then the other. Averaging these forward-reverse values of V and VV eliminated error due to contact potentials. Measurements of V and VV were made with no beam in the sample chamber, and it was assumed that the sample chamber was at a uniform temperature when no beam was present. The potentials T_1 and T_2 were measured with R under irradiation to give the sample temperature. (The thermocouples A and B were not exactly at the same point on the wire, but the resultant small IR drop was averaged out by the reversal of I.) To assure that the thermocouple-copper junctions were at a uniform temperature, these junctions were made to copper posts implanted in the massive copper sample base. These copper posts were electrically insulated from the sample base by Sauereisen cement. The potentials V, VV, T_1 , T_2 and the sample current I were measured using the switching circuit shown in figure 20.

It was assumed that the sample resistance could be written in the form

$$R(\phi, T) = \Delta R(\phi) + R(T) ,$$

where ϕ is the integrated deuteron flux incident on R. The quantity ΔR is some monotonic function of ϕ which is zero when ϕ is zero. The ratio $\gamma = R(0, T)/RR(T)$ was measured before irradiation. The radiation induced resistance change was then determined by

$$\Delta R(\phi) = R(\phi, T) - \gamma RR(T).$$

The ratio γ is just the ratio of the lengths of R and RR. For all samples studied, γ was kept within a few percent of one.

2. Uncertainty in the Measurement of Electrical Resistance

The sample current was chosen to be .010000 amperes. This value produced Joule heating in R resulting in a temperature rise of about .01°K. The initial values of R and RR were about .2 ohms so V and VV where about 2000 microvolts. An observer could estimate to $\pm .1$ microvolts on the potentiometer with the sensitivity available. Therefore the basic uncertainty in this resistance measurement was about 1 part in 10^4 . With the cyclotron oscillator turned off there was of the order of 1 microvolt difference between the forward and reverse values of V and VV. With the oscillator turned on this difference in forward-reverse values went up to 5 to 10 microvolts and the average values of V and VV with the cyclotron oscillator off and on differed by as much as 1 part in 10^3 . This effect was never understood, but it was eliminated by placing 1 microfarad ceramic condensers across V and VV where the leads come out of the cryostat. Based on a series of measurements of R and RR, the probable error in determining ΔR was found to correspond to ± 1 part in 10^4 .

3. Sample Mounting Technique for Electrical Measurements

The sample mounting scheme is shown in the sketch of figure 21. The sample wire is .0015 inch diameter tungsten wire supplied by Sylvania Company. This tungsten wire, (Sylvania number MS-50), had been cleaned, straightened and annealed in a reducing atmosphere at about 700°C. The sample wire was placed between the two vertical pillars of the lava sample mount at a height of 3/8 inches from the bottom, and was held in place by two dabs of Sauereisen cement. The left-hand continuation of the sample wire was then placed across the slot on the left-hand

pillar and again cemented in place. The right hand end of the sample wire was welded to one of the right hand Kovar connection posts; the left hand end of the sample wire was bent across and welded to the other Kovar post. To connect the .0010 inch diameter Chromel and Alumel leads to the sample wire, the sample mount was clamped in place, and the leads were brought into position with a micro-manipulator. The leads were welded to the sample wire and then cemented to the mount as shown in figure 21. When the cement was dried the free ends of the leads were released from the micro-manipulator. The proper positions for all wires was determined by scribe marks on the lava mount. All welding operations were carried out in air under a 20 power binocular microscope.

The connections described above were all butt-arc welds. The power for the arc welding was supplied by a condenser discharge. The use of a condenser discharge for welding small wires was suggested by Professor R. Craig of the Chemistry Department, University of Pittsburgh. The arc welder provided variable charging voltage, capacitance, and series resistance; the discharge was controlled by a foot switch. Best results were obtained using from 4 - 8 microfarads of capacitance charged to from 50 - 100 volts with no external series resistance. (Depending on its length, the lead wire of Chromel or Alumel provided of the order of 10 ohms series resistance.) The following procedure led to consistently good joints. Connection was made from one side of the arc welder to the sample wire by soft soldering to one of the sample wire Kovar posts. (One connection sufficed for all joints since the resistance per unit length of the tungsten was $\sim 1/10$ that of the Chromel or Alumel.) The lead to be welded was held in the manipulator by a clamp connected electrically to the other side of the arc welder. The lead was maneuvered into position on the mount with its end just

butted into the sample wire. It was then withdrawn slightly and the foot switch closed. The lead to be welded is then run into the sample wire and an arc occurs as they come together. This operation always results in the formation of a ball on the end of the lead wire, but no weld. The previous steps were then repeated and the second arc usually produced a good weld between the ball and the sample wire. An example of welds achieved with this technique is shown in the photograph of figure 22. The welds of the sample wire ends and the reference sample Chromel potential leads to their appropriate Kovar posts were made in the same way.

The completed sample mounting was then temporarily bolted to an aluminum base and annealed for one hour at 500°C in a hydrogen atmosphere. After annealing the sample mounting is bolted to the sample base and the collimator fixed in position. At this point the contacts I_1 , I_2 , AA_1 and AA_2 were ready for connection to the copper wires bringing these terminals out of the cryostat. The ends of leads A_1 , A_2 , B_1 and B_2 were free. These were then welded to heavy posts of the corresponding Chromel or Alumel metal. These thermocouple posts were silver soldered to copper posts which were in good thermal contact with the sample base as described previously. The eight contacts were then connected to the junction box on top of the cryostat with number 40 enamelled copper wires.

E. Mechanical Properties

1. Measurement of Internal Friction and Elastic Modulus

One general method for measurement of internal friction and elastic modulus involves setting up a simple mechanical resonance system where the resonance conditions involve the mechanical parameters of the

material under study. The geometry of the system chosen is dictated by the frequency range and the vibrational mode desired. In our experiment there was a further restriction. The tungsten sample had to be thin enough to permit passage of the incident deuterons through the sample with only moderate loss in energy. This was desirable so that the theory of defect production studied in the first part of this work could be used if needed to compute the radiation induced defect density. In addition, the sample mounting had to be small enough to fit into the sample chamber of the cryostat.

It was decided to use the same .0015 inch diameter tungsten wire for the mechanical studies that was used for the energy dependence work. The geometry chosen for the resonance system was that of a cantilevered rod vibrating in flexure. The measurement set up is shown schematically in figure 23. The transducer is a PZT ceramic bender bimorph supplied by Clevite Corporation. The bimorph is a rectangular parallelopiped with two ceramic sections sandwiched between 3 metal plates. The bimorph produces an e.m.f. between the outside plates when the bimorph is bent in a plane perpendicular to the plane of the metal plates. The forces of reaction of the vibrating sample on the transducer support produces a small strain in the bimorph which in turn produces an electrical signal proportional to the reaction force. One end of the sample is fixed to one of the metal plates with conducting cement. This plate is electrically grounded. A sinusoidal voltage of frequency $f/2$ is applied between a driver plate and the free end of the sample wire. The applied force on the end of the sample depends on the square of the applied voltage; therefore the oscillating component of this force will have a frequency f . The output voltage of the transducer is amplified by a variable frequency band pass amplifier tuned to frequency f .

This signal is fed to the vertical amplifier of a cathode ray oscilloscope and also to a voltmeter. The drive frequency is measured by a commercial frequency meter. The amplitude of vibration of the sample can now be measured as a function of frequency. The peak of this resonance curve gives the resonant frequency, and the width of the peak gives the damping $1/Q$ since

$$\frac{1}{Q} = \frac{f_2 - f_1}{f_0}$$

Here f_0 is the resonant frequency and f_1 and f_2 are the half power points. If the damping is very small, the resonance peak is very sharp, and the resonant frequency can be determined accurately. For this case the half-width is difficult to measure and a measurement of the logarithmic decrement δ is more precise. Figure 23 shows the scheme for measuring δ . The sample is made to vibrate at its resonant frequency. When the "transient start" switch is closed the mercury relay is energized. The mercury relay is a double pole throw switch which normally connects the drive plate to the drive voltage source and the scope trigger terminal to ground. When energized, the mercury relay grounds the driver wire making the drive force zero and initiates the oscilloscope sweep. The oscilloscope trace is photographed and the decay time constant (τ) of the exponential envelope of the trace can be determined from the photograph. The trace amplitudes were determined from the photographs using either the calibrated eyepiece of a low power microscope, or a drafting scale and a magnifying glass. The trace was superimposed in the photograph on a time scale available on the cathode ray tube face. Using the calibrating time scale on the Tektronix oscilloscope the logarithm of the amplitude was plotted versus time.

The decay time was computed from the slope of a straight line drawn through these experimental points. The exponential character of the decay reflected by this linear dependence was a constant check against spurious effects. For example the dependence of damping on vibrational amplitude would cause non-linearity in this slope. The logarithmic decrement is $\delta = 1/\tau_f$, and $\delta = \pi/Q$.

Consideration had to be given to the effect of the transmission characteristic of the band pass amplifier on the transient decay signal. The band pass of the amplifier was achieved using a simple RLC tuned filter. An analysis of the effect of this filter on the transient signal under study here is given in Appendix E. This analysis shows that the filter distorts the signal for a time $4\tau_f$ after the transient is initiated, where τ_f is the decay time constant of the filter alone. In most situations that were encountered in the measurement of damping, τ_f was $\ll \tau$, and the effect of the filter could be ignored. At worst, τ_f was of the order of $\tau/20$ and the data from the first part of the decay had to be ignored.

The fourth order equation of motion of a cantilevered rod can be solved analytically if the damping force is assumed proportional to velocity; this is done in Appendix A. The solution for the vibration amplitude as a function of applied frequency is given in equation (23) of this Appendix. The fourth order system is distinguished from the second order system by the fact that for a fourth order system the overtones are not harmonics of the fundamental resonant frequency. For high Q systems the frequency dependence of the amplitude reduces to the same form for both second and fourth order systems, namely

$$A(f) = \frac{A_0}{\sqrt{(\Delta f)^2 + D^2}} \quad (19)$$

Here $\Delta f = f - f_0$, A_0 and D are constants for a given mode depending on the damping, the driving force, and f_0 . A comparison between the theory of equation (19) and experimental results is shown in figure 24. For a cantilevered rod the fundamental resonant frequency $(f_0)_1$ is related to the elastic modulus by

$$(f_0)_1 = \frac{55966}{l^2} \sqrt{\frac{Ea^2}{4\rho}} , \quad (20)$$

where l and a are the length and radius of the circular rod respectively, and ρ is the mass density of the rod³³. The overtones of this system are related to the fundamental by

$$(f_0)_2 = 6.867 (f_0)_1 \quad (21)$$

$$(f_0)_3 = 17.548 (f_0)_1 \quad \text{etc.}$$

The ratio of the first overtone frequency to that of the fundamental was measured in all the samples studied. These ratios agreed with theory to better than 1%. In keeping with general practice, experimental results are given here either in terms of f_0 or Υ depending on which is more convenient.

There are disadvantages involved with the flexural mode of vibration chosen for this experiment. Even in uniform flexure the rod is strained non-uniformly. The strain varies linearly across the rod, going from a maximum in tension through zero at the median plane to a maximum in compression. For the cantilevered rod the flexure is not uniform, the strain will vary from a maximum at the clamped end to zero

³³P. M. Morse, Vibration and Sound, McGraw-Hill Book Company, Inc., New York, 1948, p. 158.

at the free end. The strain can be averaged over the rod, but there is some doubt about the proper way to take this average say in the case of strain dependent damping. In spite of the disadvantages of the flexure mode, and in view of the physical limitations of the experimental setup, it was thought that much information could be gained from this experiment that would still be amenable to theoretical interpretation. An attempt was made to avoid strain dependent effects in the mechanical parameters studied. This was done in general by making measurements at as low a vibrational amplitude as was possible with the measurement precision available. When possible, measurements were made of the variation of f_0 and δ with vibrational amplitude to insure amplitude independence. With a fixed sample geometry the only way in which δ could be measured as a function of frequency was to drive the sample at a succession of overtones. The transducer used for these measurements has a frequency response which is flat from zero to about 8 kc as shown in figure 25. The transducer sensitivity then goes through a large peak at about 16 kc and falls rapidly to zero for higher frequencies. Since the first overtone frequency for our sample was about 5 kc, the best we could obtain were measurements at the fundamental and the first overtone frequencies.

2. Uncertainty in the Measurement of Internal Friction and Elastic Modulus.

The basic random error in the measurement of the change in Young's modulus arises from the uncertainty in the determination of the applied frequency. The measurement of $f/2$ was made using a model 522B Hewlett Packard Electronic Counter. This instrument counts the unknown frequency signal for a prescribed time. This time is determined by a set of gate signals derived from an internal frequency standard. The uncertainty of this measurement is always \pm one count because of the

35

random phase difference between the gate signal and the input signal. The effect of this one count uncertainty on the precision of the frequency measurement was minimized by counting for long periods of time, the limitation being the frequency stability of the V.P.O. and at times the temperature stability of the sample. At frequencies of about 400 cps the general procedure was to count for 100 seconds. This gave an uncertainty of 2 parts in 4×10^4 . The uncertainty in determining the resonant frequency could be reduced to 1 part in 10^5 by plotting the resonance curve. For higher frequencies the uncertainty becomes proportionately less.

A large systematic change in f_0 was encountered whenever the sample was subjected to large vibration amplitude or to temperature cycling between 77 and 300°K. Since this effect was reduced by a factor of 5 when the positive meniscus between the conducting cement and the sample wire was eliminated, it is presumed that these changes in f_0 resulted from changes in the effective length of the sample rod. The size of this systematic error was about 1 part in 4×10^3 . This effect was not present as long as the sample temperature was constant and the vibration amplitude was small; therefore precise measurement of f_0 as a function of incident deuteron flux was still possible.

The sources of random error in the measurement of δ fall into two categories: (a) random noise and spurious modulations on the sample decay signal, and (b) random error in reading the amplitude versus time data from the photographs. The calibrations of the oscilloscope sweeps were checked regularly by photographing sinusoids of known frequencies. The contribution to the uncertainty in δ due to error in the time scale was negligible. The random noise in (a) was due primarily to microphonic excitation of the transducer. This was minimized by making

the sample frequency as low as possible, and the transducer resonant frequency as high as possible. At times an unwanted, low frequency modulation appeared on the sample signal. This modulation seemed to arise from the fact that the sample actually had two resonances corresponding to modes of vibration in the plane of the slight curvature of the sample rod and in a plane perpendicular to this one. The transfer of energy between these coupled modes resulted in a variation in amplitude. The resonant frequencies usually differed by about 2% although in one sample they differed by less than .01%. By positioning the drive wire one resonance could be accentuated over the other. Since the separation of these peaks was very much greater than the peak widths, no trouble was encountered in measuring the peak shapes. The modulation (from 1 - 10% of the sample signal) was more troublesome the closer the two resonant frequencies.

The uncertainty in δ was determined empirically by observation of the uncertainty in the slope of the semi-log decay plot. At best it was about $\pm 2\%$; in the worst cases it was about $\pm 5\%$.

It is assumed here that the damping measured in this experiment is due wholly or at worst primarily to internal friction in the sample metal. The possible sources of damping other than processes in the sample are the support and the atmosphere. The contribution to the damping of the atmosphere was eliminated experimentally. The damping measured with one atmosphere of pressure in the sample chamber was of the order of 5 times the damping observed at a pressure of 10^{-2} mm of mercury. No change in damping was observed between pressures of 10^{-2} and 10^{-4} mm of mercury. Measurements of damping reported here were all made at pressures $< 10^{-2}$ mm of mercury. The support damping was minimized by using a cement that dried to a very hard brittle state,

and by eliminating the positive meniscus between the cement and the sample rod as described below.

3. Temperature Measurement

The assumption was made, as in the electrical experiment, that the sample chamber is at uniform temperature when there was no beam in the sample chamber. The sample temperature was taken to be equal to the temperature of the sample base, and the base temperature was measured using a platinum resistance thermometer imbedded in the base. The resistance thermometer, supplied by Rosemount Engineering Company, is in the shape of a cylinder 7/8 inches long and 1/8 inch in diameter. The thermometer makes a tight sliding fit into its hole in the base; Apiezon-M vacuum grease is used as a transfer medium between the thermometer and the copper of the base. Two current and two potential leads are brought out of the sample chamber and the thermometer resistance was measured using the same resistance measuring apparatus described earlier. The manufacturer's resistance thermometer calibration was checked at liquid nitrogen, dry ice and ice temperatures. The random error in the temperature measurement was negligible, but there is a possibility of a small systematic error arising from a difference in temperature between the sample and the sample base.

Measurements were made of δ and f_0 for tungsten as a function of temperature between 77 and 300°K. This was done by letting the cryostat warm up after all the liquid nitrogen was evaporated. There is evidence that under these non-equilibrium conditions there was about a 2°K systematic difference between the sample and the base temperature, the sample being at the lower temperature.

All irradiations were made with one atmosphere of helium gas in the sample chamber to provide cooling for the sample. All measurements

of δ and f_0 were made at pressures $< 10^{-2}$ mm of mercury. The pump used to evacuate the region between the inside and outside walls of the cryostat was also used to evacuate the sample chamber for mechanical measurements. Difficulties arose when the sample chamber at one atmosphere was evacuated with the sample chamber at liquid nitrogen temperature. When the valve connecting the sample chamber to the cryostat vacuum system was opened the temperature of the sample base rose from 79°K to about 150°K in about 20 seconds and then dropped to within a few degrees of 79°K in about 2 minutes.

4. Sample Mounting Technique for Mechanical Measurements

a. The Sample Holder. The sample holder is shown in the photograph of figure 26. The transducer bimorph is fixed to the brass sample holder in the following way. The two outside metal faces of the bimorph are plated with Wood's metal over a small area near one end of the bimorph. One face of the bimorph is then soldered with Wood's metal to the sample holder at the proper height from the base of the sample holder. Electrical connection is now made from an insulated terminal on the sample holder to the other outside bimorph face. After a thorough cleaning, the soldered end of the bimorph is enclosed in insulating Sauerensen cement. The cement is then baked in air for 1/2 hour at 50°C . The bimorph is thus mounted as a cantilever with electrical connections available to its outside metal faces.

b. The Sample Mounting Operation. The sample wire is cut to proper length (~ 5 mm) on a flat hardened steel block using a razor blade. From this point on the sample is handled using a micro-manipulator. Fixed to the movable head of the manipulator is a device which provides a ball of Apiezon-W wax supported by a small heater coil. The wax ball is either liquid or solid depending on the position of an

external switch. The sample wire is nudged to the edge of the steel block and one end of the sample fixed in the pickup wax. The sample is then lifted horizontally off the steel block. Working under a binocular microscope, the operator carefully places a very small ball of Apiezon-W wax on the sample about in the middle of the wire. This is done by sliding a molten ball of wax off the end of a copper wire, (heated with a small soldering iron), onto the tungsten sample. During this operation the pickup wax softens slightly and the sample is no longer exactly horizontal. The manipulator is now turned and clamped so that what was previously the horizontal plane is now the vertical plane. The pickup wax is now molten and the sample wire, held by surface tension, plumbs to the proper alignment. In this position, a small soldering iron tip is brought near the wax ball in the middle of the sample rod. The ball melts and slides down the sample rod. It is allowed to slide until it gets to about 1/4" from the free end of the rod and then the heat is removed. Now this end is dipped into conducting cement (Ceram-Tech Conductalite) and the situation shown in the section sketch of figure 27 obtains.

Now the manipulator is returned to the horizontal plane and the sample holder clamped to the manipulator base. The bimorph is washed with benzene or toluene to remove the manufacturer's protective coating. The bimorph is now painted with a benzene solution of Apiezon-W everywhere but a small area of the free end of the metal face connected electrically to the sample holder. The sample is placed in position on the bimorph with the manipulator, and the prepared end of the sample is cemented to the transducer with Conductalite. When the cement has hardened, (it takes about 15 minutes to set), the pickup wax is melted and the pickup ball is removed. The sample holder with the sample in

in place is now placed in benzene to remove all of the Apiezon-W wax. It is washed in acetone and then clean alcohol. The sample holder is then baked in air at 50°C for 1/2 hour.

This technique results in a joint between the tungsten and the conducting cement that is a casting of the wax ball that was slid down the tungsten rod. Since the bottom of the wax ball makes a small positive meniscus with the rod, the cement makes a small negative meniscus with the rod. The shape of the cement casting can be seen in the photograph of figure 26.

c. The Drive Plate. The drive plate is made from number 40 copper wire rolled flat for a length of about .2 inches. The flat portion is .001 inches thick and about .020 inches wide. The drive plate is soldered directly to the center conductor of the coaxial cable that leads from the sample chamber to the junction box on the top flange of the cryostat. This center conductor is held in an insulating bushing cemented to a brass plate. This brass plate is bolted to a small manipulator which provides two dimensional Cartesian motion in a plane perpendicular to the plane of the sample rod. This motion is necessary to bring the drive plate close to the sample and to rotate the direction of the drive force to accentuate one of the two sample resonances.

d. Assembly Procedure. The sample base is first soldered to the bottom of the coolant well with Wood's metal. Then the resistance thermometer is slipped into place and connections made from the thermometer to the junction box on the top flange of the cryostat. The collimator and the drive plate manipulator are bolted to the base. The coaxial drive cable is attached to the insulating bushing on the manipulator and the drive wire is soldered to the center conductor of the drive cable. The drive plate is now bent into position roughly parallel to the

collimator face and about .06 inches away. The drive plate is then moved with the manipulator as far away from the collimator as possible. The sample holder is bolted in place with the sample rod parallel to the drive plate and about .04 inches from the collimator face. The sample holder is positioned so that the cemented end of the sample is just beyond the collimator opening. Looking through the collimator opening in the direction of the beam the only thing visible are the sample rod with the drive plate behind it. Now the sample signal cable from the junction box is bolted to the back of the sample holder with a bracket soldered to the shield of the cable. The center conductor of the signal cable is then soldered to the insulated terminal on the sample holder. Now the terminals on the junction box are connected by coaxial cables to the measurement apparatus shown in figure 23. The drive plate is moved to within .015 inches of the sample rod. The mechanical measurement apparatus is shown assembled in the photographs of figure 28. The sample resonance is found in the following way. The sample resonant frequency is known roughly from equation (19); the filter is set to pass this frequency. The gain of the system is turned up so that the oscilloscope displays mostly the electromagnetically induced V.F.O. frequency $f/2$. Now the V.F.O. is tuned until a signal at frequency f appears. This is the sample signal and it is then maximized by tuning the V.F.O. and the pass filter.

As was discussed earlier, two resonant frequencies were observed in all sample studied. At this point in the assembly procedure the drive wire is moved in small increments to accentuate one or the other of the two resonant frequencies. Now the copper sample can is temporarily soldered in place without aluminum foils on the beam windows. The cryostat is temporarily assembled without the Faraday cup chamber and

without the nickel foil on the beam entrance window. The alignment of the cryostat beam window-sample collimator system is checked optically using a cathetometer. The front slits are set in position so that the beam is confined to an area smaller than the windows but larger than the collimator opening. The positions of the front slits are marked with scratches and the slits removed. The cryostat is disassembled and the three beam window foils are mounted. The cryostat is then assembled and the front slits set in place. This alignment procedure was necessary only once; samples could be changed without realignment as long as the new samples were placed properly in the collimator opening, and the position of the collimator remained unchanged.

III. THE ENERGY DEPENDENCE OF RADIATION DAMAGE IN TUNGSTEN

A. Results

The method used for studying the energy dependence of radiation damage in tungsten is shown schematically in the exaggerated sketch of figure 29. The two smooth curves are damage curves, (plots of the fractional change in electrical resistance as a function of integrated incident deuteron flux), for two incident energies. The expectation of the non-linearity of these damage curves is based on published damage curves for deuteron irradiated copper³⁴, and neutron irradiated tungsten³⁵. The resistance change in tungsten was measured for small increments of incident flux, alternating between two incident energies. An example of these data is shown in figure 30. This plot shows the change in the slope of the damage curve with a change in the incident energy. The slope (m) of the damage curve is defined as

$$m = \frac{d(\Delta R/R_0)}{d\phi} ; \quad (21)$$

where R_0 is the unirradiated tungsten sample resistance at 195°K, and ϕ is the integrated incident deuteron flux. Based on a series of short irradiations such as those of figure 30, the dependence of m on ϕ was measured for incident energies $E_0 = 13.7$ mev and $E_2 = 10.3$ mev. These data are shown in figure 31. Let us number the measured damage slopes of figure 31 as: $m_1(E_0)$, $m_2(E_2)$, $m_3(E_0)$, $m_{i-1}(E_0)$, $m_i(E_2)$ Then we may define the ratios

³⁴M. G. Cooper, J. S. Koehler and J. W. Marx, Phys. Rev. 97, 599 (1955).

³⁵M. W. Thompson, Phil. Mag. 5, 278 (1960).

$$\gamma_{2-} = \frac{m_i(E_2)}{m_{i-1}(E_0)} ,$$

and

$$\gamma_{2+} = \frac{m_i(E_2)}{m_{i+1}(E_0)} .$$

Since the slope of the damage curve decreases with ϕ and therefore with the index i , γ_+ should always be greater than γ_- . We may now define a ratio γ_2 which is just

$$\gamma_2 = \frac{\gamma_{2+} + \gamma_{2-}}{2} .$$

The data of figure 31 are expressed in terms of γ_2 in the graph of figure 32. The frequency distribution of these experimental values of γ_2 is shown in figure 33. From the average and the standard deviation of this distribution we get that $m(E_2)/m(E_0) = 1.43 \pm .02$. This value is in agreement with an earlier, less precise measurement of this ratio, i.e. $m(E_2)/m(E_0) = 1.45 \pm .05$.

The radiation effects data shown in figure 30 and 31 were adjusted to show the shape of the overall damage curve for incident energy E_0 using the known value of $m(E_2)/m(E_0)$. This corrected damage curve is shown in figure 34.

Still using the same sample, the slope m was measured as a function of ϕ between incident energies E_0 and $E_1 = 12.1$ mev. An example of these damage curves is shown in figure 35. Measured values of m as a function of ϕ for energies E_0 and E_1 are shown in figure 36. The ratio γ_1 is defined as before for incident energies E_0 and E_1 . The values of γ_1 determined from the data shown in figure 36 are given in

figure 37. The frequency distribution of γ_1 is shown in figure 38. From the average and the standard deviation of this distribution we get that $m(E_1)/m(E_0) = 1.16 \pm .01$.

The experimental values of $m(E)/m(E_0)$ are plotted in figure 39 as a function of E/E_0 . The theoretical curves of figure 39 are based on the theory of defect production outlined in the Introduction, with the assumption that $m(E)/m(E_0) = \sigma(E)/\sigma(E_0)$. Curve (a) is drawn for $\sigma(E) = \sigma_d(E)$, where, from equation (6), $\sigma \propto 1/E$. Curve (b) is drawn for $\sigma(E) = \sigma_d(E)\bar{\nu}(E)$, where, from equations (6) and (9), $\sigma \propto (1/E)(1 + \ln \xi E)$. Both the theoretical curves of figure 39 include a correction of about 3% in the ordinate for the degradation in deuteron energy in passing through the sample. Since the incident deuteron energy is degraded by about 2 mev in passing through the .0015 inch diameter tungsten wire, and since the cross section for producing defects goes roughly as $1/E$, a greater resistance change is expected at the back of the sample wire than in the front. In Appendix E the change in resistance of the sample is computed for a given incident energy and energy loss in the sample. The effective energy E_p is defined as the energy a deuteron would have to have to produce this same resistance change if no degradation in incident energy took place. The effective energy E_p is related to E and the energy loss in the sample in Appendix E. The theoretical curves of figure 39 were based then on $\sigma(E) \propto 1/E_p$ in curve (a) and $\sigma(E) \propto (1/E_p)(1 + \ln \xi E_p)$ in curve (b). The energy losses were computed using published Range-Energy tables³². The range of the tungsten sample was expressed in terms of its mass per unit area.

³²op. cit., W. A. Aron et al.

The energy loss for this range was read from the tables for lead. The uncertainty in determining the energy loss in the sample is estimated to be about $\pm 5\%$.

During irradiations the sample temperature rises varied between 4 and 10°K , and were proportional to beam intensity. Measurements were made with a range of beam intensities from 4 to 10×10^{12} deuterons/sec/cm². No obvious indication of an effect of beam intensity on the parameters measured was detected, although no systematic investigation of this effect was made.

The energy dependence of radiation damage in tungsten observed by Pearlstein et al.³⁶ is given in figure 40. In this graph Pearlstein's data are compared with an extrapolation of the data reported here. This extrapolation is based on an approximate description of our data, namely $m \propto 1/E$. It was necessary to correct our data to be commensurate with Pearlstein's results. Pearlstein's data were taken with bombarding protons, where ours were taken with deuterons; his results are quoted in terms of fractional changes of room temperature resistance, where ours are given in terms of resistance at 195°K . It can be seen from equations (4) and (6) that protons of a given flux and energy will produce $1/2$ the damage produced by deuterons of the same flux and energy. (Note that M_1 in equation (4) is essentially one for protons and two for deuterons.) The fractional change in room temperature resistance was taken to be $2/3$ the fractional change of resistance at 195°K , just the approximate ratio of the resistances of tungsten at 195°K and 300°K .

³⁶J. J. Harwood, H. H. Hausner, J. G. Morse, W. G. Ranch, The Effects of Radiation on Materials, Reinhold Publishing Co., New York, 1958, p. 150.

Our data for $m(E)$ were therefore multiplied by a factor of $1/3$ to get the extrapolation shown in figure 40.

B. Discussion of the Energy Dependence Results

The general shape of the damage curve for tungsten reported here (figure 34) is in agreement with data reported by M. W. Thompson³⁵ for neutron irradiated tungsten. It should be noted from the data of figures (31) and (36) that there was no linear region in the damage curve near the origin that was detectable with this experiment. For integrated flux out to 4×10^{17} deuterons/cm² no indication of saturation of the damage curve was observed. The lack of linearity near the origin indicates that (a) some sort of annealing is taking place, and/or (b) some sort of interaction of defects is taking place, so that the resistance change is not proportional to the total number of radiation induced defects.

For $E_0 = 13.7$ mev, the value of σ_d from equation (6) is $\sigma_d = 1.15 \times 10^{-20}$ cm². The first two experimental points of figure 31 for E_0 show a 10% change in damage slope for an incident flux of $.5 \times 10^{16}$ deuterons/cm². The volume density of primary knock-on interstitials is $N_p = \sigma_d \phi n_0$, where n_0 , the number of tungsten atoms per unit volume, has the value $.62 \times 10^{23}$ cm⁻³. Our first measured slope, where the slope seems already to depend on ϕ , corresponds to $N_p = 3.5 \times 10^{18}$ cm⁻³. If these primary knock-on collisions are distributed uniformly through the lattice, then their average spacing is about 65 \AA or 20 lattice spacings. Inclusion of the knock-on progeny would make the average defect separation about 12 lattice spacings.

³⁵op. cit., M. W. Thompson.

The closeness of radiation induced defects even for our lightest irradiations supports the interaction hypothesis suggested in (b) of the preceding paragraph.

The results of the energy dependence investigation are summarized in figure 39. If the assumption that $m(E)/m(E_0) = \sigma(E)/\sigma(E_0)$ is valid, then these data show that σ varies almost as $1/E$ for the conditions of this experiment. From the theory of defect production outlined in the Introduction, we get that $\sigma = \sigma_d \bar{\nu}$, and that $\sigma_d \propto 1/E$. Therefore, we may conclude that any mechanism proposed for secondary defect production would have to have a weak incident energy dependence when averaged over a coulomb recoil spectrum.

The small deviations of the experimental results from the $1/E$ coulomb energy dependence (figure 39) are about twice the experimental error and in a direction opposite to that predicted by the hard sphere model yield function energy dependence. It should be noted however that no attempt was made here to include in the theoretical curves the effect of thermal spikes on the hard sphere yield function. The thermal spike is the result of a high energy knock-on atom making a series of glancing hard sphere collisions with lattice atoms near the end of its trajectory. These collisions transfer energies less than E_d to the lattice atoms and result in a large temperature rise in the region around the end of the primary atom's trajectory. These thermal spikes may produce annealing of displaced atoms.

The function $d\sigma_d/dT$ is given in equation (3). This function is shown in the sketch of figure 41 for incident energies E_0 and E_1 , where $E_0 > E_1$. From equation (5) the cross section for production of primary knock-on atoms is the area under this curve between E_d and T_m . Higher energy incidents produce fewer knock-ons, but produce a larger fraction

of high energy knock-ons. Therefore we expect more radiation annealing from high energy incident particles than from low energy incidents. Koehler³⁷, using detailed data by Corbett *et al.*³⁸ on low temperature annealing of electron induced radiation damage in copper, has corrected the simple hard sphere yield function for the annealing effect of thermal spikes. Similar detailed data for tungsten would be required to make such corrections here. Such data is not available; we can only say that these corrections would tend to improve agreement between the theory and experiment of figure 39.

The change in electrical resistance of the irradiated sample is a function of the number of radiation induced defects N . We may relate m to σ by writing

$$m = \frac{d \Delta R/R_0}{d\phi} = (1/R_0) \frac{d \Delta R(N)}{d\phi} = (1/R_0) \frac{d \Delta R(N)}{dN} \frac{dN}{d\phi} .$$

Since $N \propto \phi$, this reduces to

$$m \propto \frac{d \Delta R(N)}{dN} \sigma .$$

The assumption that $m(E)/m(E_0) = \sigma(E)/\sigma(E_0)$ then reduces to the assumption that $d \Delta R(N)/dN$ is independent of incident energy. We expect that this term may have some dependence on the incident energy in the following way. The resistance change for a given number of defects will depend on the nature of the defects. For example, two radiation induced

³⁷J. S. Koehler, Bull. Am. Phys. Soc. 5, 175 (1960).

³⁸J. W. Corbett, R. B. Smith and R. M. Walker, Phys. Rev. 114, 1452, 1460 (1959). J. W. Corbett and R. M. Walker, Phys. Rev. 115, 67 (1959).

vacancies might be expected to scatter conduction electrons differently depending on whether they exist widely separated or close together. The arrangement of the defects might be expected to depend on the energy of the knock-on atom which gave rise to these defects. It has been found, however, that the electrical resistance change per defect in copper differs only by a factor of 2 between irradiation by 1 mev electrons and 10 mev deuterons³⁹. Since 1 mev electrons are barely able to create displacements by head-on collisions, these defects are known to be isolated from one another. This is in contrast to the clustering of defects we are concerned with for irradiation by 10 - 14 mev deuterons. Therefore, we do not expect $d \Delta R(N)/dN$ to have a strong incident energy dependence compared with $\sigma(E)$ over the range of energies studied here.

Our results in the 10 - 14 mev range of incident energy show the expected $1/E$ dependence for the radiation damage slope. This is in contrast to the results of Pearlstein et al shown in figure 40. The extrapolation of our data from 14 mev to hundreds of mevs cannot be relied on quantitatively, but it is of heuristic value. The extrapolation of the $1/E$ dependence shows that in the 100 - 400 mev range the contribution of coulomb scattered knock-on atoms to the resistance change in tungsten is expected to be small compared with the resistance change observed by Pearlstein. It is expected, then, that the large effects seen by Pearlstein are due to some mechanism other than elastic collisions with the incident particle. Our results then support

³⁹A value of $1.5\mu \text{ ohm-cm}/\text{at. \% defects}$ was deduced by Corbett, Denny, Fiske and Walker, Phys. Rev. Rev., 108, 954 (1957). A value of $3.0\mu \text{ ohm-cm}/\text{at. \% defects}$ was deduced by Magnuson, Palmer and Koehler, Phys. Rev. 109, 1990 (1958) for 10.7 mev deuteron bombardment of copper. Magnuson et al used data by Cooper et al³⁴ and R. W. Vook and C. A. Wert, ibid, 1529 (1958).

³⁴op. cit., H. G. Cooper et al.

Pearlstein's conclusion about the predominant effect of nuclear spallations for 100 - 400 mev proton bombardment of tungsten.

IV. EFFECTS OF RADIATION ON THE MECHANICAL PROPERTIES OF TUNGSTEN

A. Results

1. The Pre-Irradiation Bordoni Peak

The results of measurements of δ as a function of temperature on four unannealed tungsten samples are shown in figure 42. Although the detailed shape of $\delta(T)$ varies from sample to sample, the characteristic peak at about 140°K is quite reproducible. The peaks widths are $\sim 60^{\circ}\text{K}$, and in fact seem to be made up of two unresolved peaks, the principal one at 140°K , and a secondary peak at 100°K . In terms of the peak widths and peak temperatures, these results are similar to results obtained for face centered cubic metals⁹. Measurements of $\delta(T)$ for several body centered cubic metals have been made very recently by Chambers and Schultz¹⁵. They observe a peak in $\delta(T)$ for cold worked polycrystalline tungsten at about 170°K and 15,000 cps. Their peak height in δ is about 1.5×10^{-3} compared with our peak heights of from .7 to 1.0×10^{-3} .

Figures 43 and 44 show $\delta(T)$ measured here at the fundamental and the first overtone frequencies for two samples. If the peaks in $\delta(T)$ observed here and by Chambers and Schultz are the result of a relaxation process with a single activation energy, then the frequency of measurement and the peak temperature will be related by equation (18). Figure 45 shows the experimental results of figures 42, 43 and 44, along with the measurement of Chambers and Schultz, plotted as $\ln f_0$ vs $1/T_{\text{peak}}$. A fit of these data to the relationship of equation (18) gives an

⁹ op. cit., For a review of this work see D. H. Niblett and J. Wilks, Adv. in Phys. 9, 1 (1960).

¹⁵ op. cit., R. H. Chambers et al.

activation energy $H = .21 \pm .05$ ev, and an attempt frequency $A \approx 1.5 \times 10^{10}$ cps.

2. The Effect of Irradiation at 300°K on Internal Friction and Young's Modulus

Figure 46 shows the effect of a room temperature irradiation of 2×10^{16} deuterons/cm² on the temperature dependence of δ for tungsten sample MW8. These data were observed at the fundamental resonant frequency. The height of the pre-irradiation Bordoni peak has been reduced, and a series of four smaller, sharper peaks have appeared. The post-irradiation measurements of $\delta(T)$ for sample MW8 made at the fundamental and the first overtone frequencies are compared in figure 47.

The four peaks in the first overtone data are shifted to higher peak temperatures by 10-20°K with respect to the peaks observed at the fundamental frequency. The first overtone peak III is almost an order of magnitude higher than the other internal friction peaks. Figure 48 shows a detail of peak III at the first overtone frequency for several values of maximum vibrational amplitude; figure 49 gives similar data for peak III at the fundamental frequency. Figure 50 compares the pre-irradiation measurements of $\delta(T)$ for sample MW9 with $\delta(T)$ observed after a room temperature irradiation of 8×10^{16} deuterons/cm². The data of figure 50 were taken at the fundamental frequency. Note from figure 42 that the height of the Bordoni peak for MW9 is $.7 \times 10^{-3}$ compared with $.9 \times 10^{-3}$ for MW8. In this case the pre-irradiation Bordoni peak is not reduced, but is broken up into sharper peaks as was observed for MW8. The pre-irradiation Bordoni peak for MW9 is compared with the post-irradiation measurements of internal friction for the first overtone frequency in figure 51. Here, the α radiation has reduced the original Bordoni peak height. In this plot there is more fine structure

than had been observed in MW8, but there are four major peaks that can be identified. Figure 52 shows a comparison of the post-irradiation data for $\delta(T)$ of MW9 at the fundamental and the first overtone frequencies. A comparison of the post-irradiation data for $\delta(T)$ of samples MW8 and MW9 at the fundamental frequency is shown in figure 53; a similar comparison is made for the first overtone frequency in figure 54. The very large height of peak III observed in MW8 was not reproduced in MW9.

Measurements were also made on MW8 and MW9 of δ and f_0 as a function of integrated deuteron flux at room temperature. Figure 55 gives δ and the percentage change in resonant frequency ($\Delta f_0/f_0$) as a function of flux for MW8. The internal friction decreases and the elastic modulus increases with incident flux, the effect saturating at about 1×10^{16} deuterons/cm². Similar data for MW9 are shown in figure 56. The effect of extended irradiation on δ and $\Delta f_0/f_0$ is shown for sample MW9 in figure 57. The saturation value of internal friction is unaffected by extended irradiation, but $\Delta f_0/f_0$ starts to drop off linearly with incident flux for $\phi > 1 \times 10^{16}$ deuterons/cm². The slope of this high flux curve for $\Delta f_0/f_0$ is $.011\%/10^{16}$ deuterons/cm². From equation (20) we get that the rate of change of $\Delta Y/Y$ with incident flux would be just twice this value or $.022\%/10^{16}$ deuterons/cm².

3. Irradiation at 79°K and the Effect of Annealing on Internal Friction

Ten measurements of δ and f_0 were made on sample MW6 at 79°K as a function of incident flux up to a flux of 1×10^{15} deuterons/cm². No change in δ or f_0 was detectable with our apparatus for this amount of bombardment. Subsequent to this irradiation, $\delta(T)$ was measured for MW6 as the sample annealed to room temperature. These data are compared

with the pre-irradiation and post anneal temperature dependences of δ in figure 58. It is of interest to note that the structure present in $\delta(T)$ during the anneal is not present either before irradiation or after the sample had warmed to room temperature. An attempt was then made to repeat this experiment. Sample MW9 was given an uninterrupted irradiation of 2×10^{15} deuterons/cm² at 79°K. Measurements of δ were then made as the sample warmed to room temperature. The measured values of δ during the anneal are compared with the pre-irradiation curve for $\delta(T)$ in figure 59. Sample MW9 remained at room temperature for 24 hours and then $\delta(T)$ was measured subsequent to the anneal. These post-anneal data are compared with the pre-irradiation data for $\delta(T)$ in figure 60. The generally large internal friction and the temperature dependent structure of this internal friction observed during the anneal of lightly irradiated sample MW9 were no longer present after warm up to room temperature.

4. The Temperature Dependence of the Resonant Frequency

Measurements of $f_o(T)$ were made simultaneously with measurements of $\delta(T)$. A typical curve for $f_o(T)$ is shown in figure 61. The slope of $f_o(T)$ was reproducible for a given sample to about $\pm 1\%$ for both the fundamental and first overtone frequencies. The average slope $d(\Delta f_o/f_o)/dT$ for the four samples studied was $.50 \times 10^{-4}/^{\circ}\text{K}$, with a maximum deviation of about 4%. This gives a value for $d(\Delta Y/Y)/dT$ for tungsten between 79 and 300°K of $.96 \times 10^{-4}/^{\circ}\text{K}$ with a percentage error of $\pm 4\%$. (The coefficient of thermal expansion contributes $.04 \times 10^{-4}/^{\circ}\text{K}$ to the measured value of $d(\Delta f_o/f_o)dT$).

No provision was made in the measurement of mechanical properties as a function of irradiation for direct observation of the sample

temperature during irradiation. Since the sample diameter was the same as it was in the measurement of electrical resistance, and since both irradiations were carried out in one atmosphere of helium, it was assumed that the same temperature rises were experienced for a given beam intensity in both cases. It was possible, however, to estimate the sample temperature rise during irradiation with the mechanical measurement apparatus in the following way. The value of f_0 was measured both with and without irradiation. From the known value of the temperature coefficient of f_0 the temperature of the sample was then computed. This provided only an estimate because f_0 could not be determined with as much precision as it could be with no beam in the sample chamber. The sample vibration signal was partially obscured when the beam was in the sample chamber by pick-up of the direct driving signal; this occurred probably because the ionized gas provided a conducting path between the drive plate and the sample wire. The result of this estimate agreed with the temperature rises measured in the electrical resistance experiment.

R. Discussion

It is helpful in interpreting and understanding the results presented here, on the effect of irradiation on the mechanical properties of tungsten, to know something about the temperature at which radiation induced defects become mobile. Studies of radiation induced defect annealing have been made for tungsten by Kinchin and Thompson⁴⁰. Their results show a very complex annealing temperature spectrum for defects. In spite of this complexity, their measurements lead to the following

⁴⁰C. Kinchin and M. W. Thompson, *J. Nuclear Energy* 6, 275 (1958).

hypothesis. Interstitials start becoming mobile at about 80°K, and are essentially gone at 300°K, while vacancies anneal out at about 600°K. This would mean that, for tungsten at 79°K, radiation induced interstitials are barely mobile, and radiation induced vacancies are frozen into the lattice. For tungsten at 200°K, radiation induced interstitials are completely mobile and presumably migrate to sinks such as dislocation lines, while vacancies are still immobile.

1. The Pre-Irradiation Bordoni Peak

The data of figures 42, 43 and 44, along with the measurement by Chambers and Schultz¹⁵, establish the existence of a peak in the temperature dependence of internal friction in tungsten. The association of a relaxation phenomenon with the observed peak is based on the dependence of peak temperature on frequency shown in figure 45. The fit of the data of figure 45 to a single activation energy relaxation model is much better than a similar fit for copper²².

Not all of the properties of Bordoni peaks, summarized for face centered cubic metals on pages 8 and 9 of the Introduction, were investigated for the tungsten peak reported here. The effect on the relaxation peak in tungsten of the polycrystalline state of the sample, the cold work history of the sample, and the impurity content of the sample were not investigated. Pre-irradiation measurements of $\delta(T)$ for tungsten were made here for several values of strain amplitude in the range 5×10^{-7} to 5×10^{-6} . No change in $\delta(T)$ was observed for these strain amplitudes. This range of strains was chosen, however, such that

¹⁵ op. cit., R. H. Chambers *et al.*

²² Composite values of H and A based on the work of several investigations are given in reference 9, p. 27.

no strain amplitude dependence of δ and f_0 was observed at 79°K and 300°K. What has been found for copper, for example, is that for strains large enough to increase the background friction, no change in the height of the Bordoni peak relative to the background is observed. This behavior was not investigated for the tungsten peak. The association made here, of the Bordoni-dislocation relaxation model proposed⁹ for face centered cubic metals, with the peak in $\delta(T)$ for tungsten, is based on: (a) the existence of the peak, (b) the peak temperature shift with frequency change, and (c) the reduction in peak height by irradiation. This latter effect is discussed the next section.

2. The Effect of Room Temperature Irradiation on the Bordoni Peak.

The effect of room temperature irradiation on $\delta(T)$ in tungsten was shown for samples MW8 and MW9 in figures 46, 50 and 51. In figure 46 we see an appreciable reduction in the Bordoni peak height and the appearance of some new structure in $\delta(T)$ for MW8 after an irradiation of 2×10^{16} deuterons/cm². Sample MW9 was subjected to a flux of 8×10^{16} deuterons/cm². Figures 50 and 51 show the effect of this irradiation on the Bordoni peak observed at the fundamental frequency and the first overtone frequency respectively. There is a reduction in the peak height for the first overtone, but none for the fundamental. As was true for the pre-irradiation curves of $\delta(T)$, the post-irradiation curves of $\delta(T)$ reproduce for different samples in general shape, but not in detail. The variations in both the pre- and post-irradiation results probably arise from the fact that little attempt was made to control

⁹op cit., D. H. Niblett et al.

the cold work state of the samples. The samples were not annealed*, and, although they were handled with reasonable care, they did get strained in preparation. Hence the cold work induced dislocation density could vary widely in the samples studied.

The fact that the reduction in Bordoni peak height of MW8 was not reproduced for the fundamental frequency in MW9 is a little surprising. If radiation induced interstitials are mobile at 300°K, and they do migrate to dislocations, and they do pin these dislocations, then the average free length (L) of the dislocation will be decreased by irradiation. Seeger's theory for the dislocation relaxation peak in $\delta(T)$ predicts that the peak height will go as L^3 . (See equation (17).) If this theory is correct, then irradiation of tungsten at 300°K should reduce the height of the Bordoni peak. The two cases (figures 46 and 51), which do show a reduction in the Bordoni peak height, support the dislocation relaxation theory. The fact that the peak height was not reduced in the data of figure 50 is probably attributable to the appearance of the post-irradiation structure. If the heights of the post-irradiation peaks are increasing with flux while the pre-irradiation peak height is decreasing, then the situation of figure 50 could obtain. In addition it should be noted that the pre-irradiation Bordoni peak height was higher in MW8 (figure 46) than it was in MW9 (figure 50). This would indicate that MW8 had a higher dislocation density than MW9 before irradiation.

*The tungsten wire supplied by Sylvania had been annealed, but it had then been wound on a mandrel suffering some plastic strain.

The structure in the post-irradiation curves of $\delta(T)$ is of great interest. Figure 47 shows the post-irradiation data for MW8 taken at the fundamental and the first overtone. There are four small peaks observed at the fundamental frequency. There are also four peaks discernible in $\delta(T)$ for the first overtone. The four peaks observed at the first overtone are clearly associated with the four peaks seen at the fundamental. The shift in the peak temperature with the increase in frequency again suggests that the peaks arise from some sort of relaxation process. These post-irradiation peaks could be a resolution of the original Bordoni peak as a result of dislocation pinning by interstitials, or these peaks might arise in some way from radiation induced defects alone. This latter mechanism would probably involve radiation induced vacancies left throughout the lattice at 300°K. The only property of the post-irradiation peaks shown in figure 47 that does not fit the relaxation theory outlined in the Introduction is the large height of peak III at the first overtone frequency. We do not expect any change in peak height with frequency change for a relaxation peak. Another property of peak III at the first overtone that was different from the rest of the post-irradiation peaks was that the height of peak III was strain amplitude dependent. Peak III at the first overtone is shown in Figure 48 for several values of vibration amplitude for which the rest of $\delta(T)$ was unchanged. (The shift in peak temperatures shown in the detailed plot of figure 48 is not considered to be a function of amplitude. The shifts represent a change in the systematic error in the measurement of temperature mentioned earlier for these three experimental runs.) Note that in figure 49 no change in peak III at the fundamental is observed with a change in amplitude.

The data discussed above was taken on sample MW8 after a room temperature irradiation of 2×10^{16} deuterons/cm². This experiment was repeated on sample MW9 for a flux of 8×10^{16} deuterons/cm². The post-irradiation curves $\delta(T)$ taken at the fundamental frequency for the two sample MW8 and MW9, are compared in figure 53. The shapes of these curves are quite similar, especially for peaks I, II and III. A similar comparison is shown in figure 54 for the first overtone frequency. Here there is again agreement in the general shape of the curves, but peak III for MW9 is an order of magnitude smaller than it is for MW8.

One reason for the lack of reproducibility in the height of peak III could be that the peak height is extremely frequency dependent, since the two samples did differ in resonant frequency by about 2%. Another possibility is that the large peak height observed for MW8 was spurious, introduced in some way by the measurement apparatus. However, no mechanism for the spurious introduction of this large peak has been found to date. Although a spurious origin remains a possibility, it is thought that peak III observed for MW8 is real. From the shift in post-irradiation peak temperatures with frequency change shown in figure 47 we may make estimates of H and A for these post-irradiation peaks. These estimates are very rough; very little data is available, and some of the post-irradiation peaks are poorly defined. The estimated values of H and A for sample MW8 are given in the table below.

Peak	Activation Energy H(ev)	Attempt Frequency A(cps)
I	.21 \pm .02	$10^{12.3} \pm 1.0$
II	.19 \pm .04	$10^{9.6} \pm 1.5$
III	.27 \pm .04	$10^{10.3} \pm 1.5$
IV	.47 \pm .15	$10^{11.1} \pm 2$

To sum up this part of the discussion, it can be said that a room temperature deuteron irradiation in general reduces the height of the Bordoni peak in tungsten. After irradiation, the internal friction as a function of temperature exhibits a series of narrow peaks. It was suggested that these narrow peaks are possibly a resolution of the pre-irradiation Bordoni peak as a result of dislocation pinning by radiation induced interstitials. It was pointed out that if this is true, then the post-irradiation peaks should also be described by the dislocation-relaxation theory. The unusual height of peak III contradicts this theory, but this piece of experimental evidence has not been confirmed. It was also pointed out that the peaks might arise from the presence of unannealed, radiation induced vacancies alone.

3. The Effect of Room Temperature Irradiation on the Background

(Strain Independent) Internal Friction

Figures 55 and 56 show δ and $\Delta f_0/f_0$ measured as a function of incident flux at room temperature. The internal friction decreases and Young's modulus increases with incident flux. This effect saturates at about 1×10^{16} deuterons/cm². These data are similar to $\delta(\phi)$ and $\Delta f_0(\phi)/f_0$ measured at room temperature by other workers for copper^{23,24}, although the total change at saturation for copper is very much greater. Thompson and Holmes²³ observed, at saturation, an increase in $\Delta f_0/f_0$ of 1-2%, and a decrease in δ by a factor of 7. It should be noted that the internal friction in copper is of the order of ten times greater than that of tungsten. It appears then that we are observing, in tungsten,

²³op. cit., D. O. Thompson et al.

²⁴op. cit., D. H. Niblett et al.

the pinning of dislocations by radiation induced interstitials. The fact that the total effect in tungsten is so much smaller than it is in a "soft" metal like copper probably indicates that the dislocations in tungsten are already fairly well pinned before irradiation. It is possible that we are observing the removal of most of the dislocation damping by irradiation, and that the internal friction that is left arises from some other mechanism.

We have hypothesized that room temperature irradiation leaves only vacancies in the lattice for tungsten; we then have an opportunity to test Dienes' theory²⁷ for the change in the elastic properties of a metal with vacancy density. Dienes predicts that vacancies will produce a "bulk" effect, that is, one atomic percent of vacancies should produce a 1% decrease in Young's modulus. The data of figure 57 shows that heavy room temperature irradiation produces no change in δ (after the initial decrease), and that there is a linear decrease in $\Delta\epsilon_0/\epsilon_0$ with flux (after the initial increase). The slope of this curve in terms of $\Delta Y/Y$, the fractional change in Young's modulus, is .022% / 10^{16} deuterons/cm². We may calculate the density of vacancies produced by a flux of 10^{16} deuterons/cm² in tungsten for incident energy 13.7 mev from equation (11) and $x = \alpha\phi$, where x is the atomic fraction of vacancies. We get that $x = .05\%$ for 10^{16} deuterons/cm². These results give .44% decrease in Young's modulus per atomic percent of vacancies compared with Dienes' prediction of 1.0%. This agreement is actually good, considering the approximate nature of Dienes' treatment of the problem.

²⁷ op. cit., G. J. Dienes.

4. The Effect of Irradiation at 79°K on Internal Friction

Tungsten sample MW6 was lightly irradiated at 79°K. Measurement of $\delta(T)$, as this sample warmed to room temperature, indicated some structure in $\delta(T)$ superimposed on the pre-irradiation Bordoni peak. (See figure 58.) A post-anneal run showed $\delta(T)$ just below the pre-irradiation curve with no indication of the structure observed during the anneal. It was thought that this internal friction structure might arise from the migration of radiation induced interstitials. The model could be as follows. Interstitials, or clusters of interstitials might tend to reorient themselves into a lower energy configuration under an applied stress. In a body centered cubic metal, even single interstitials tend to reorient themselves under an applied stress. If an interstitial is located in the center of a (100) cube edge, and a compressive stress is applied in the (100) direction, then the interstitial will prefer the (010) or (001) cube edge position. The reorientation process is again pictured as a relaxation process, characterized by a frequency which is dependent on the temperature of the lattice.

When the irradiation of MW6 was performed, we were looking for a change in δ with incident flux at 79°K. No change was observed, but in the process of measuring δ after each of the ten exposures, the sample was subjected to an anneal to about 150°K. We decided to give sample MW9 roughly the same irradiation dose as was given to MW6 without the intermediate anneals. Sample MW9 received only one anneal to 150°K as the sample chamber was pumped out after the irradiation. It was expected that the structure seen in MW6 would be greatly accentuated in MW9. This was in fact what we saw in the data of figure 59. The post-anneal run on MW9 exhibited no structure; figure 60 shows that the post-anneal

It is natural to ascribe this structure to the stress-induced reorientation of defects for resistivity measurements show appreciable annealing between 77°K and room temperature. The extreme sharpness of these peaks, however, casts considerable doubt on this interpretation. With nominal activation energies, the narrower peaks require an attempt frequency of $A \sim 10^{20} \text{ sec}^{-1}$. This is prohibitively high. While similarly sharp peaks are reported in the literature^{12,41,42} for face centered cubic metals, the present results on Tungsten have not been reproducible. It therefore seems most probable that the peaks are a spurious result caused by unexplained resonances in the apparatus or by radiation induced changes in the sample-mounting interface.

¹² op. cit., H. L. Caswell.

⁴¹ H. K. Birnbaum and M. Levy, *Acta Met.*, 4, 84 (1956).

⁴² A. J. Filmer, G. J. Hutton and I. S. Hutchinson, *J. Appl. Phys.*, 29, 146 (1958).

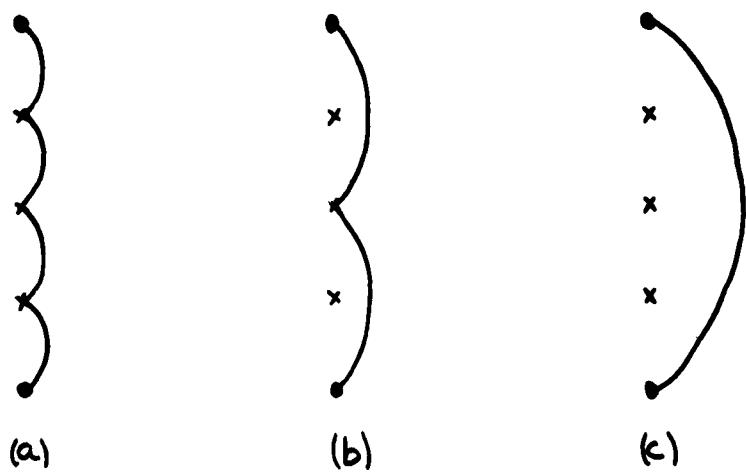


Figure 1

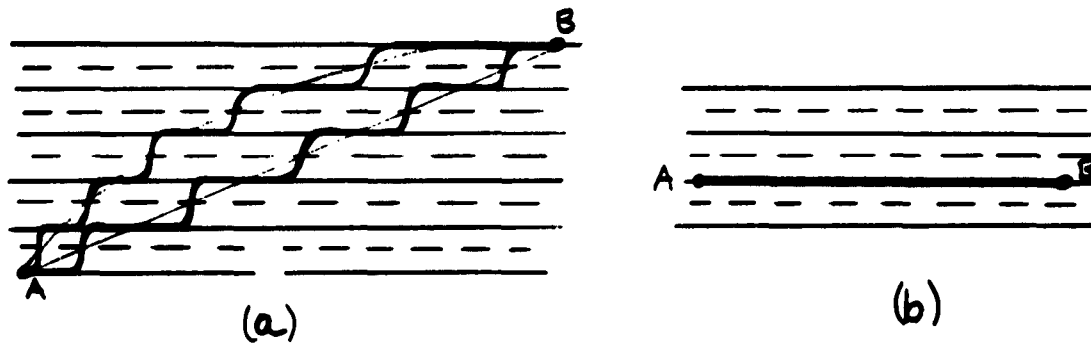


Figure 2

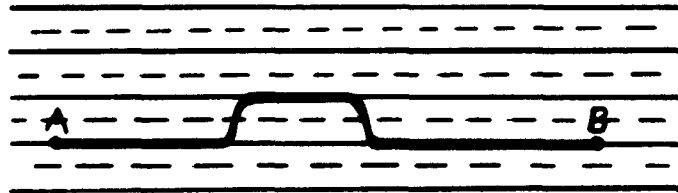


Figure 3

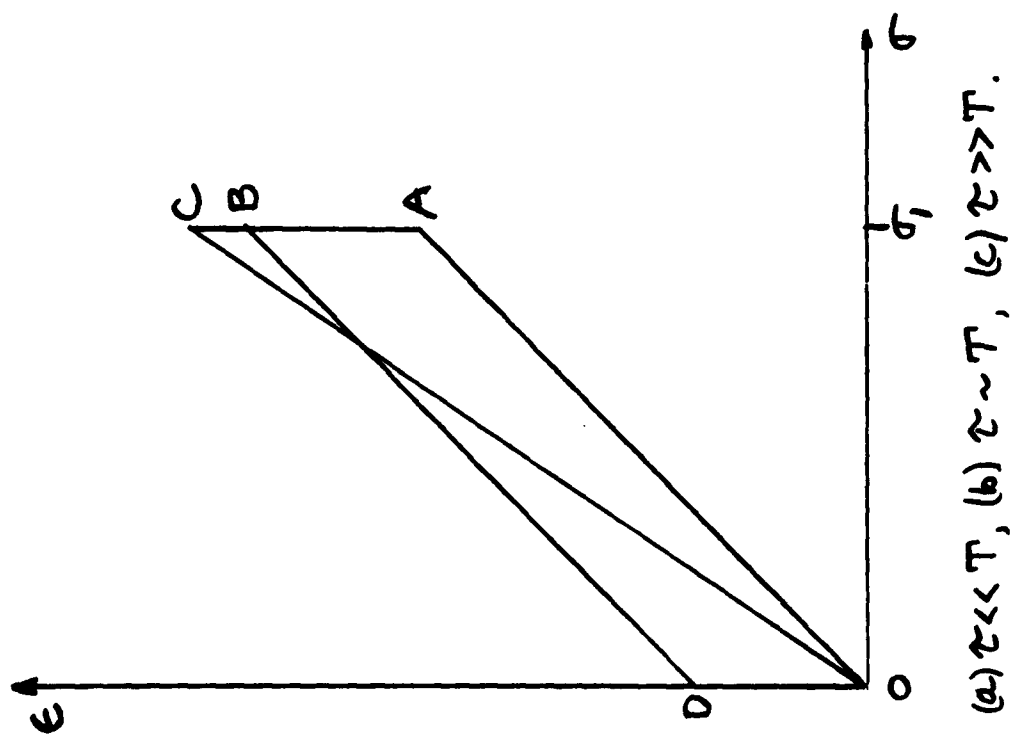


Figure 5

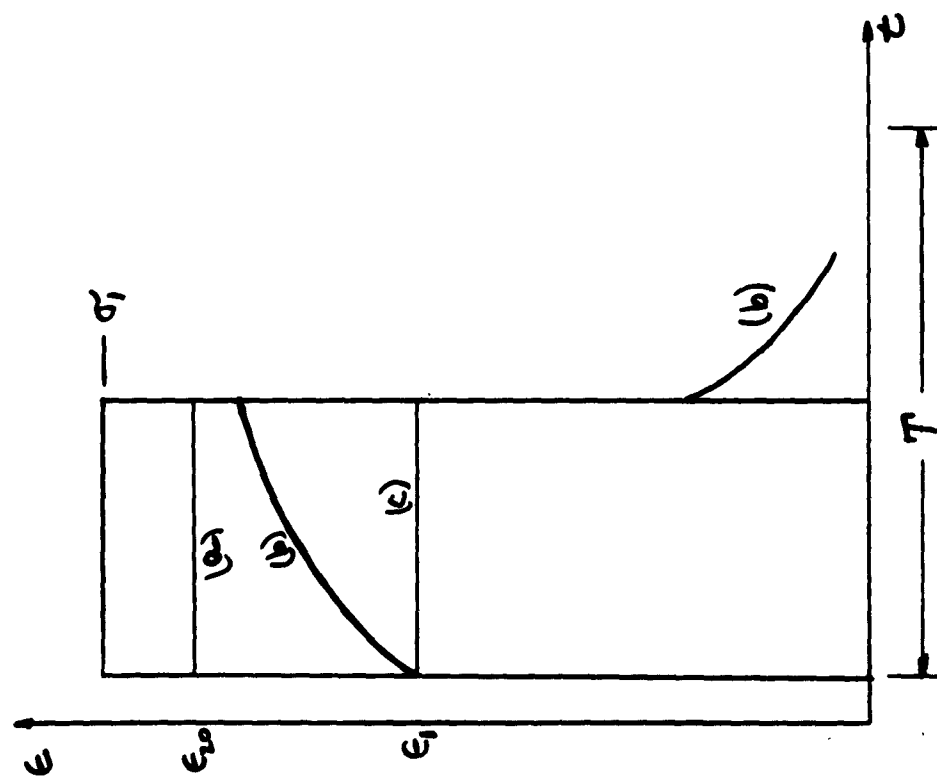


Figure 4

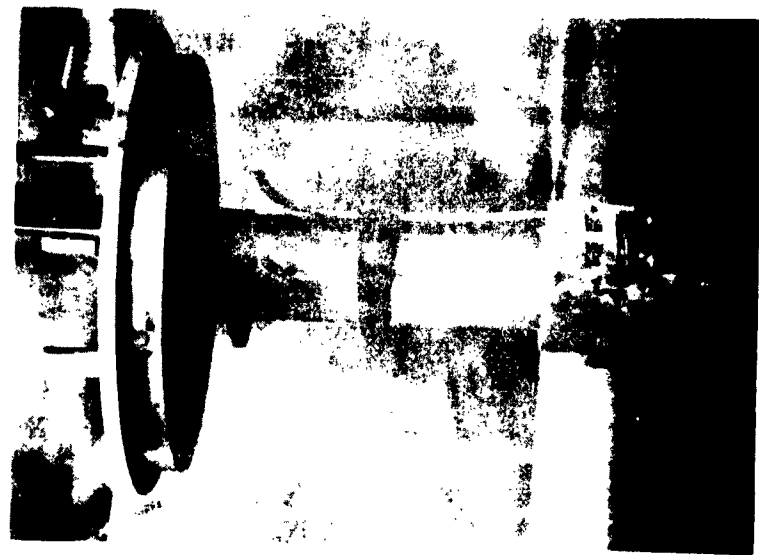


Figure 7



Figure 6



Figure 8



Figure 9

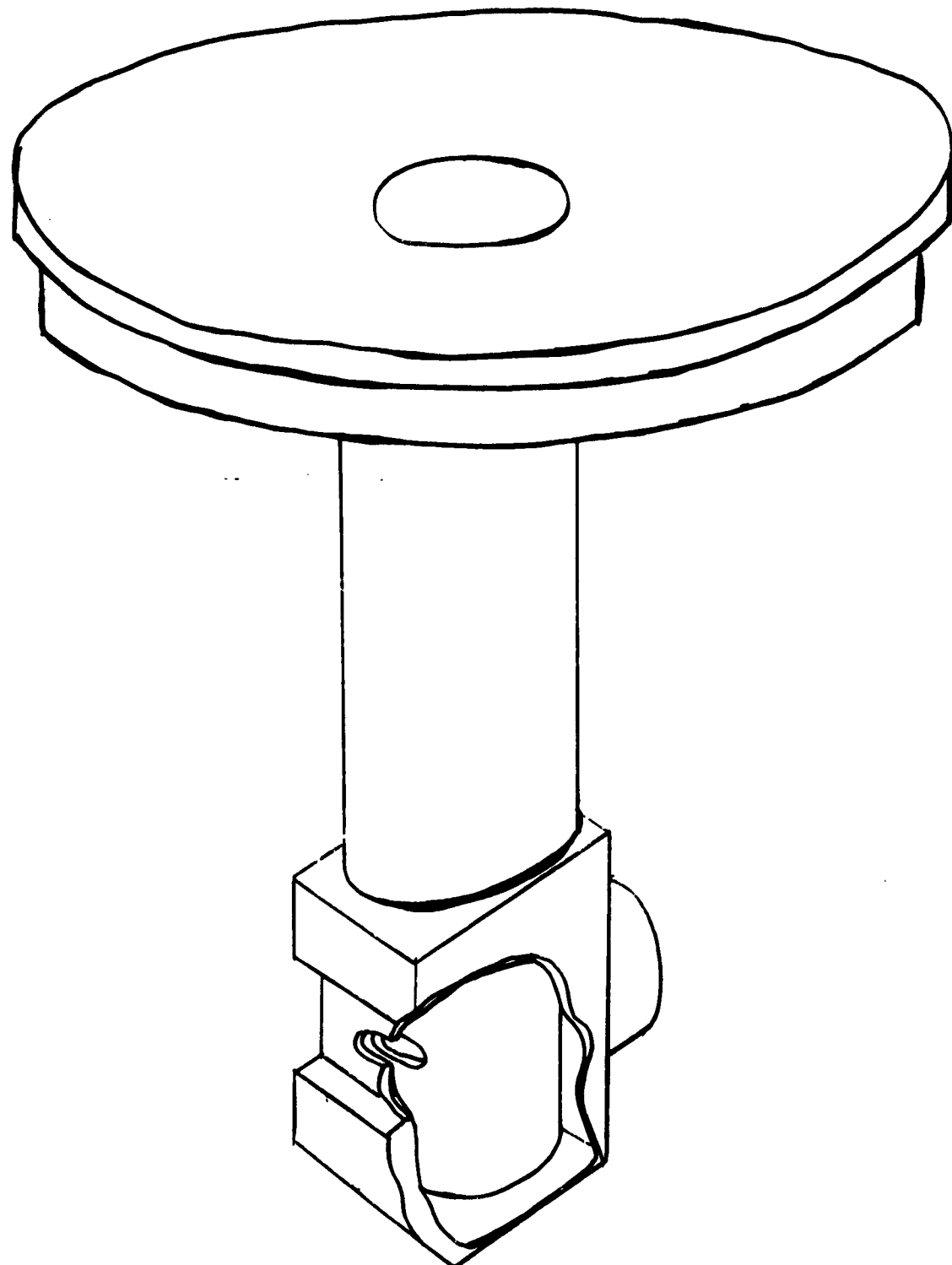


Figure 10

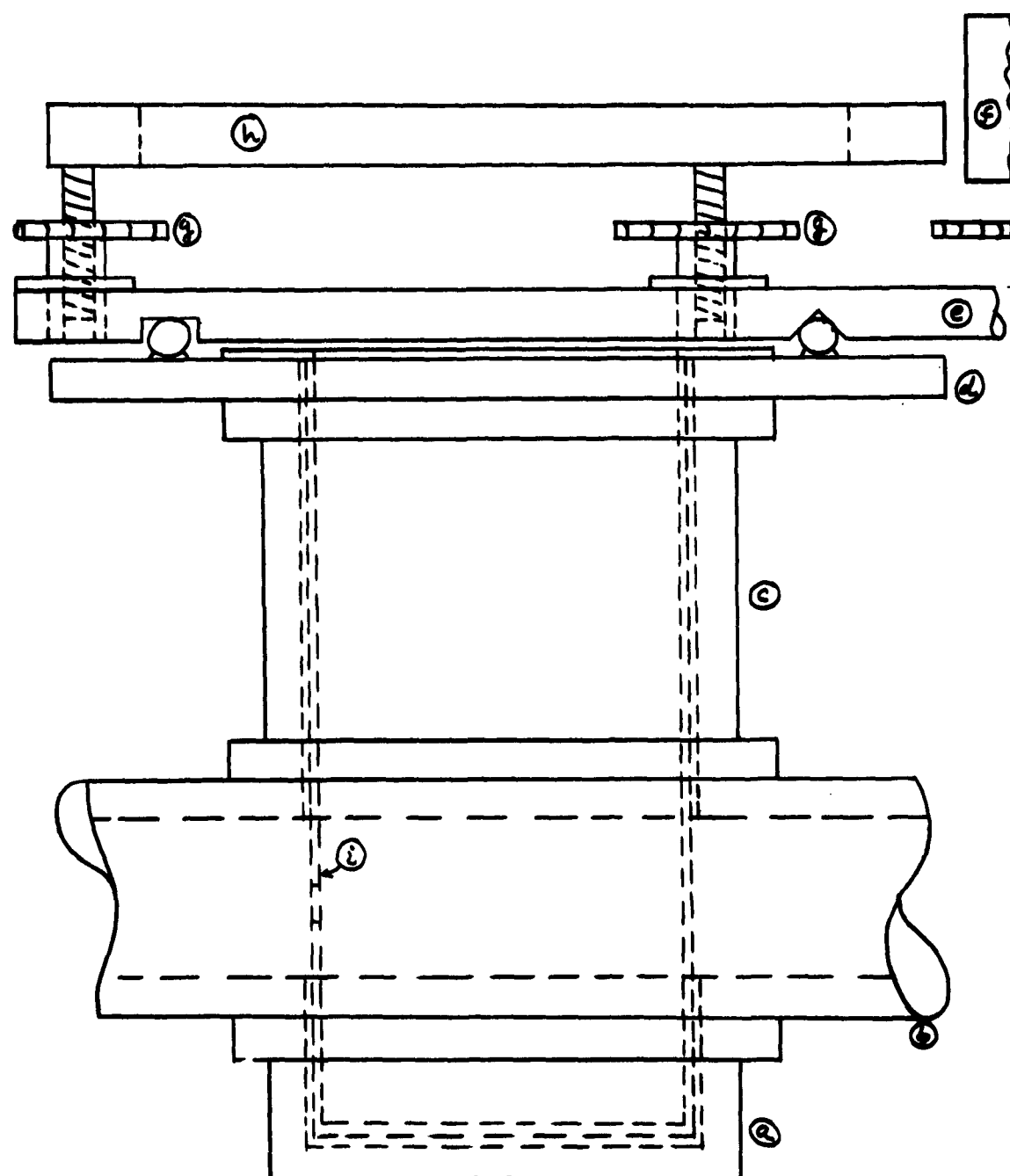


Figure 11

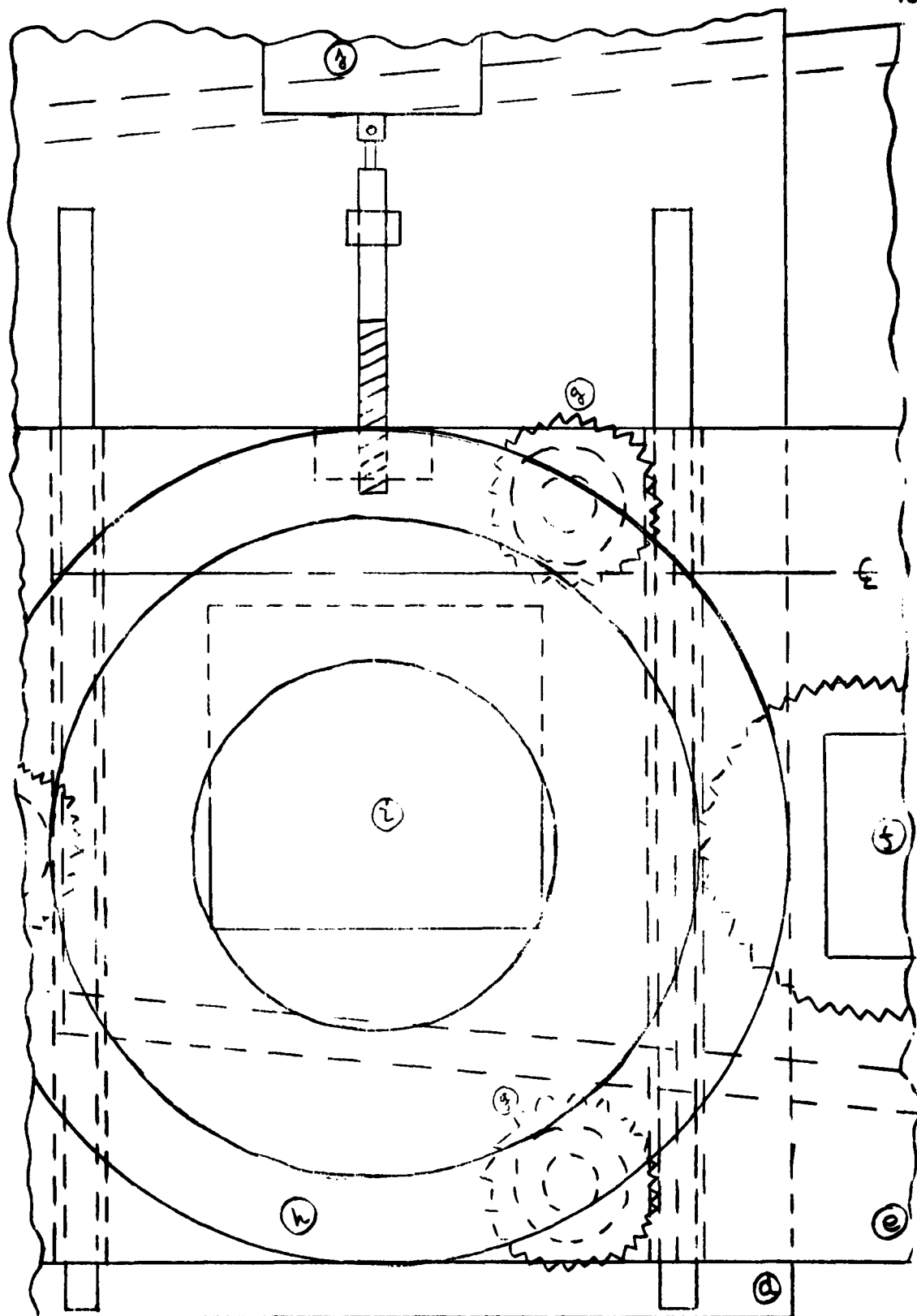


Figure 12

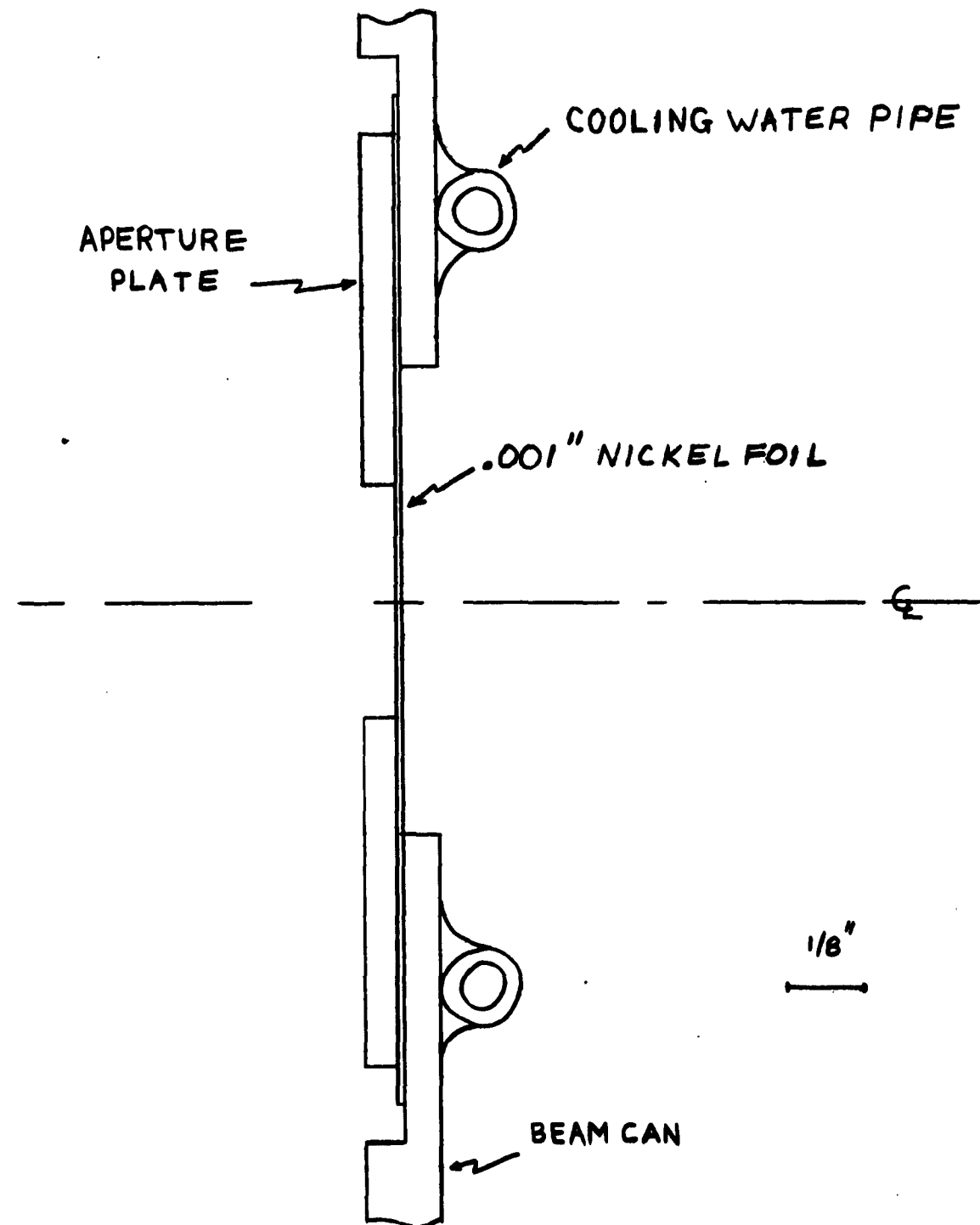
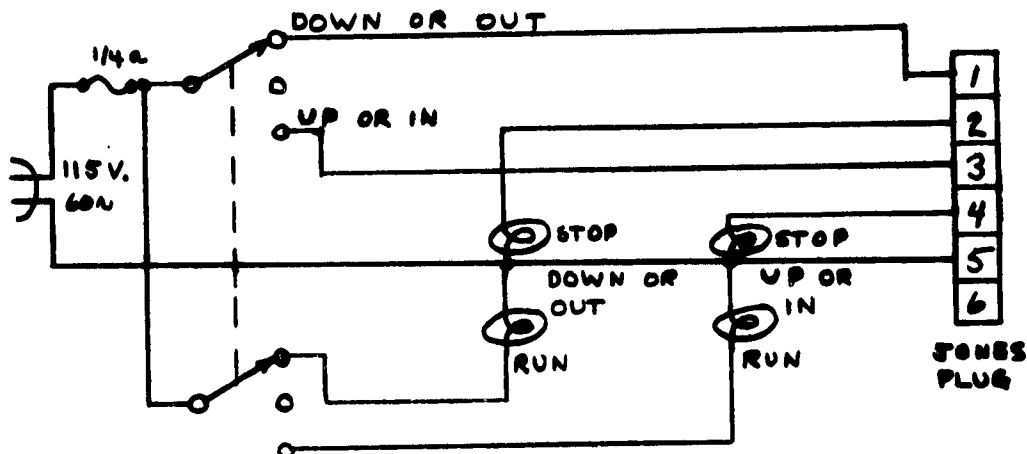
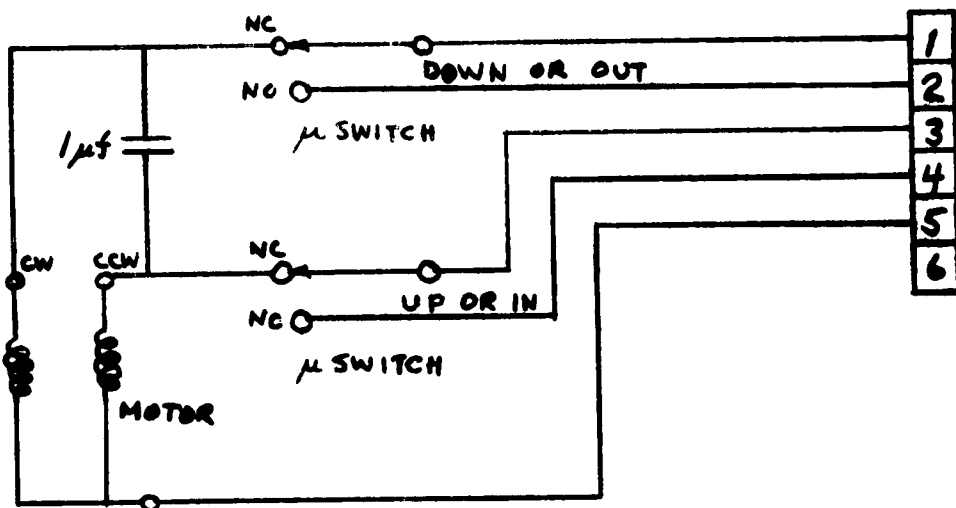


Figure 13

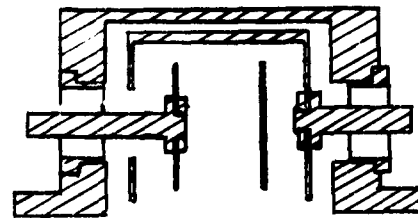


CONTROL PANEL



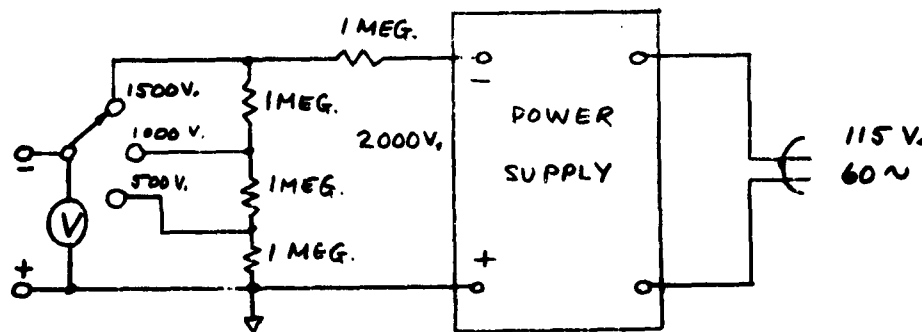
MOTOR SITE

Figure 14



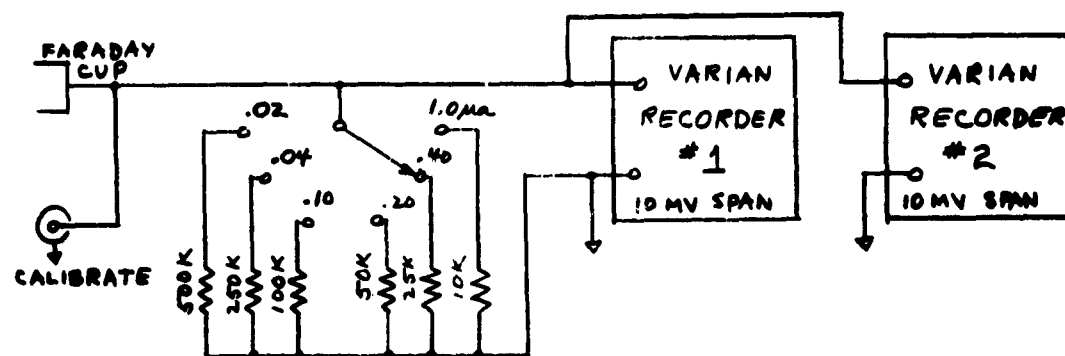
FARADAY CUP CHAMBER

Figure 15



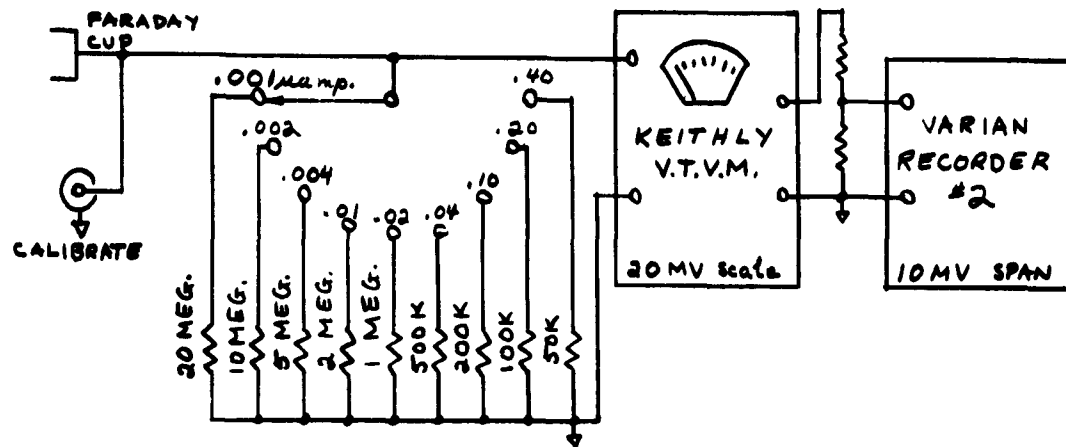
FARADAY CUP SUPPRESSOR POWER SUPPLY

Figure 16



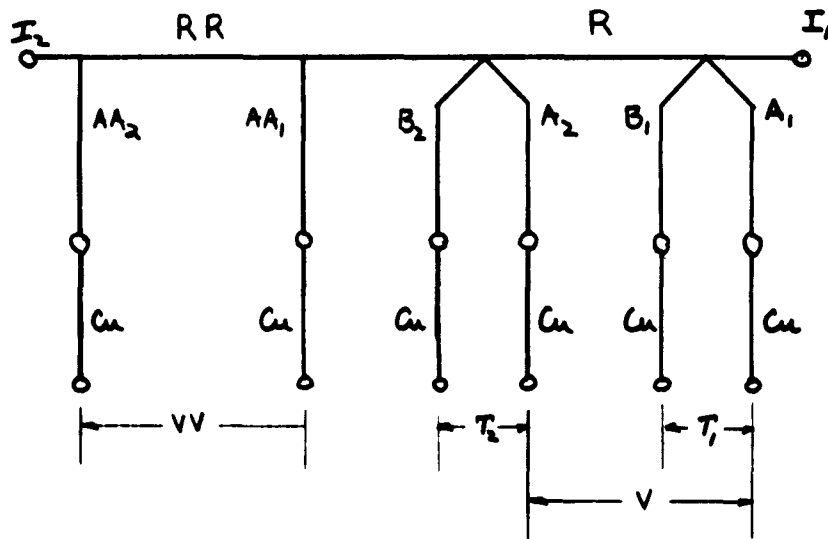
BEAM CURRENT MEASUREMENT #1

Figure 17



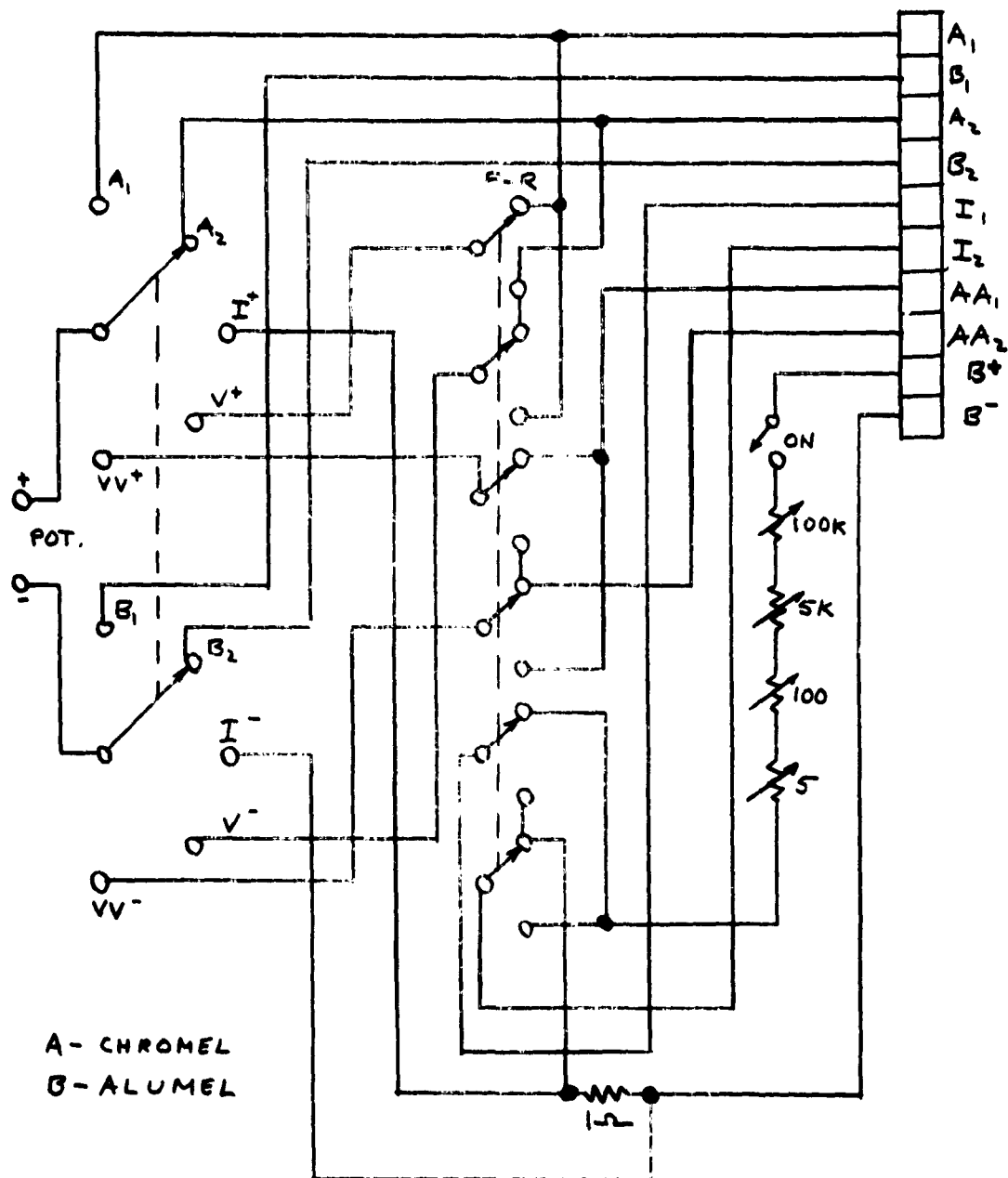
BEAM CURRENT MEASUREMENT #2

Figure 18



ELECTRICAL RESISTANCE MEASUREMENT

Figure 19



SWITCHING CIRCUIT FOR
ELECTRICAL RESISTANCE MEASUREMENT

Figure 20

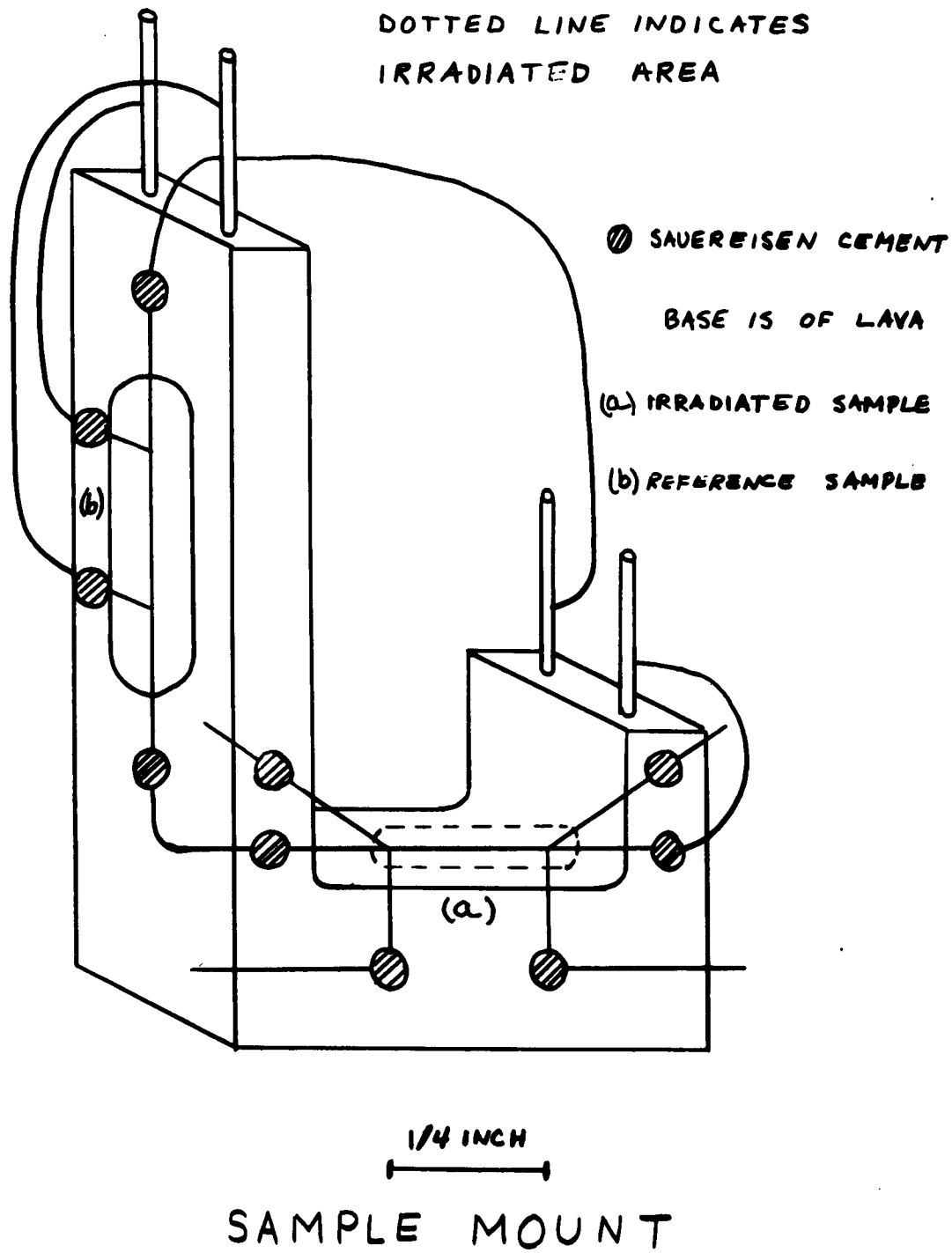
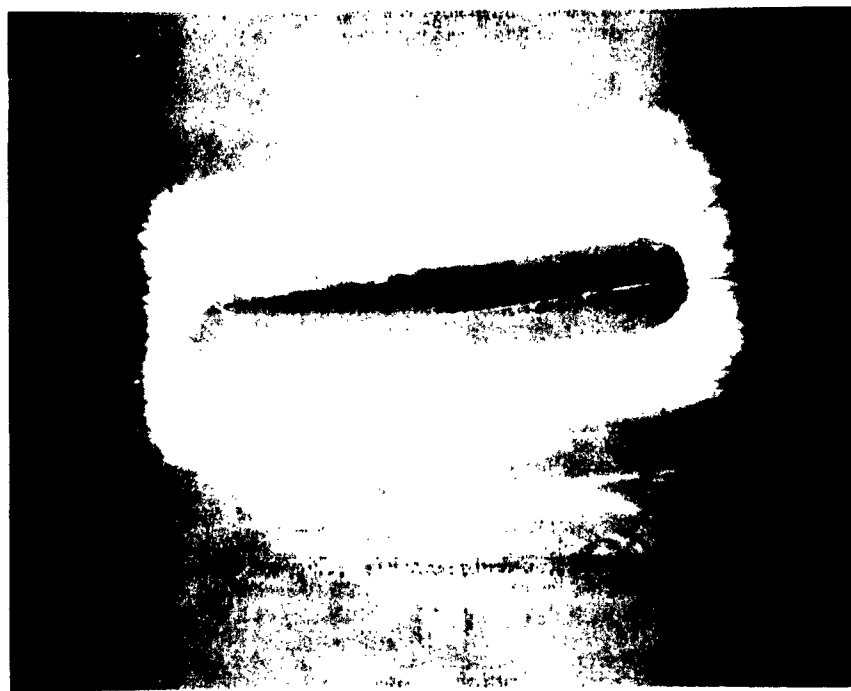
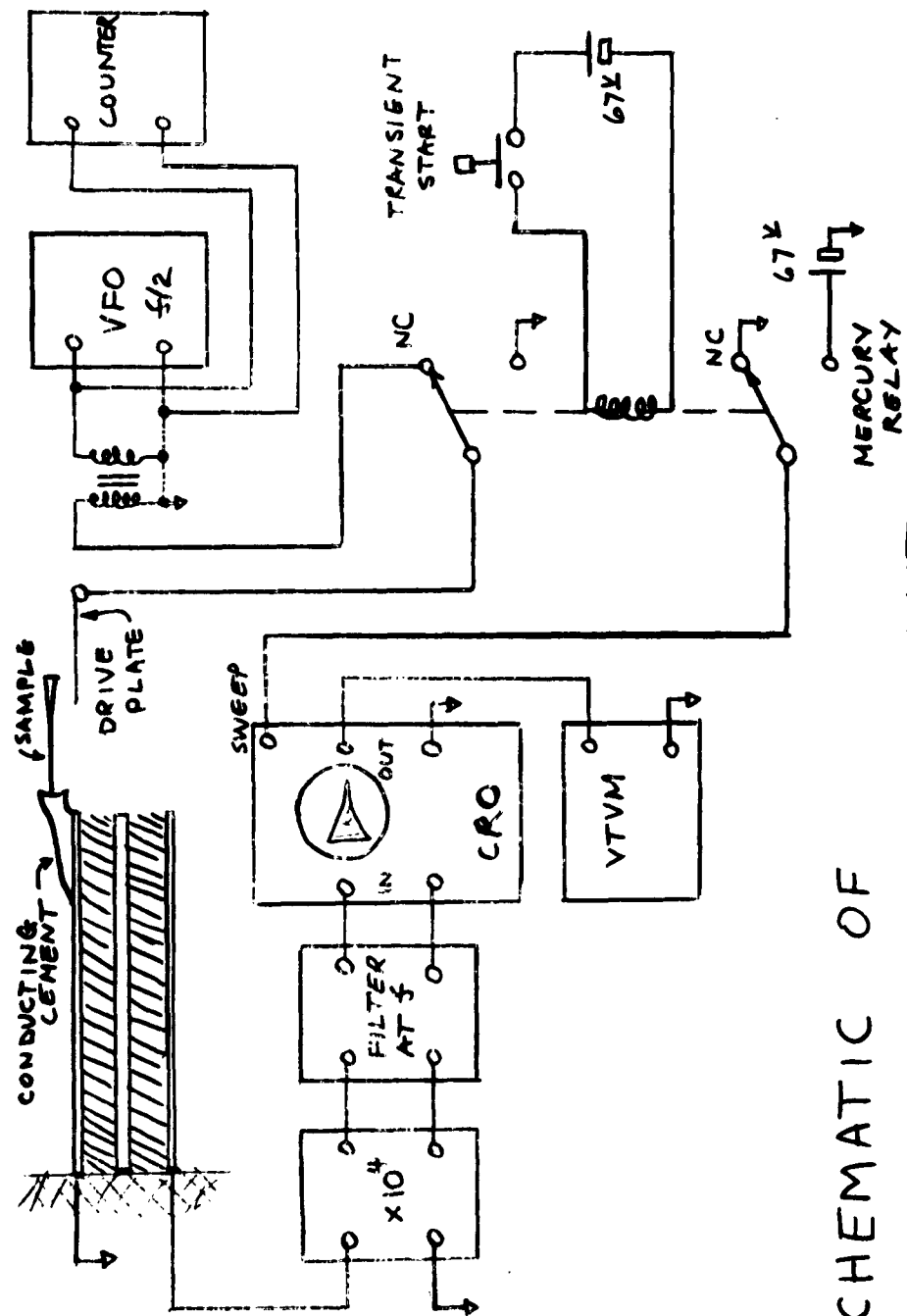


Figure 21





SCHEMATIC OF MECHANICAL MEASUREMENT

Figure 23

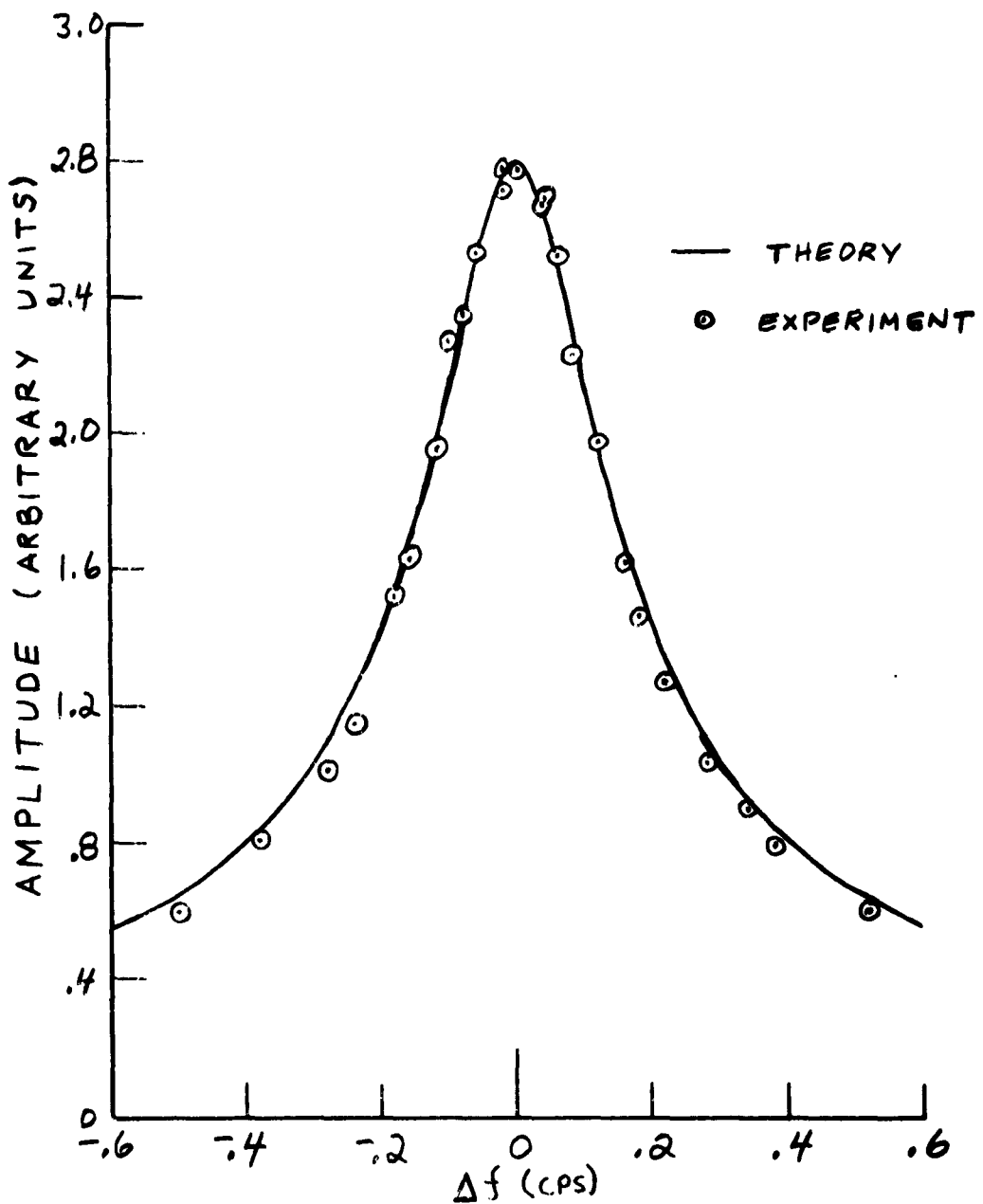
MECHANICAL RESONANCE OF
A CANTILEVERED ROD

Figure 24

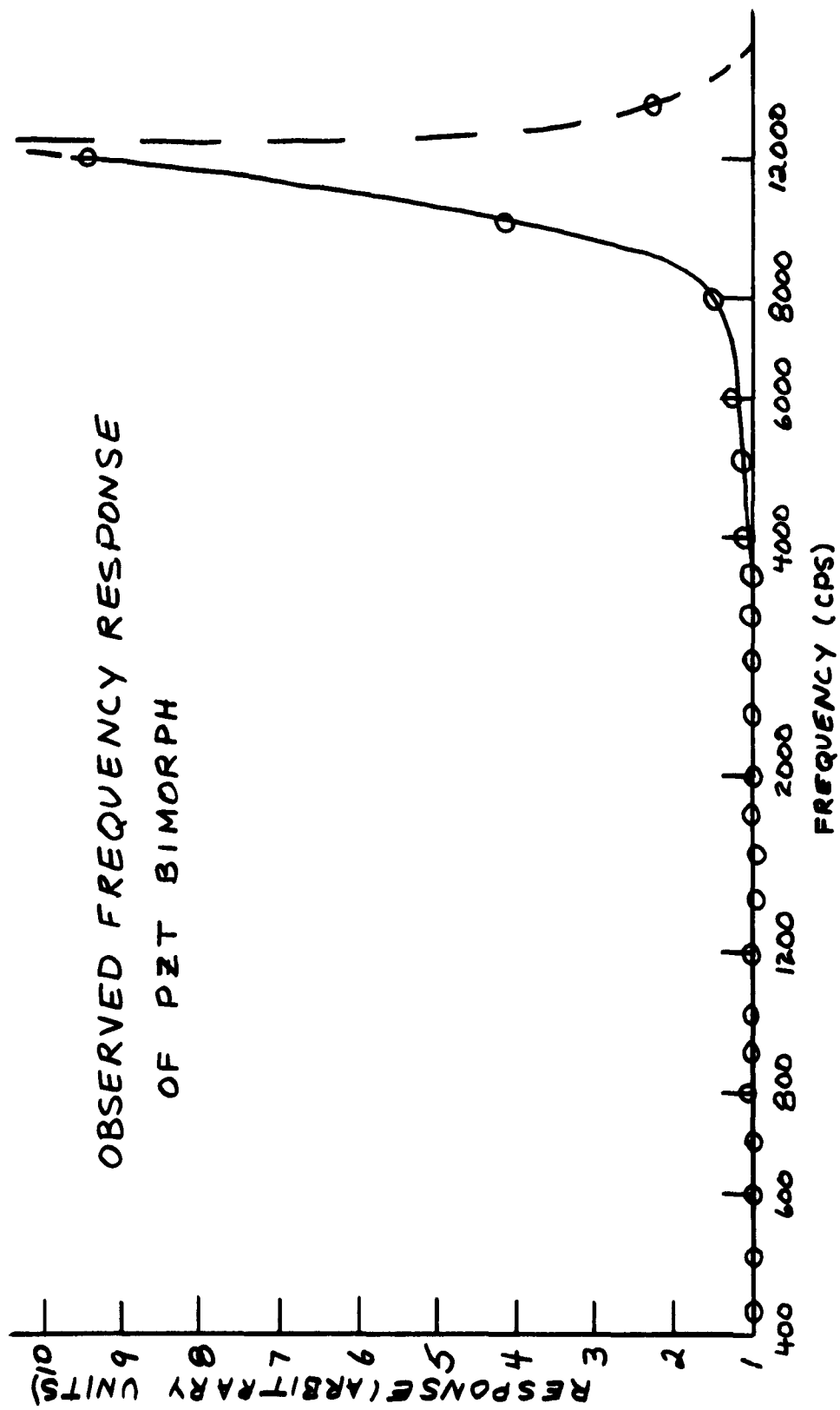


Figure 25

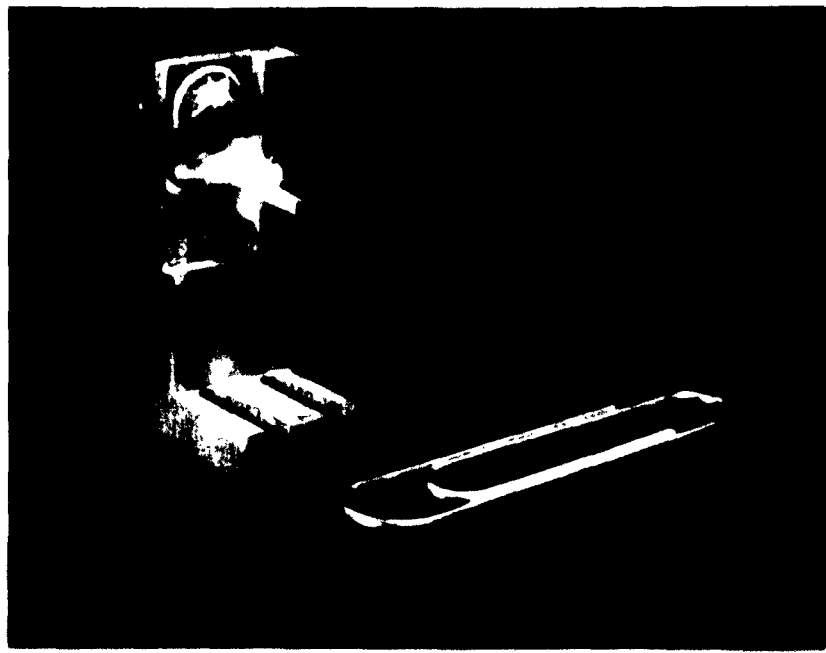
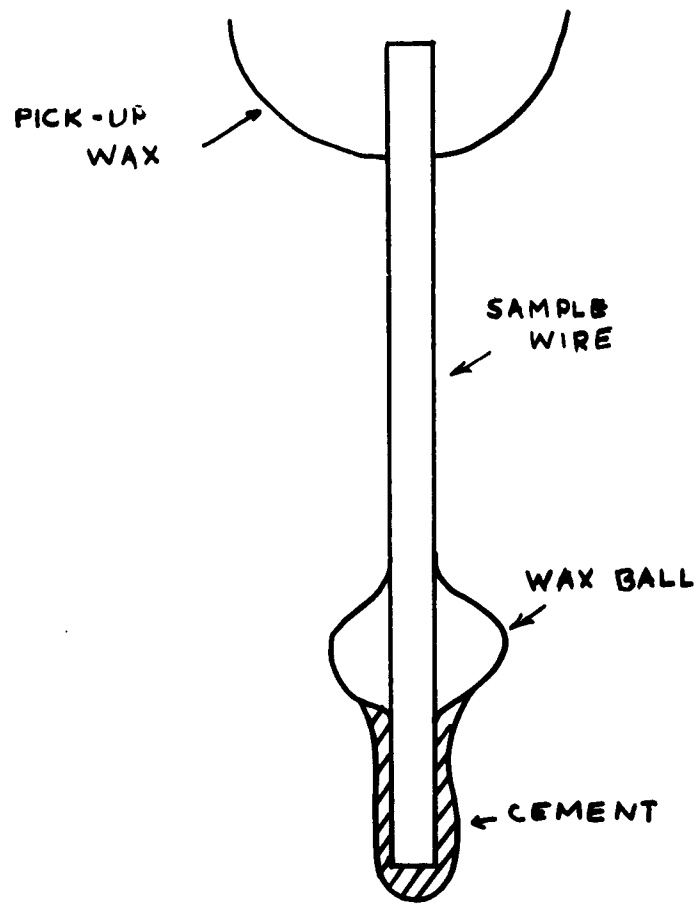


Figure 26



TECHNIQUE FOR APPLYING
CEMENT TO SAMPLE WIRE

Figure 27

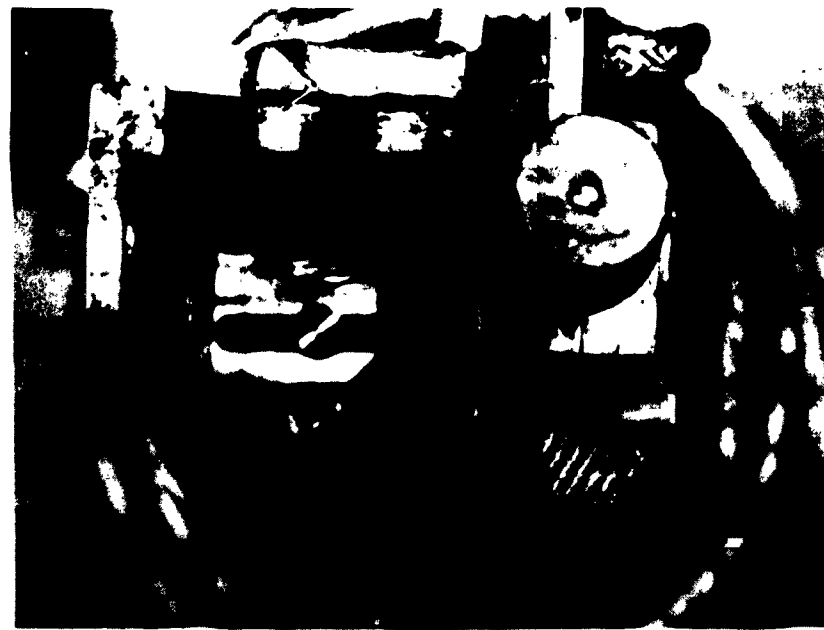
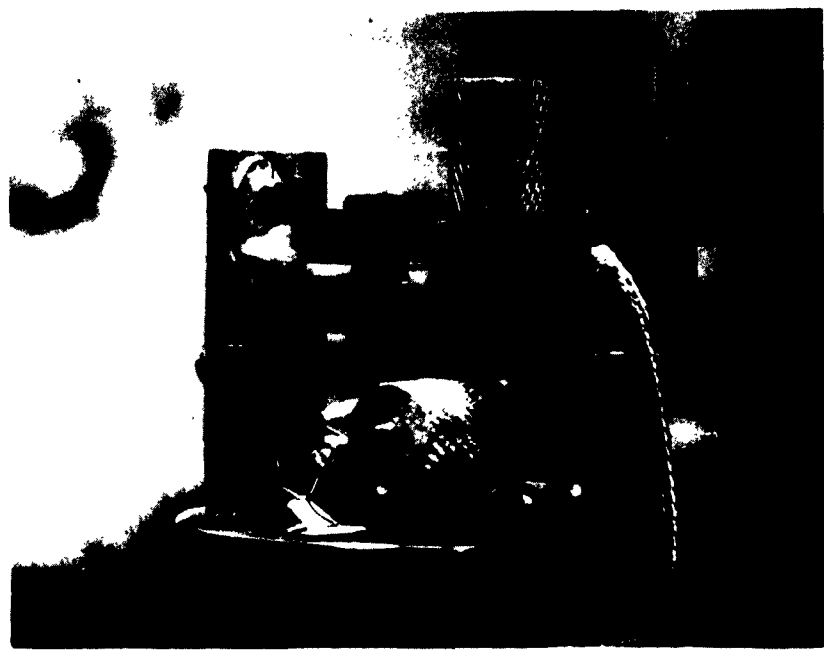


Figure 28

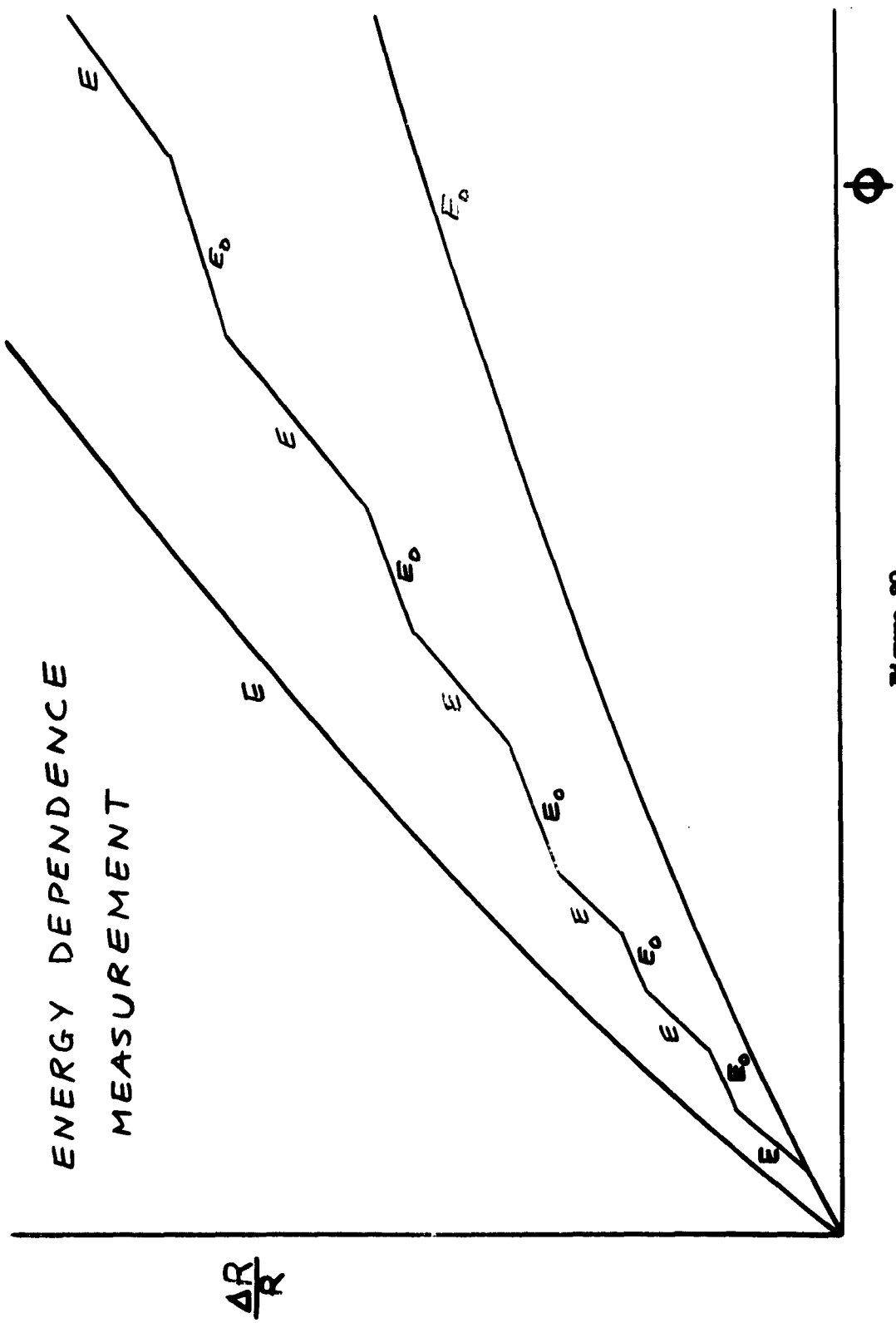


Figure 29

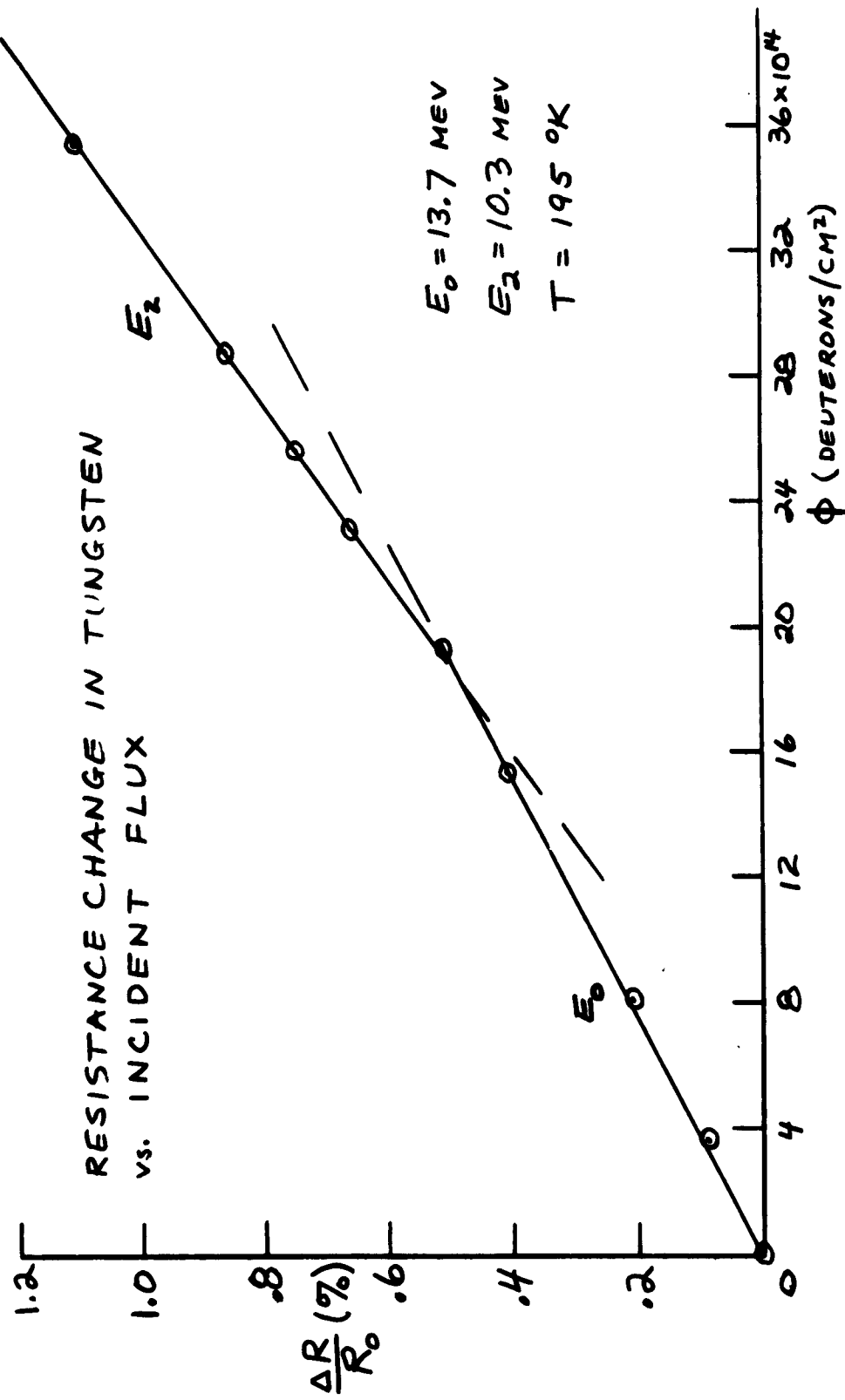


Figure 30

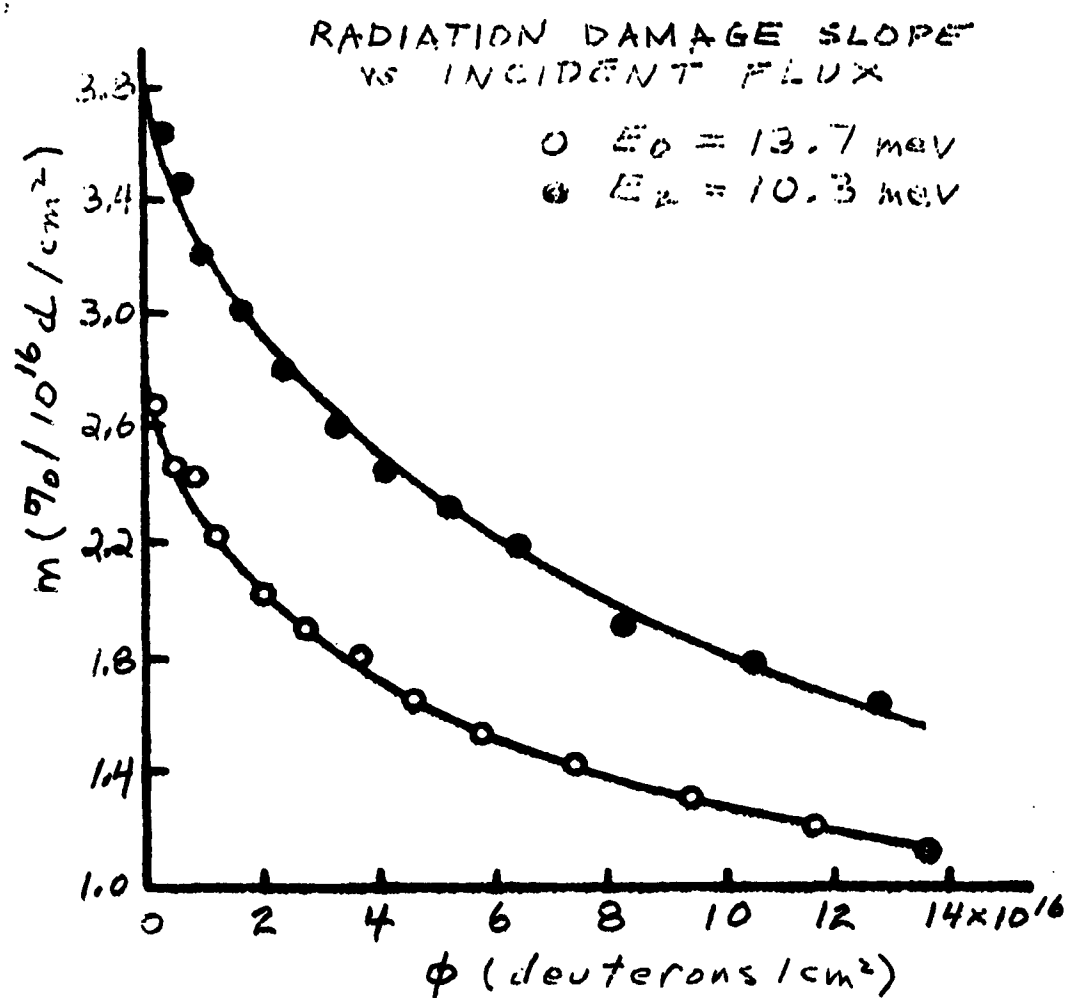


Figure 31

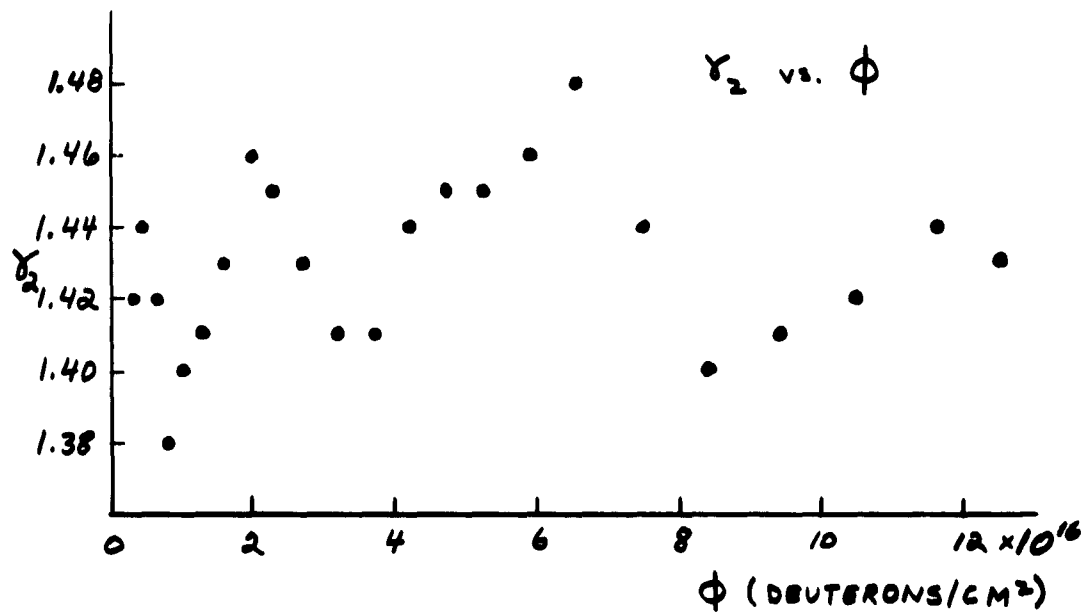


Figure 32

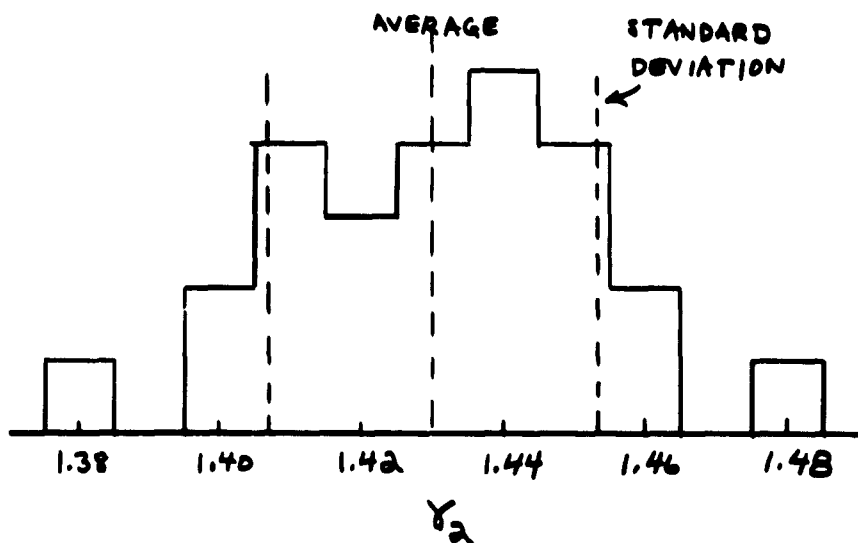


Figure 33

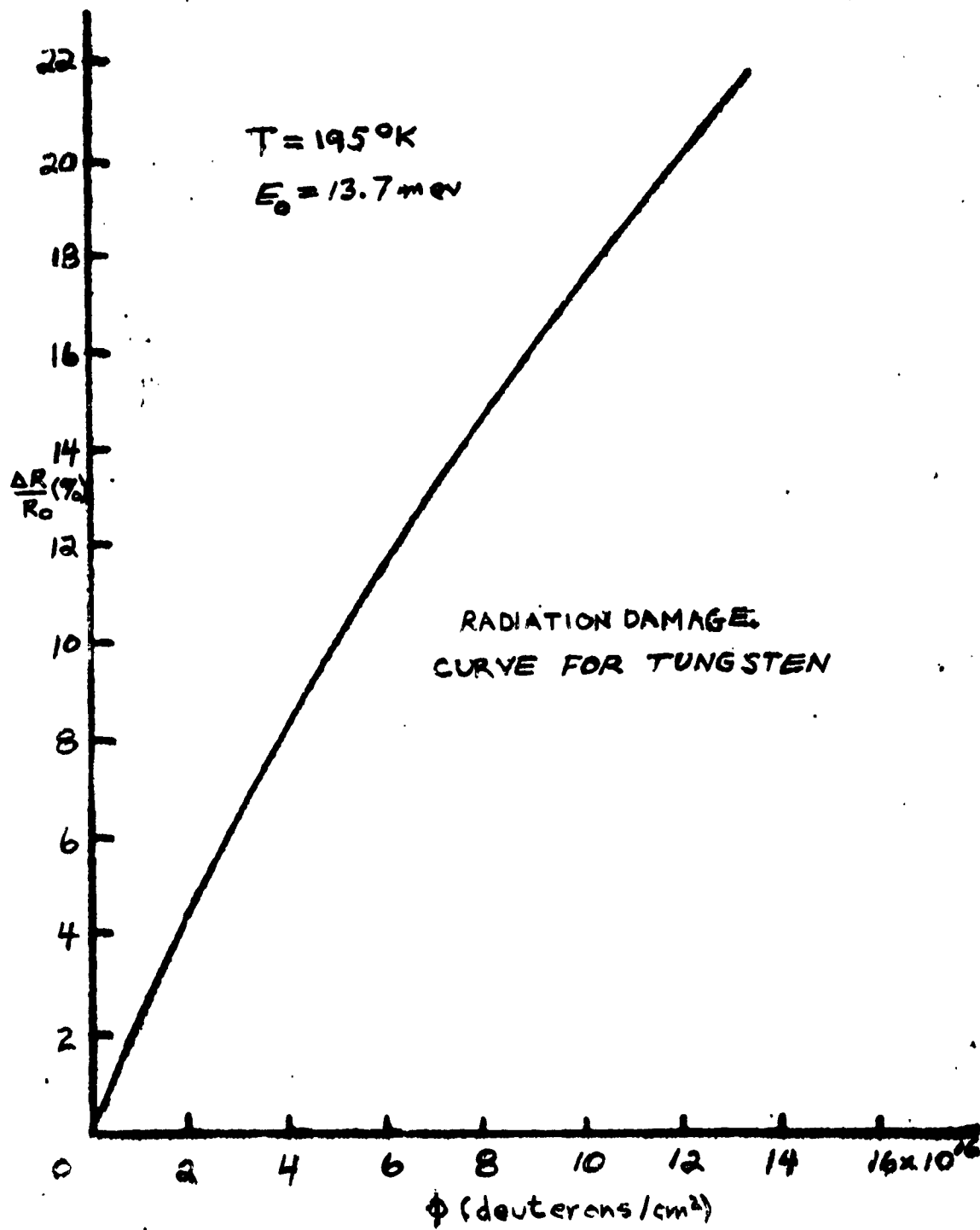


Figure 34

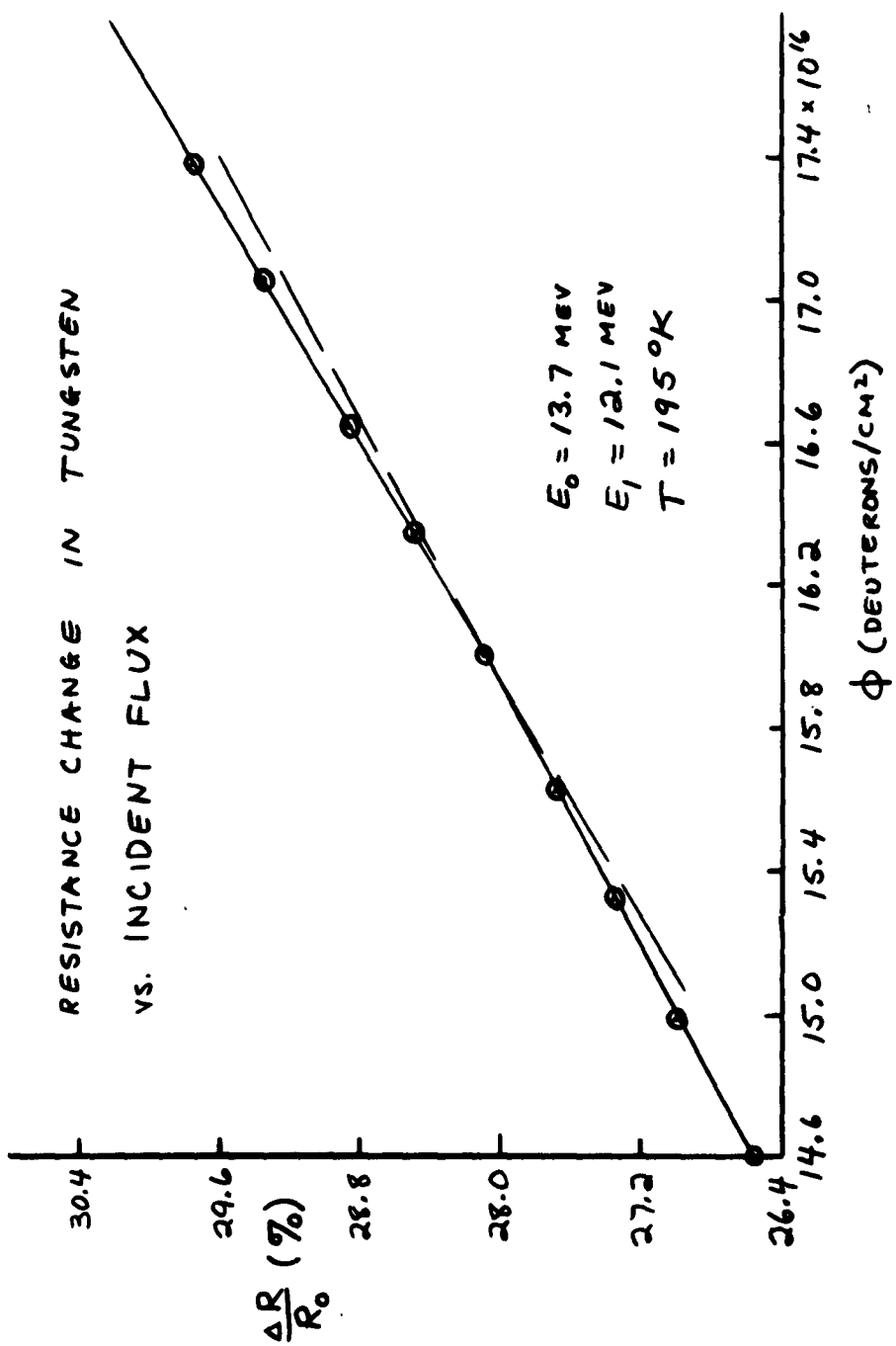


Figure 35

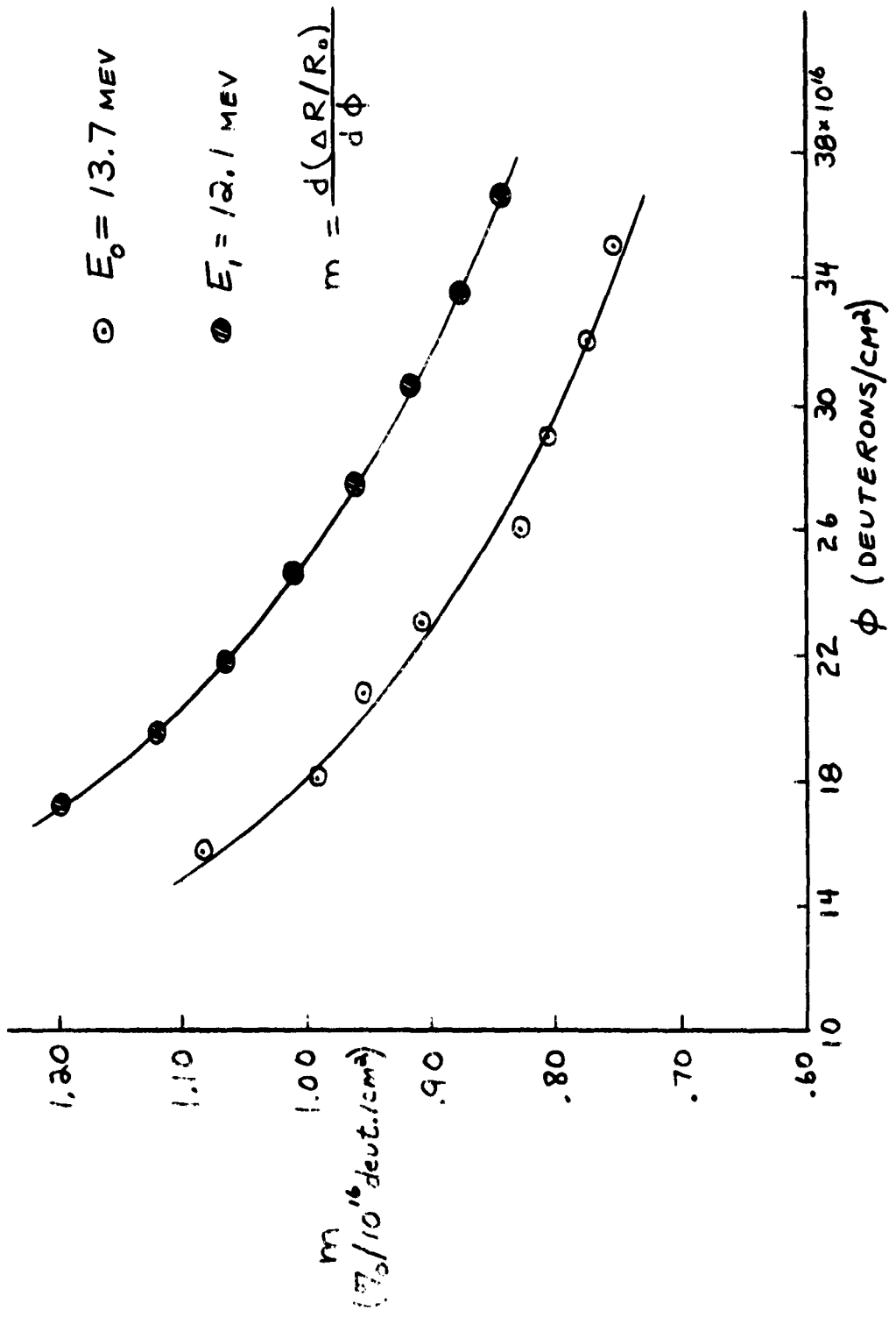


Figure 36

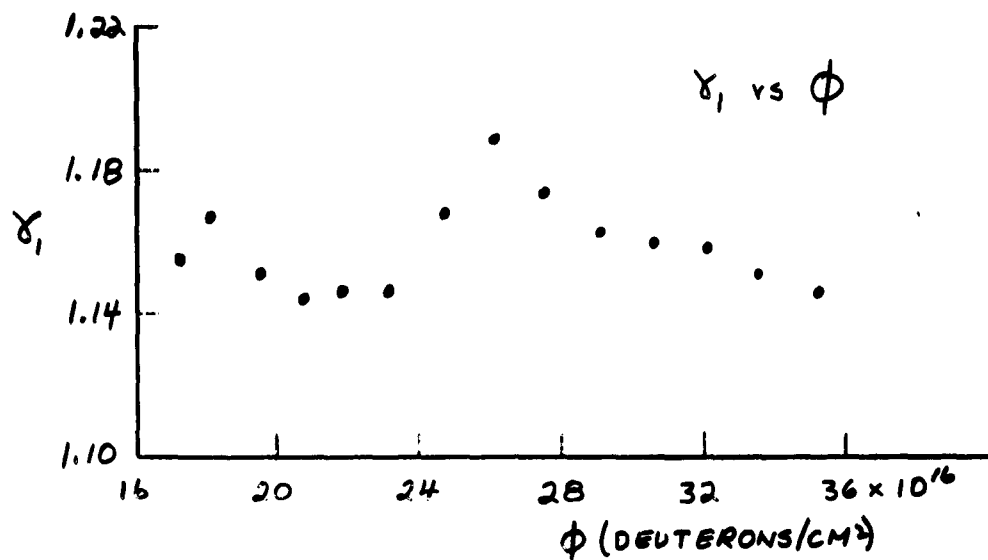


Figure 37

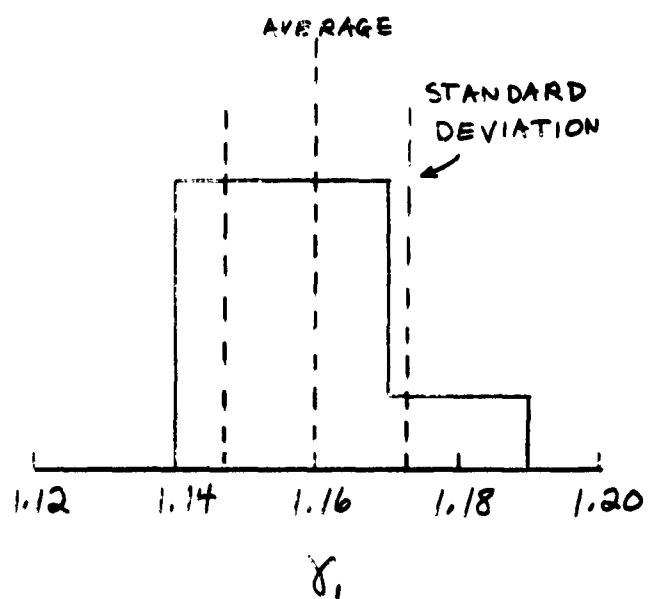
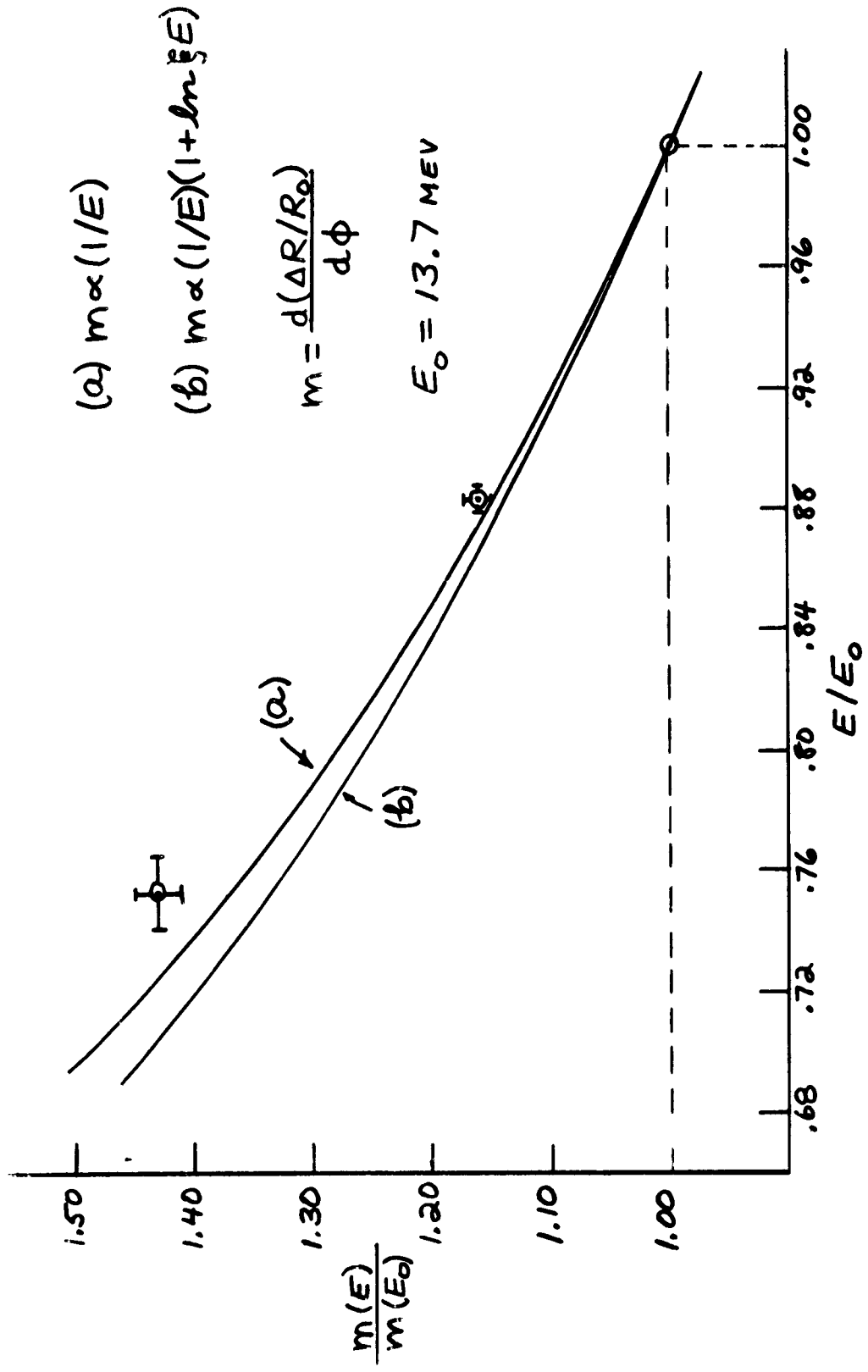


Figure 38



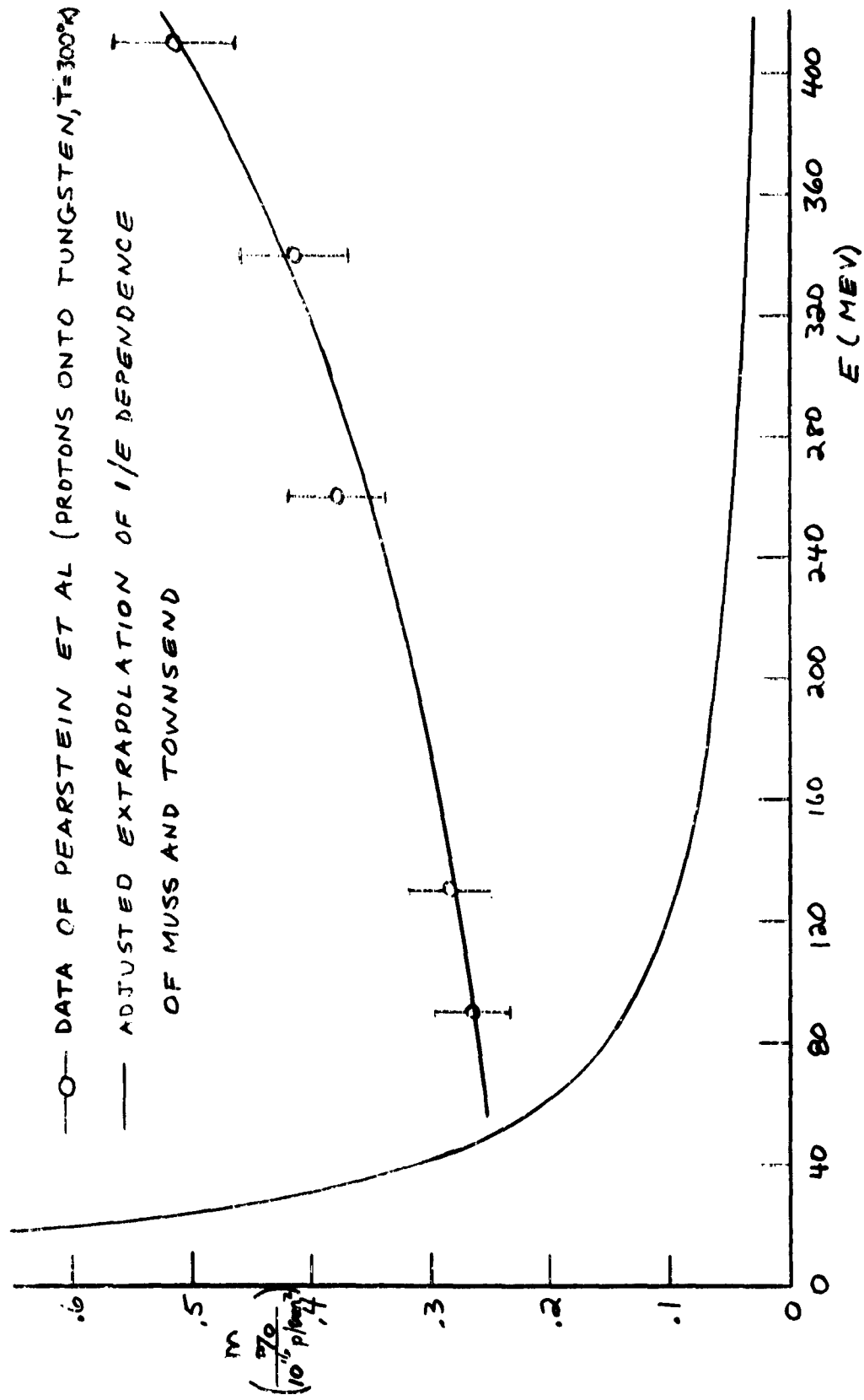


Figure 40

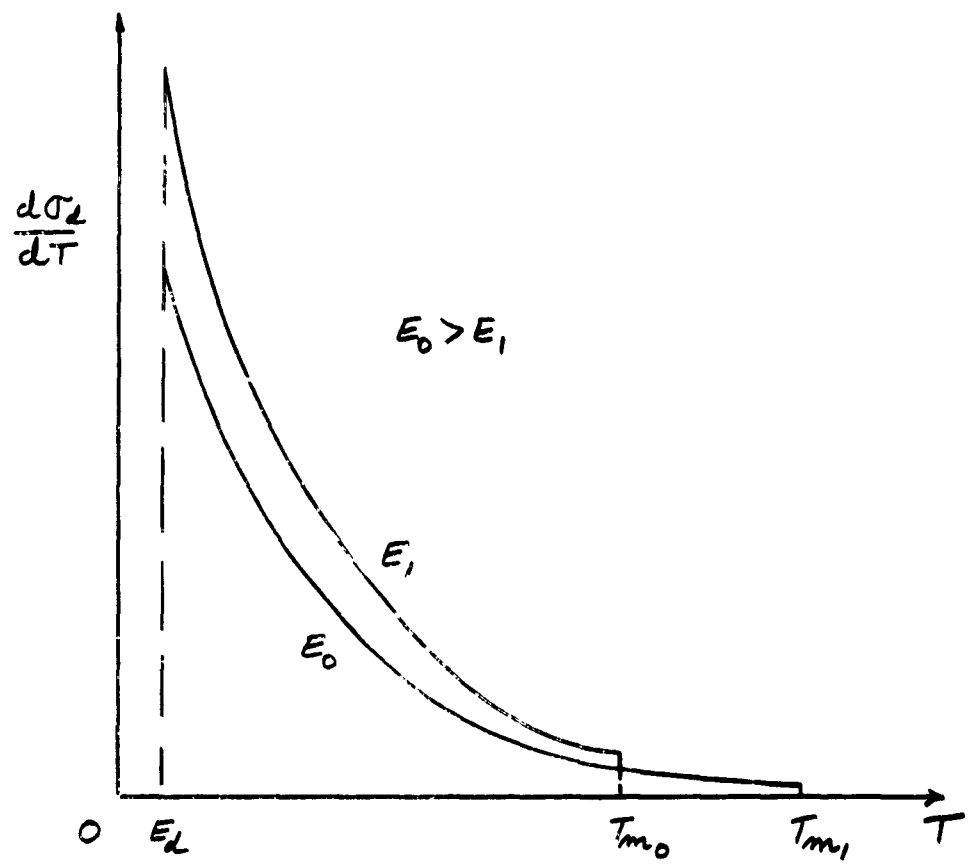
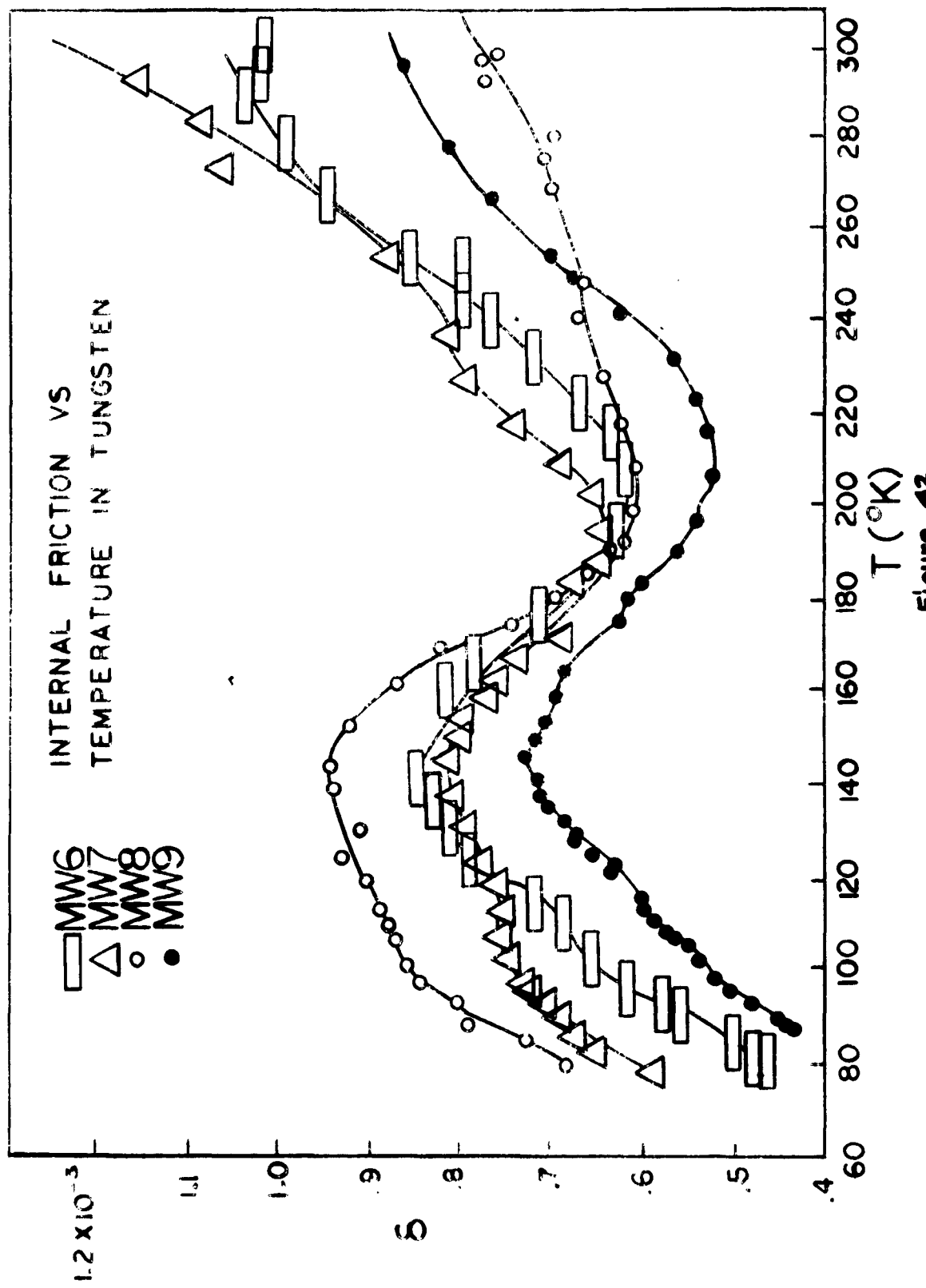


Figure 41



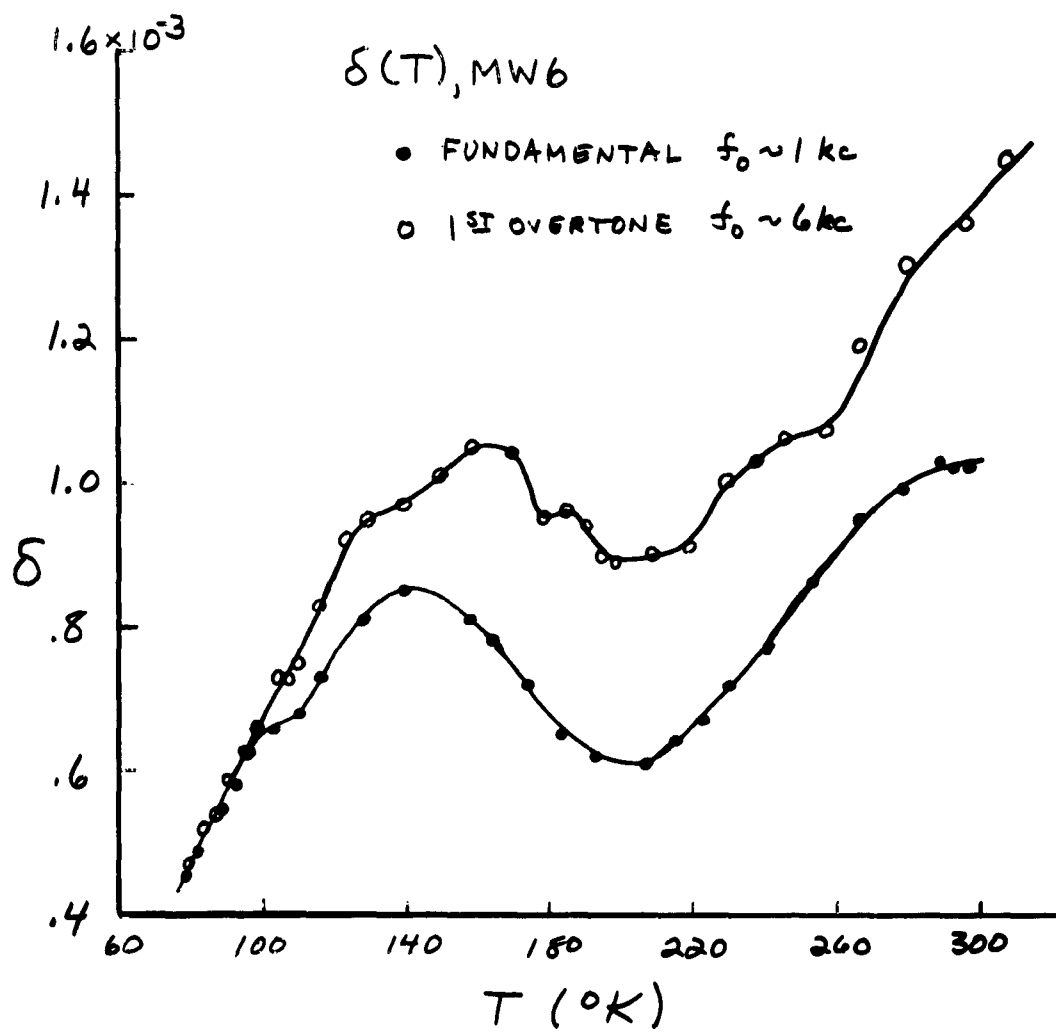
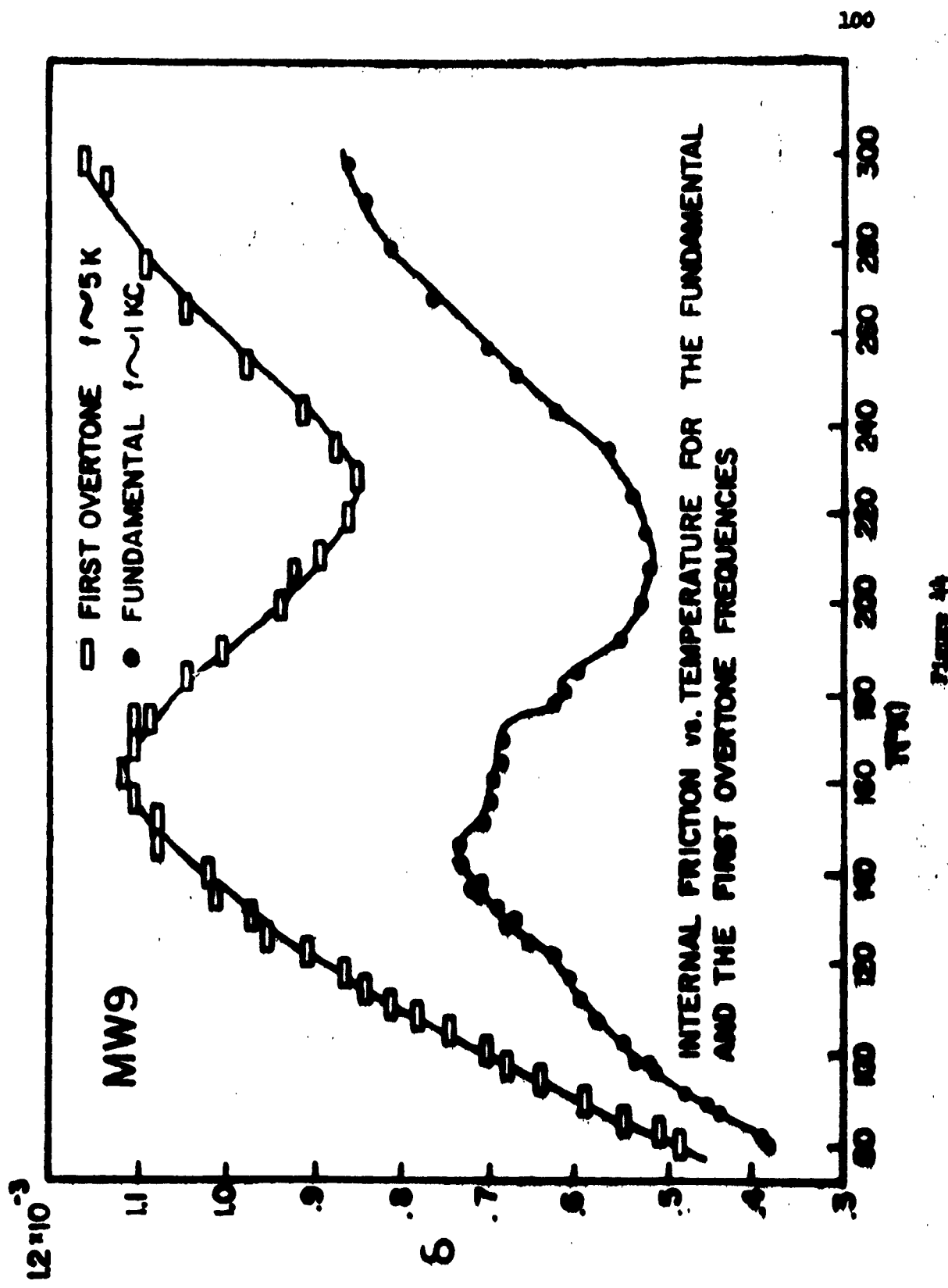


Figure 43



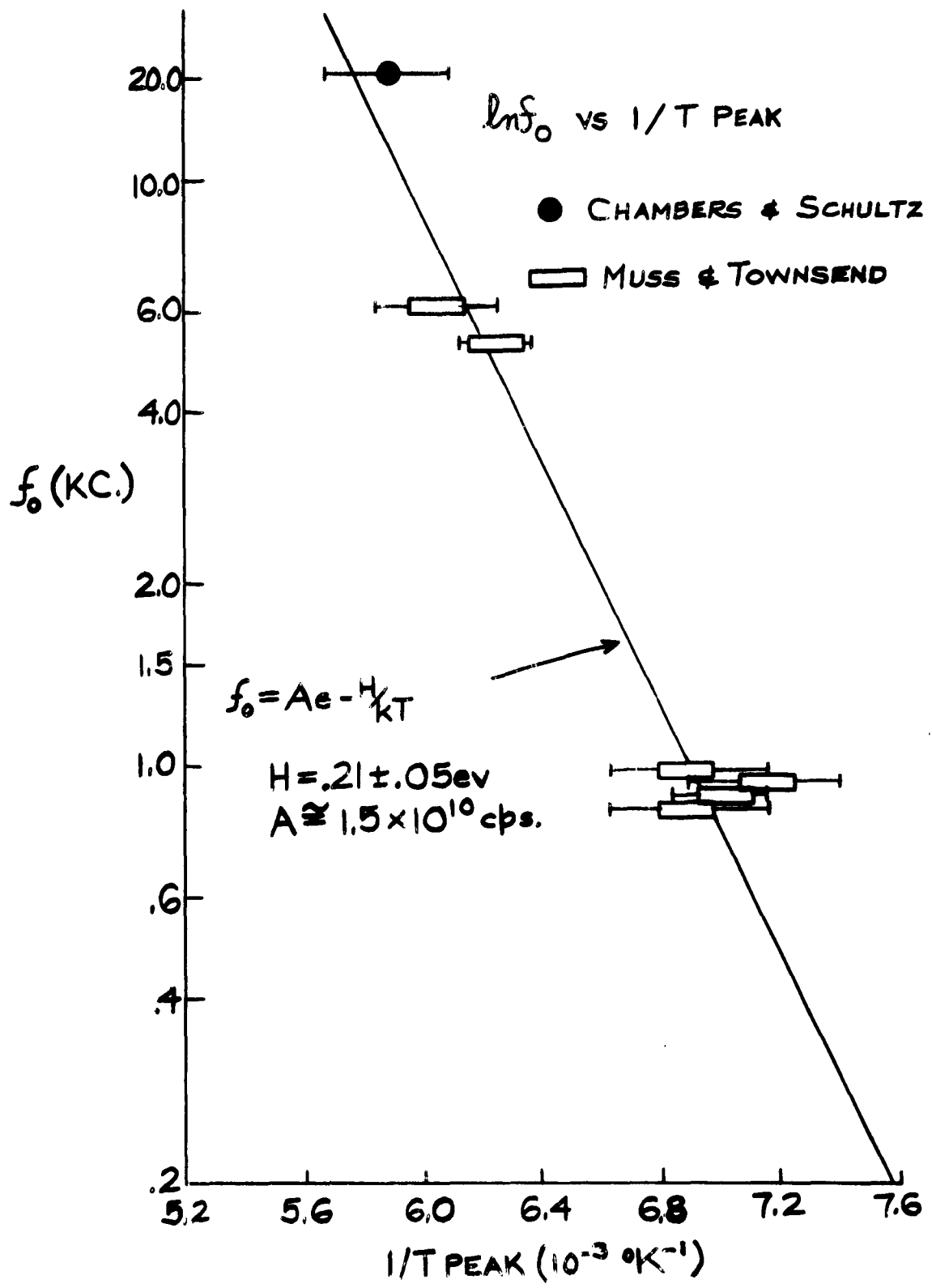


Figure 45

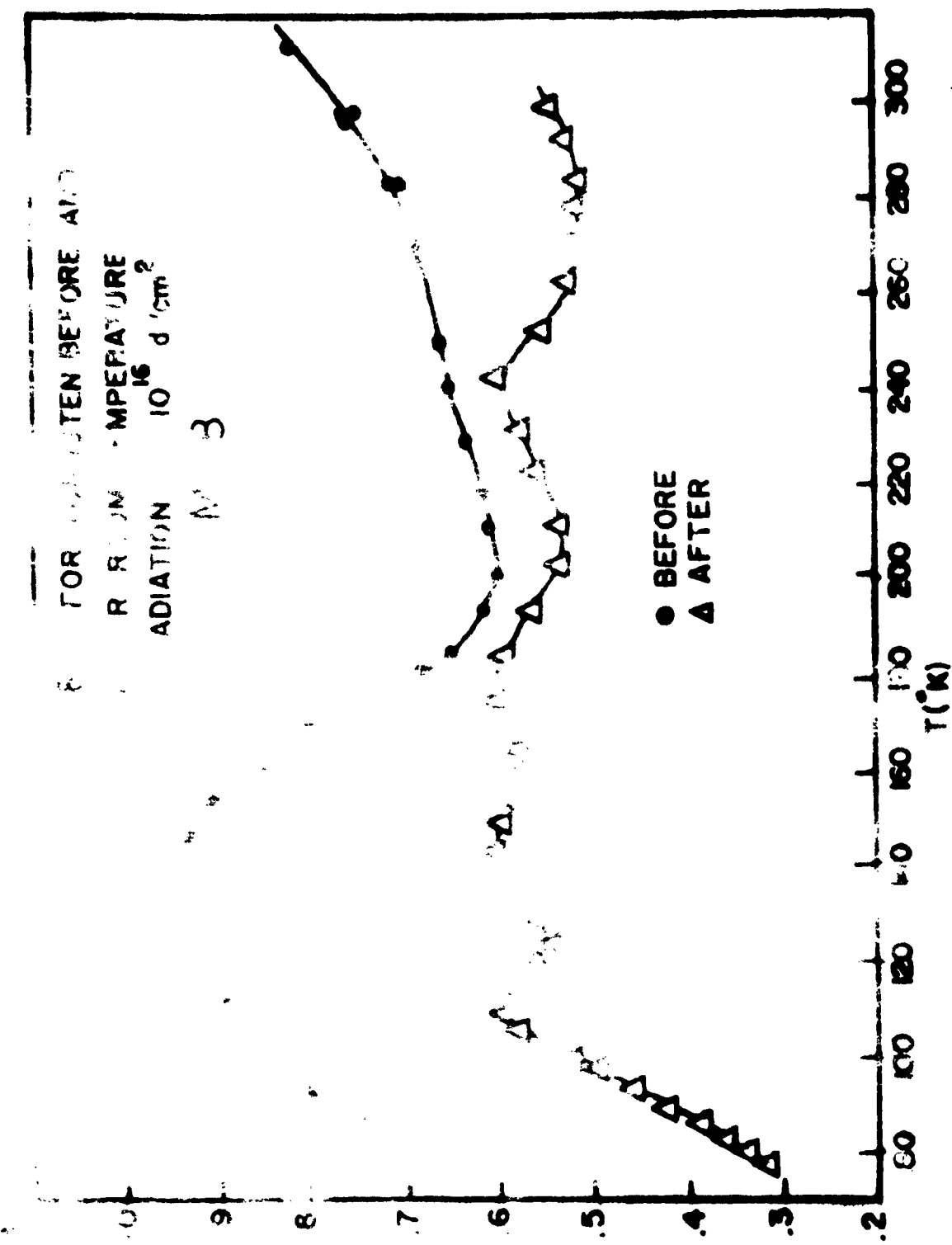
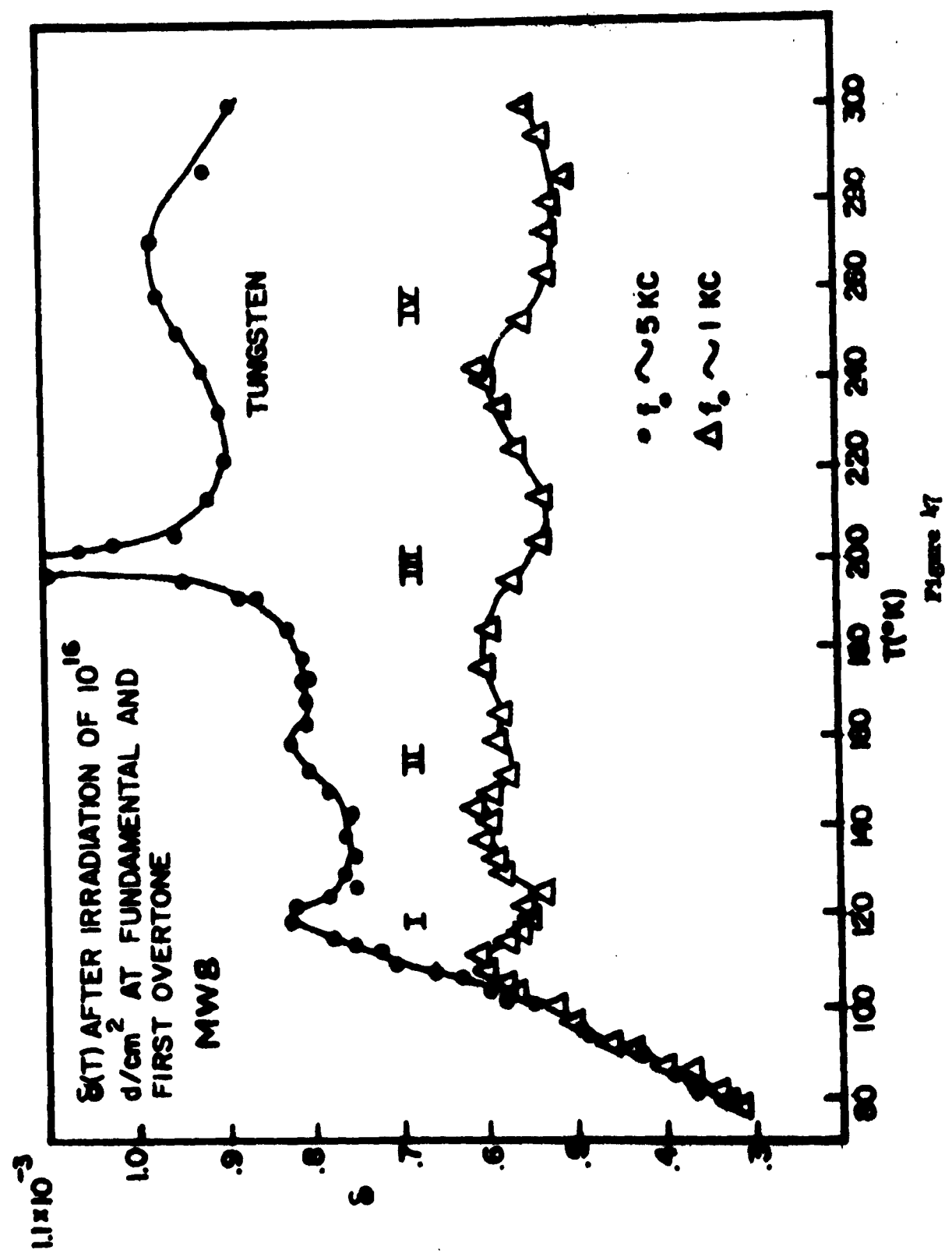
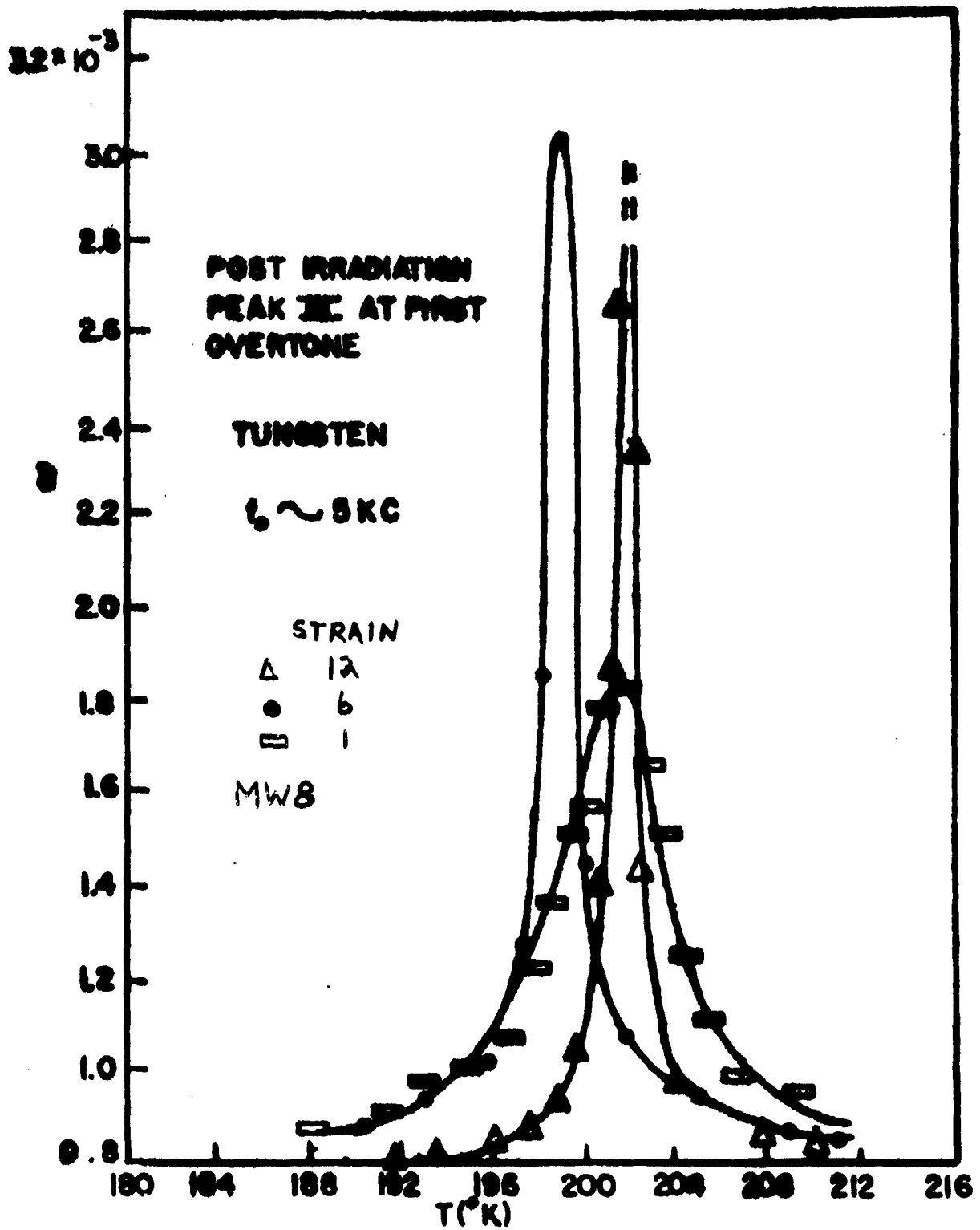


Figure 46





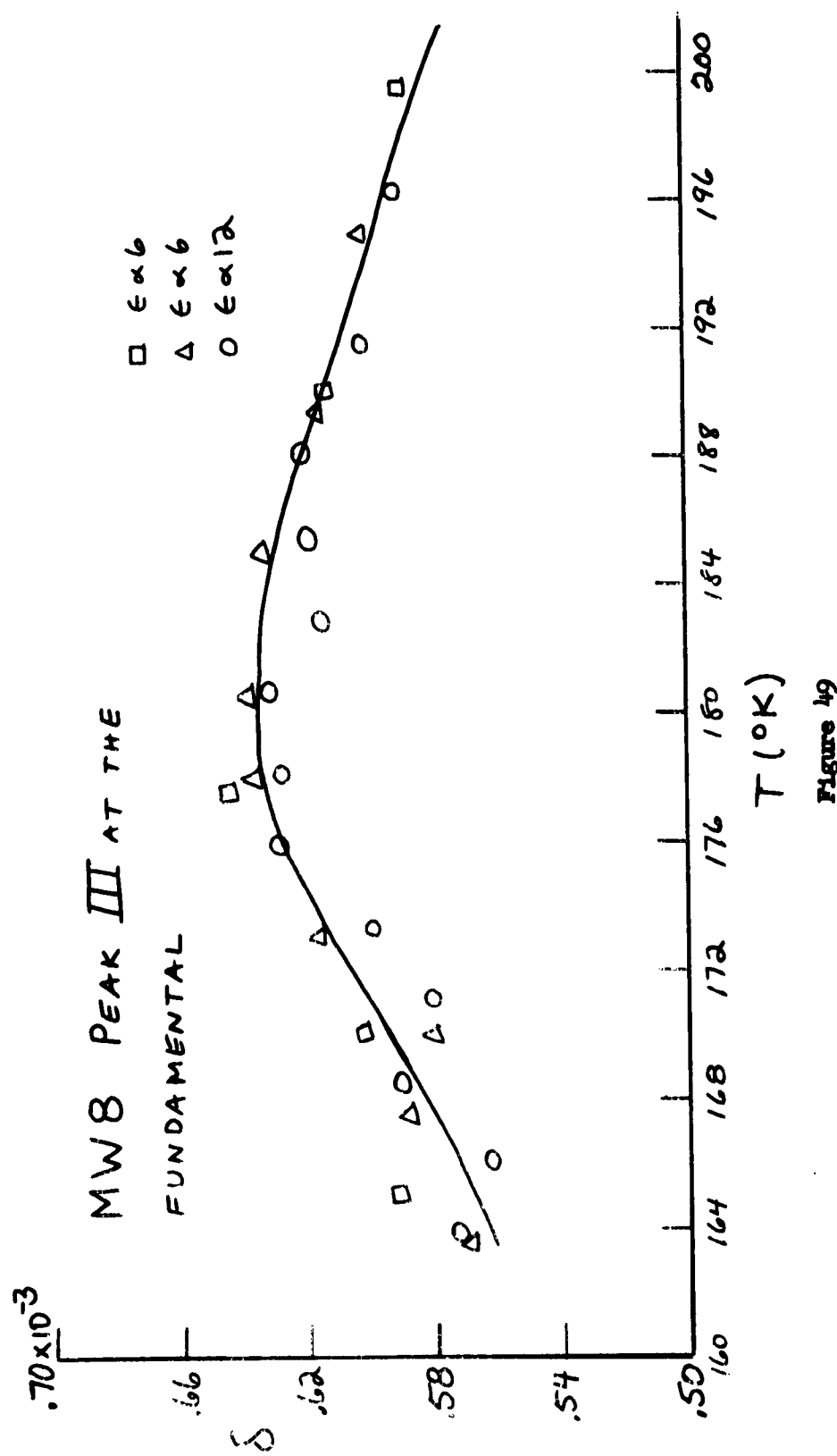


Figure 49

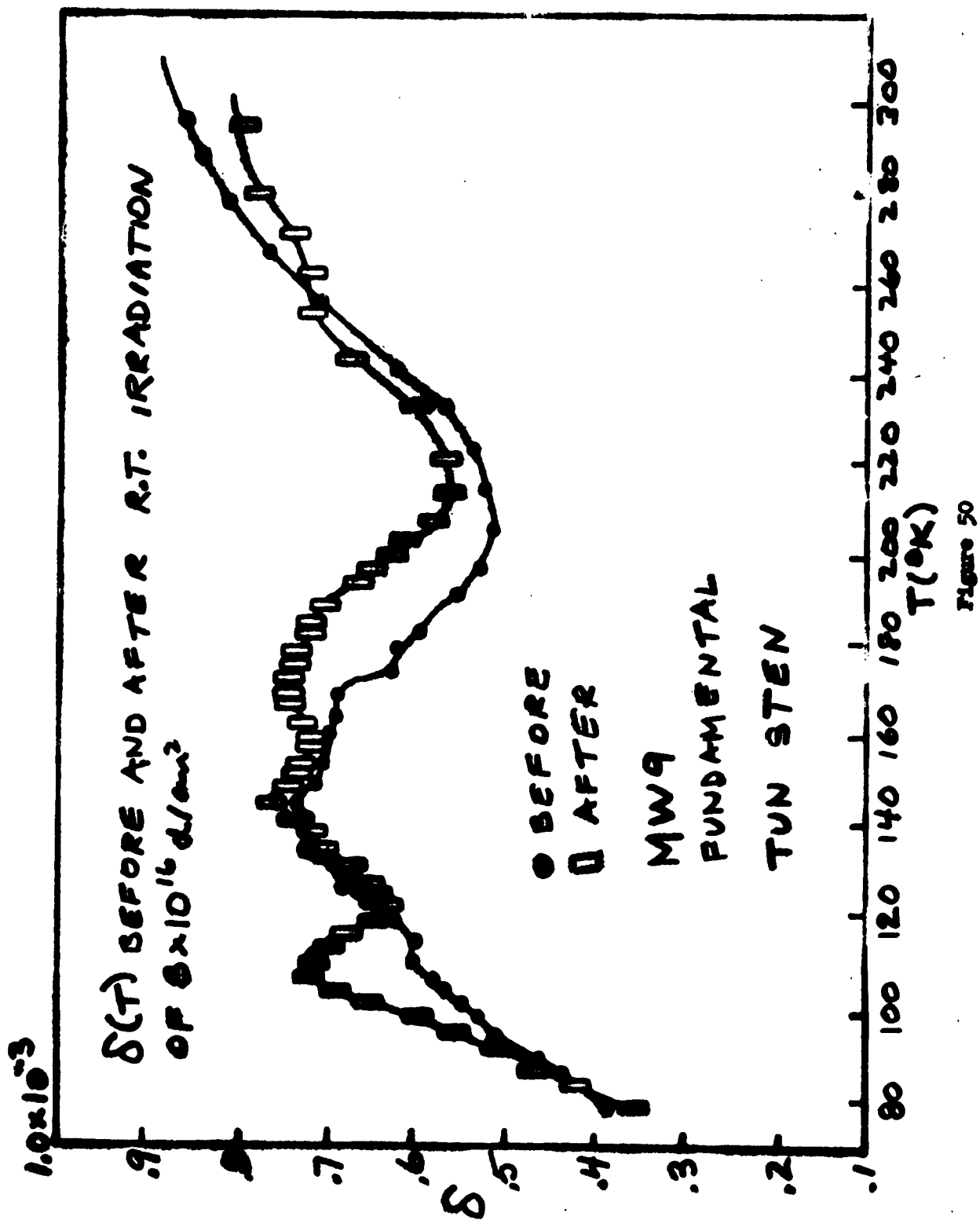


Figure 51

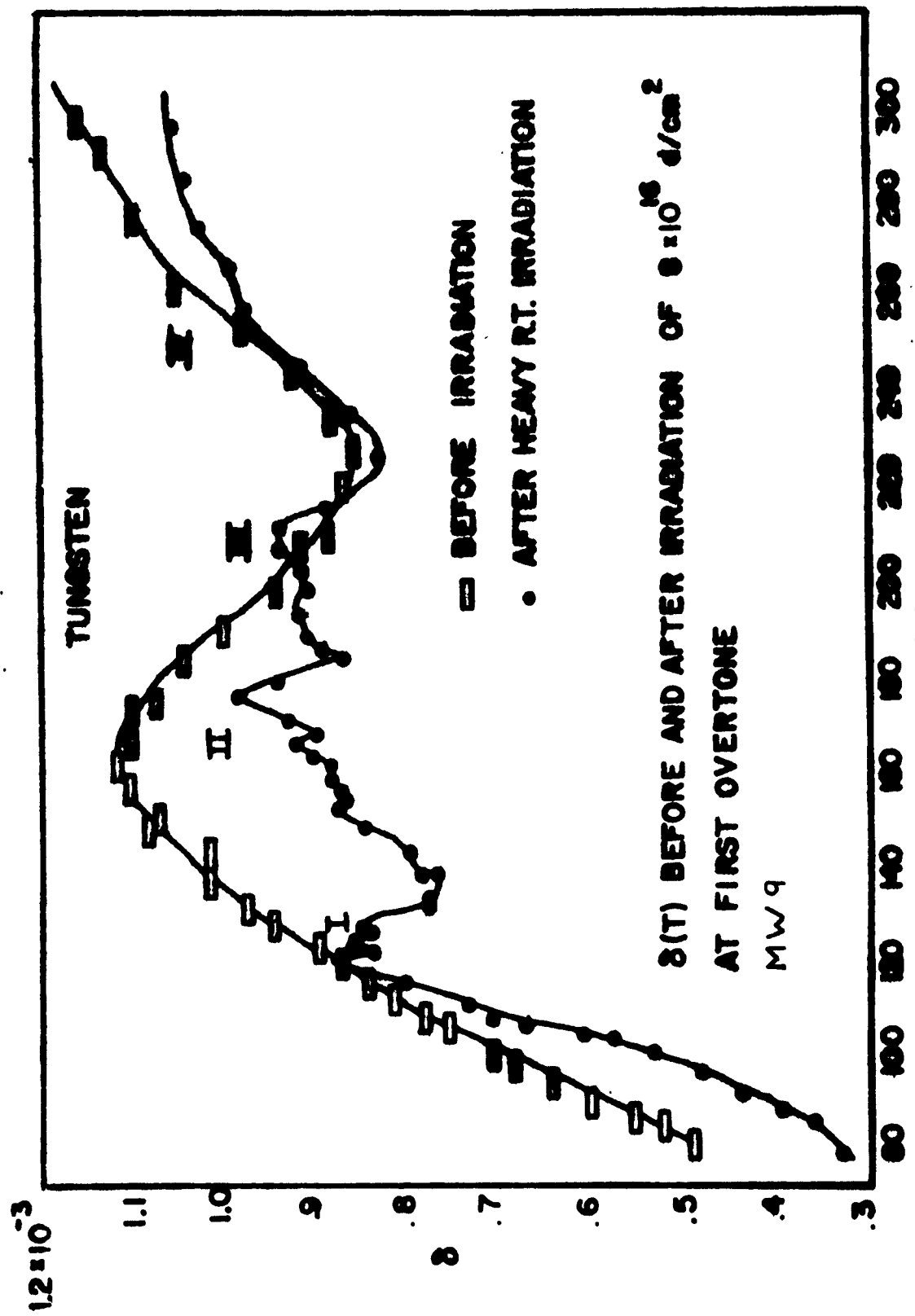
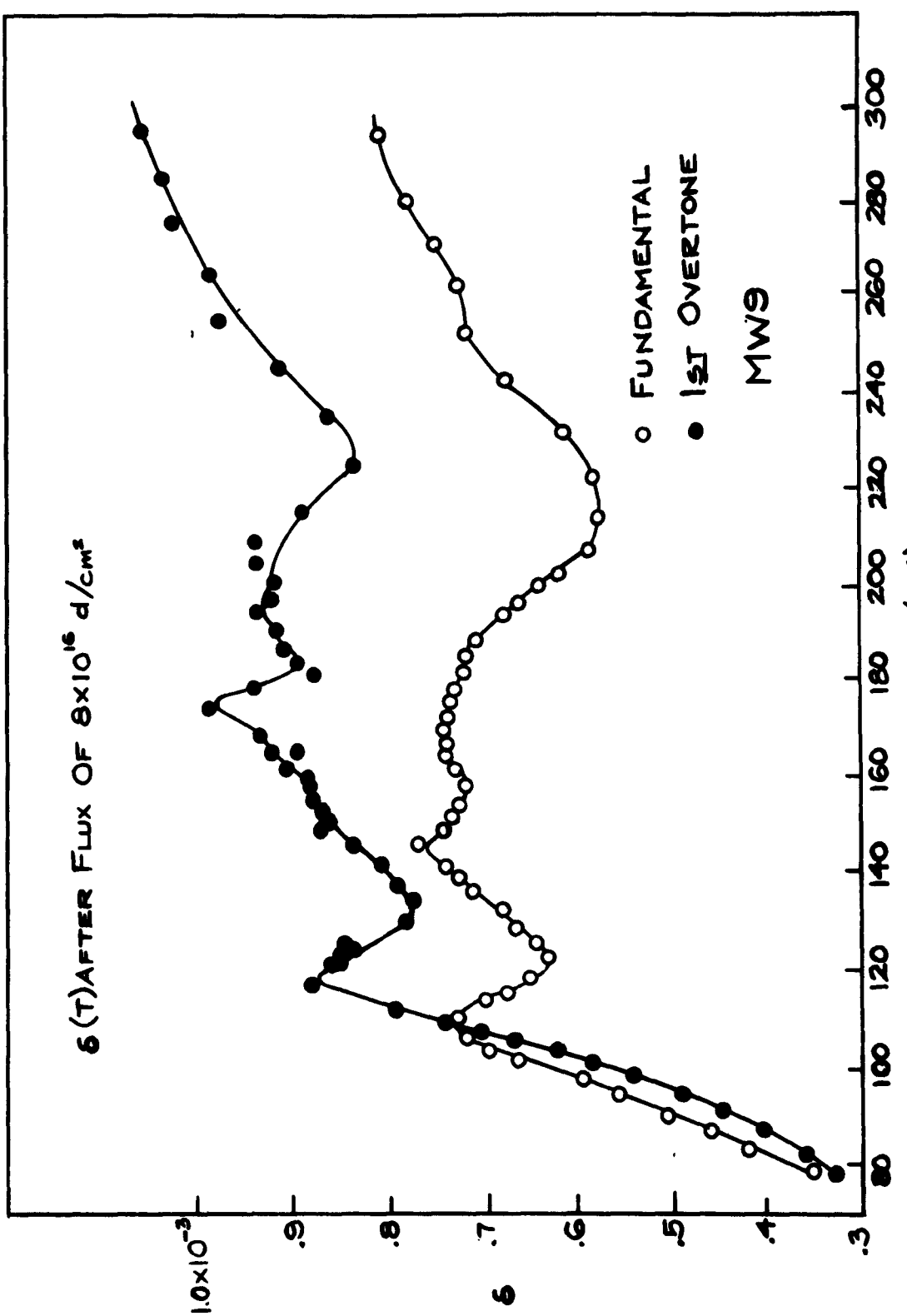


Figure 52



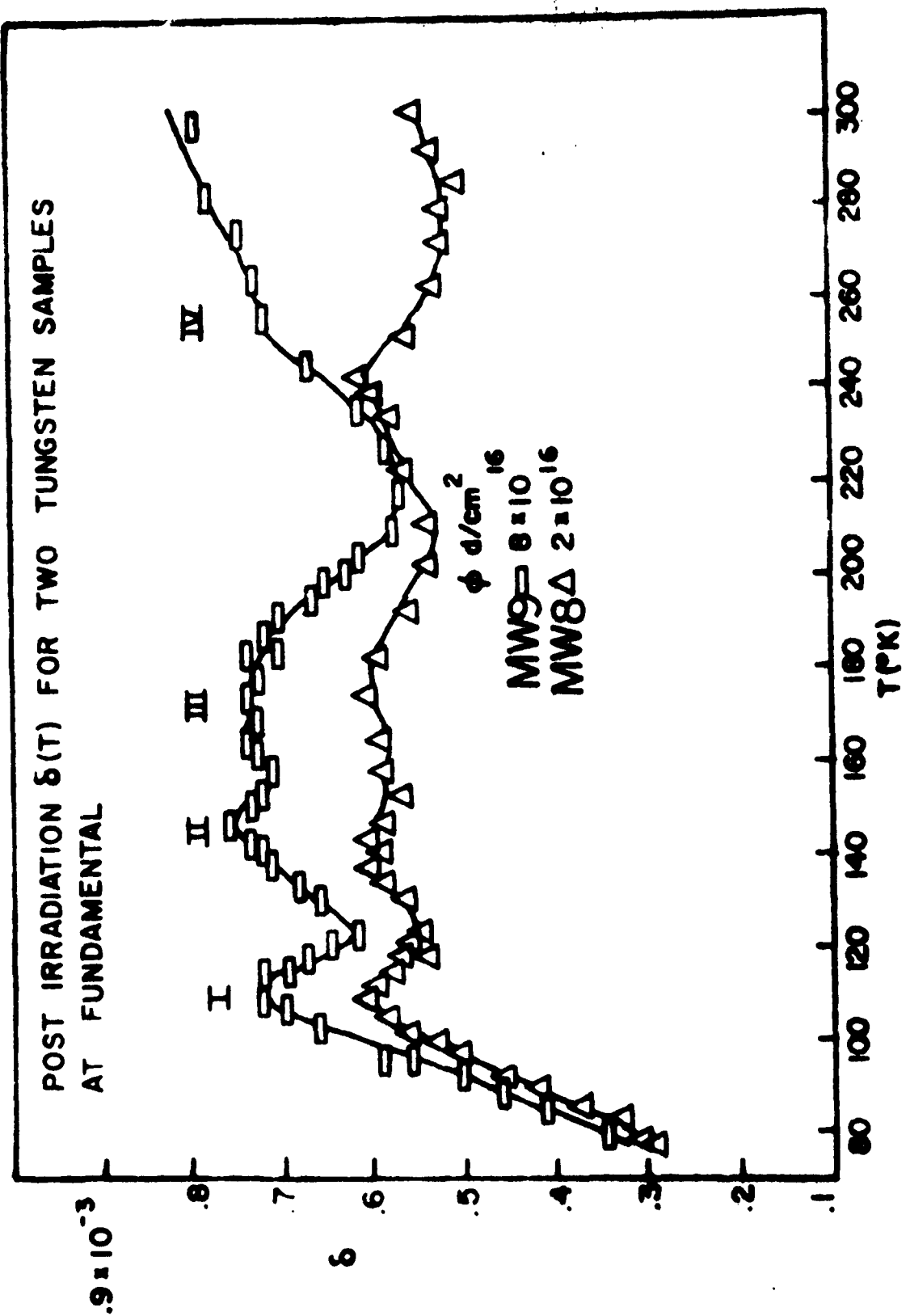


Figure 53

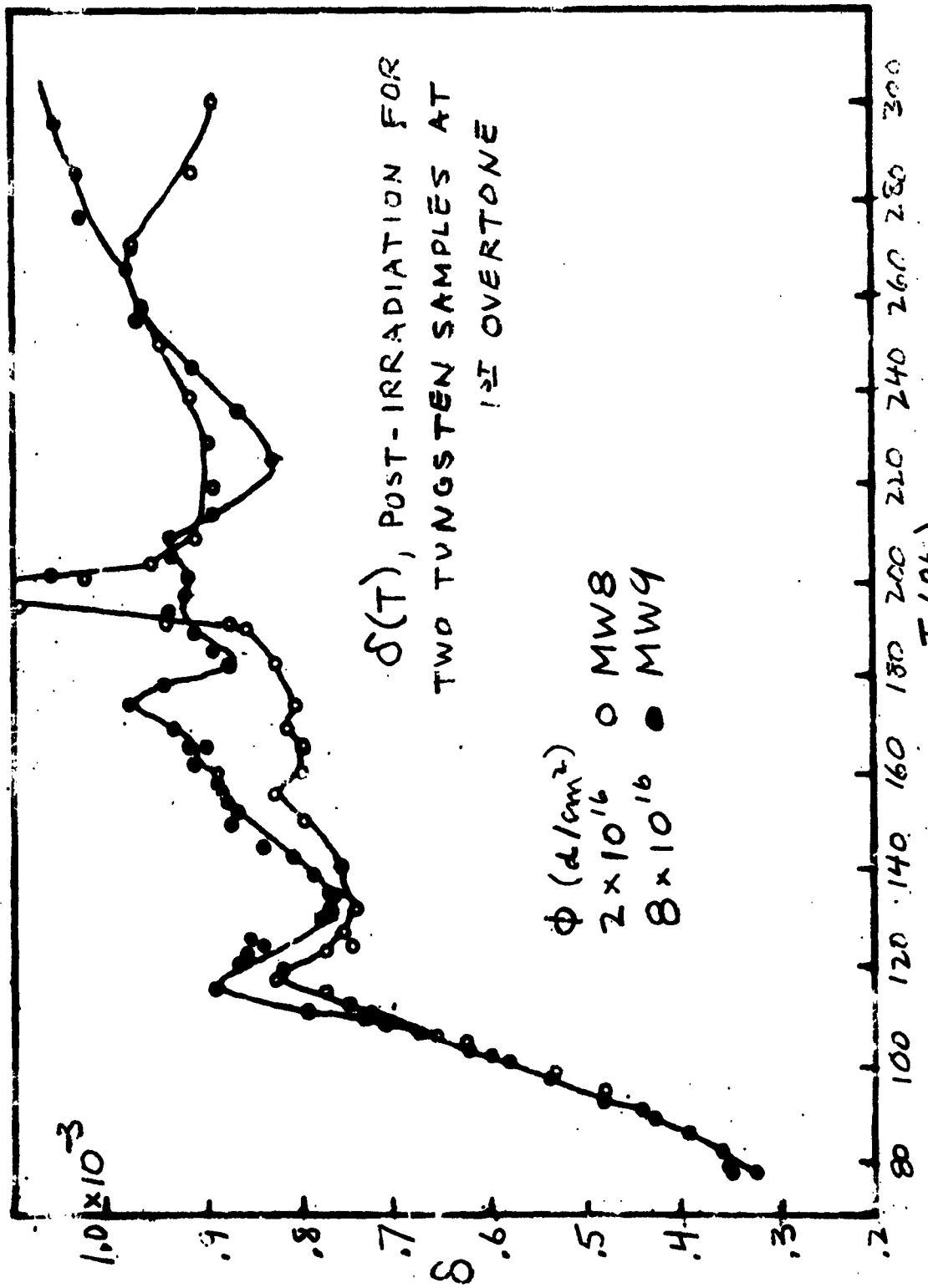


Figure 54

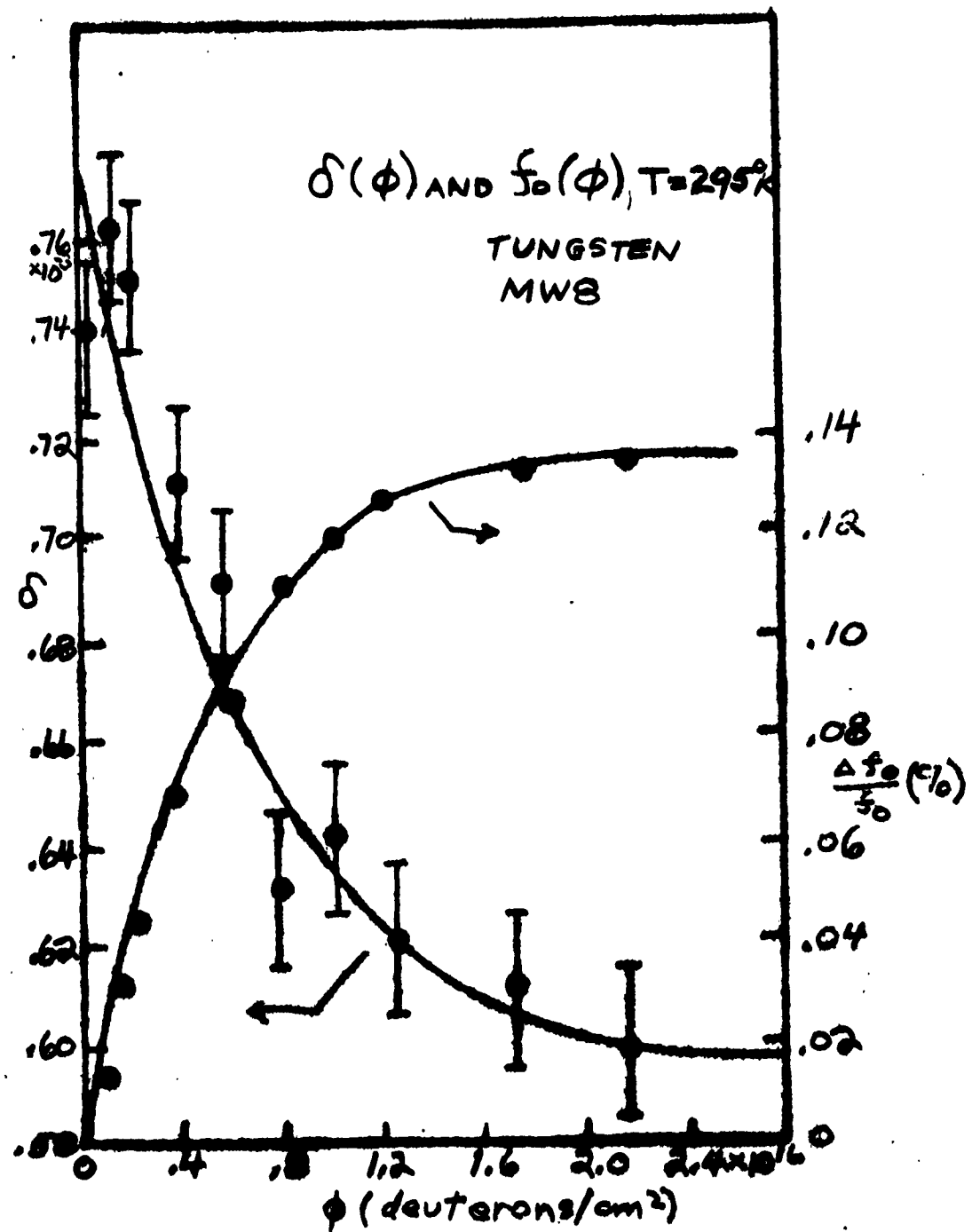
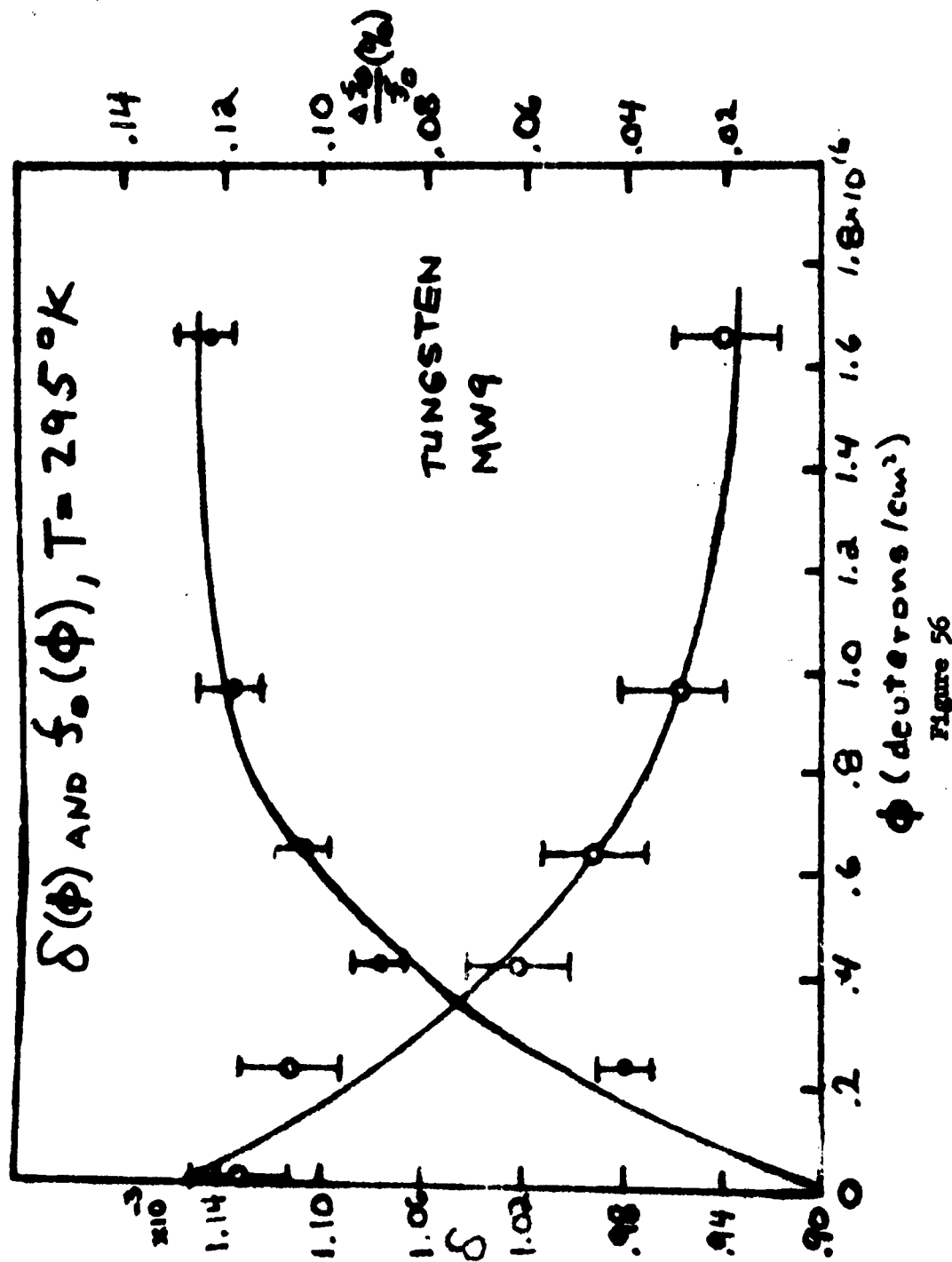


Figure 55



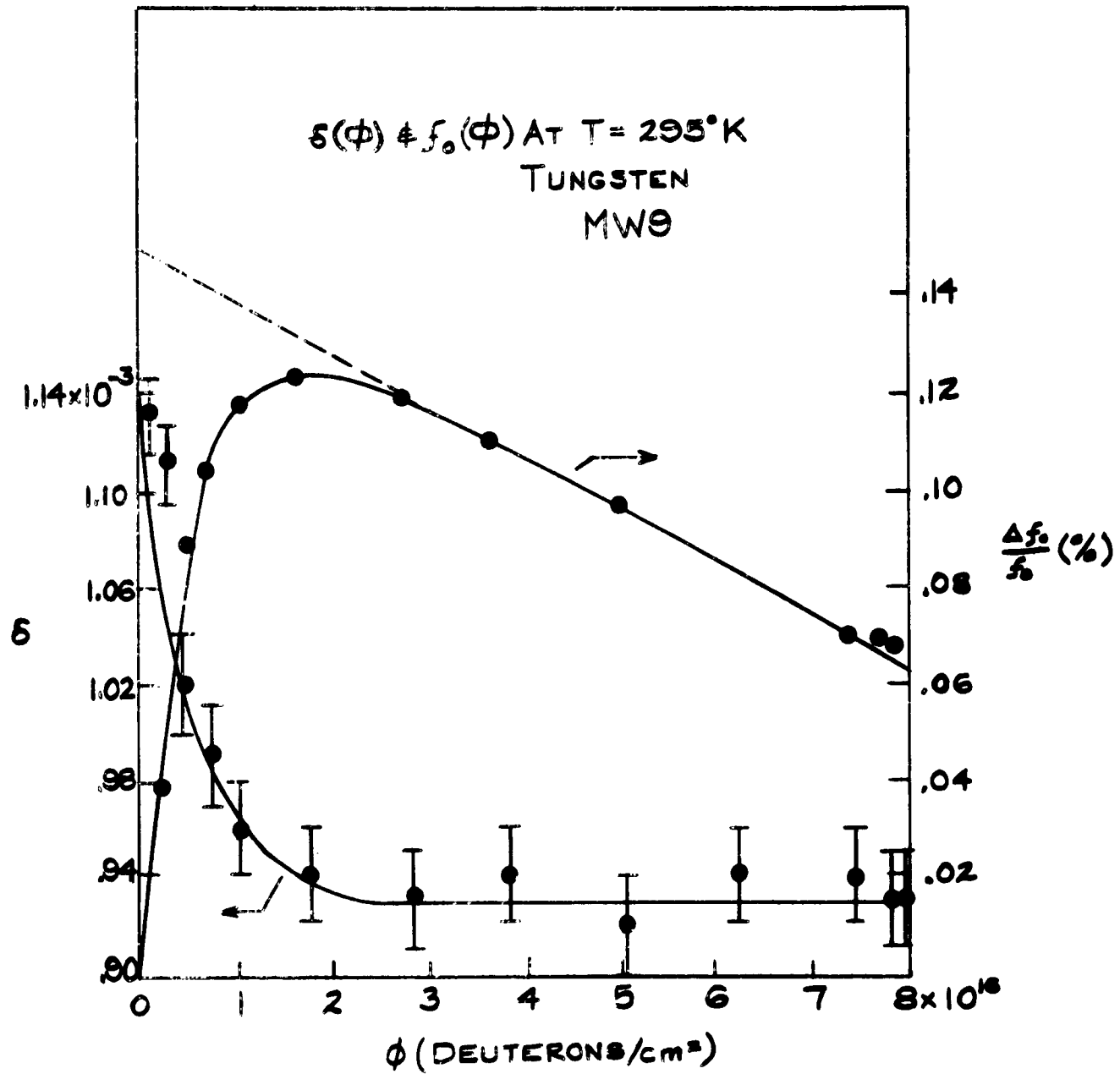


Figure 57

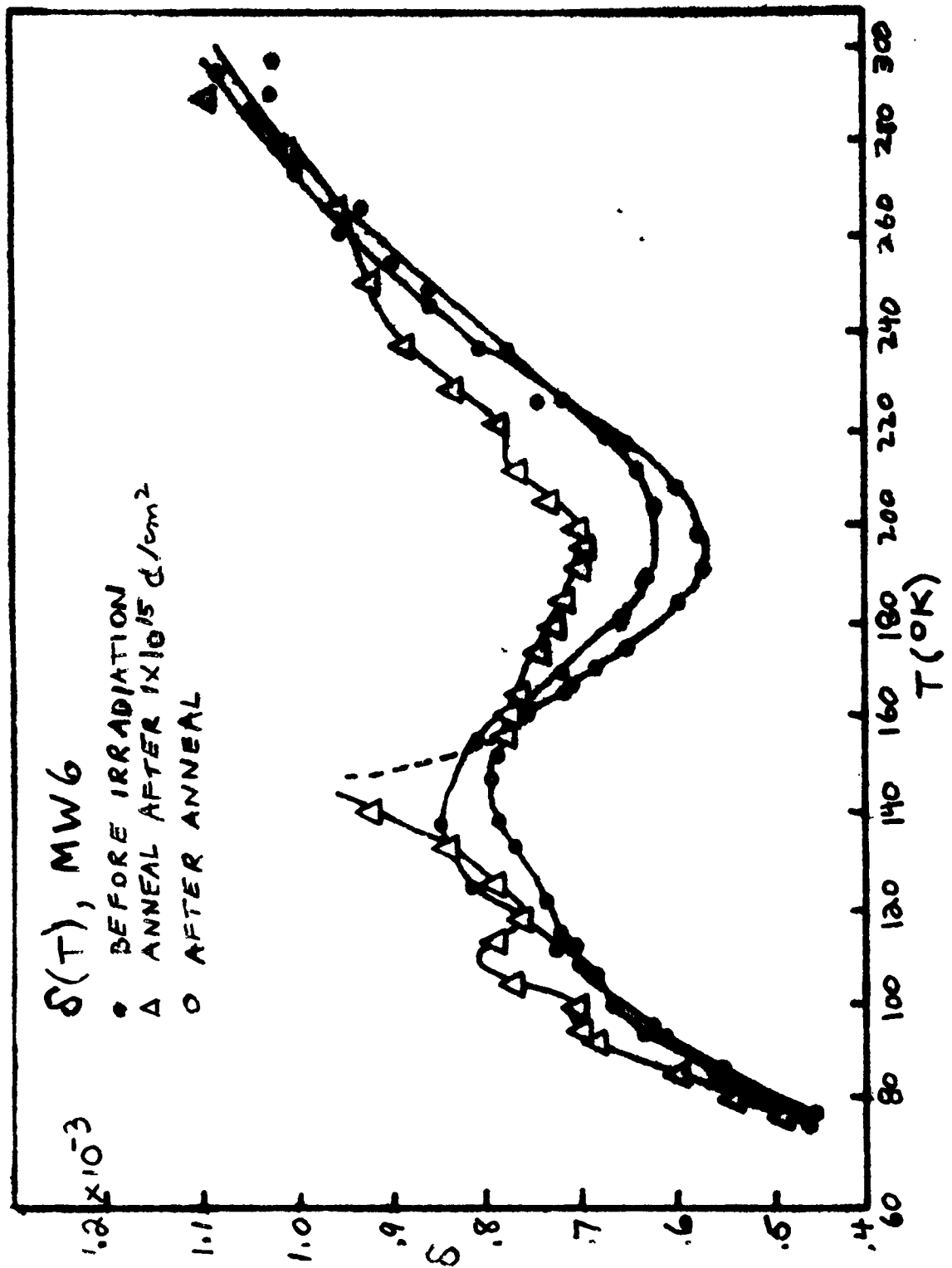
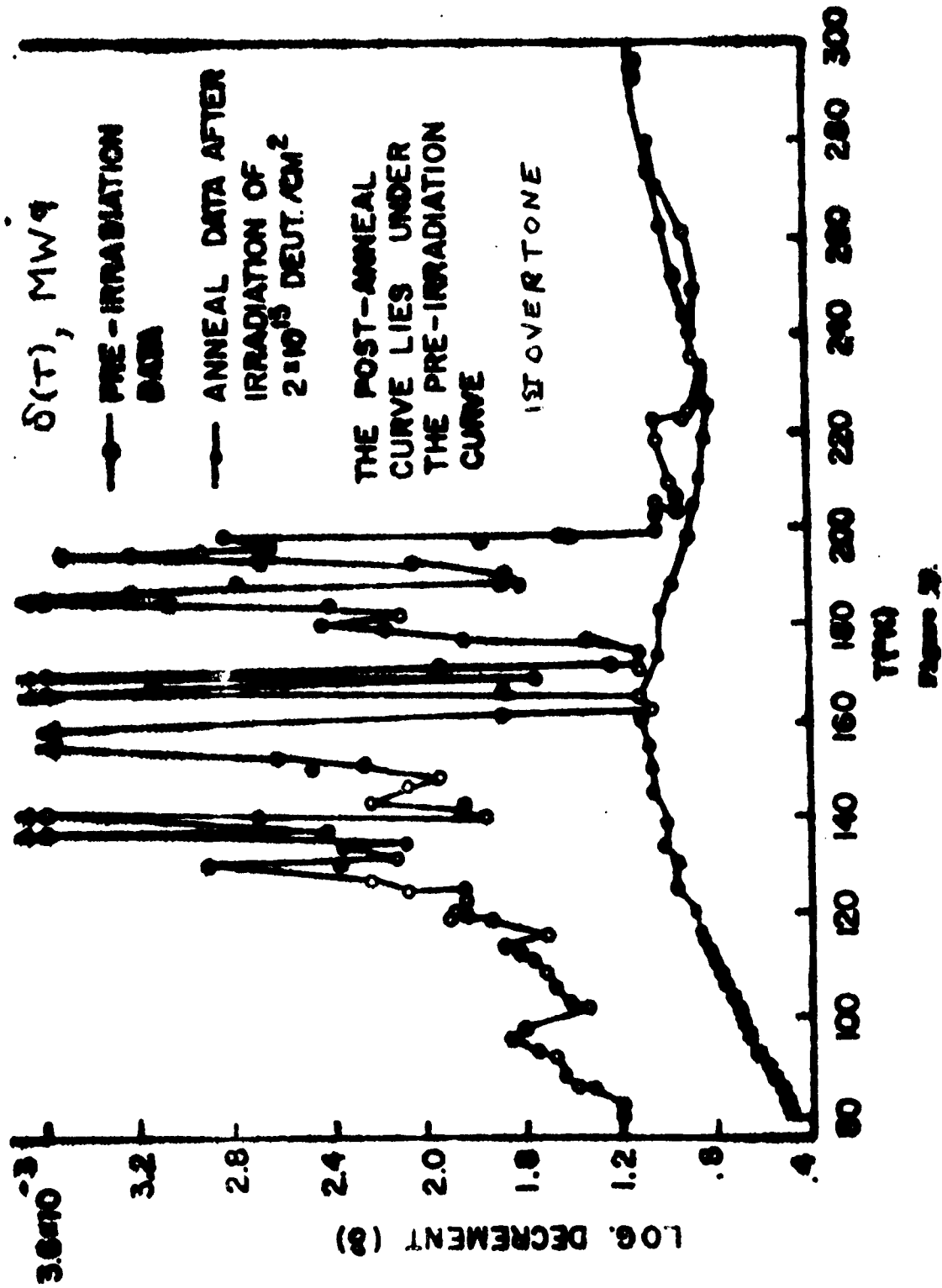


Figure 58



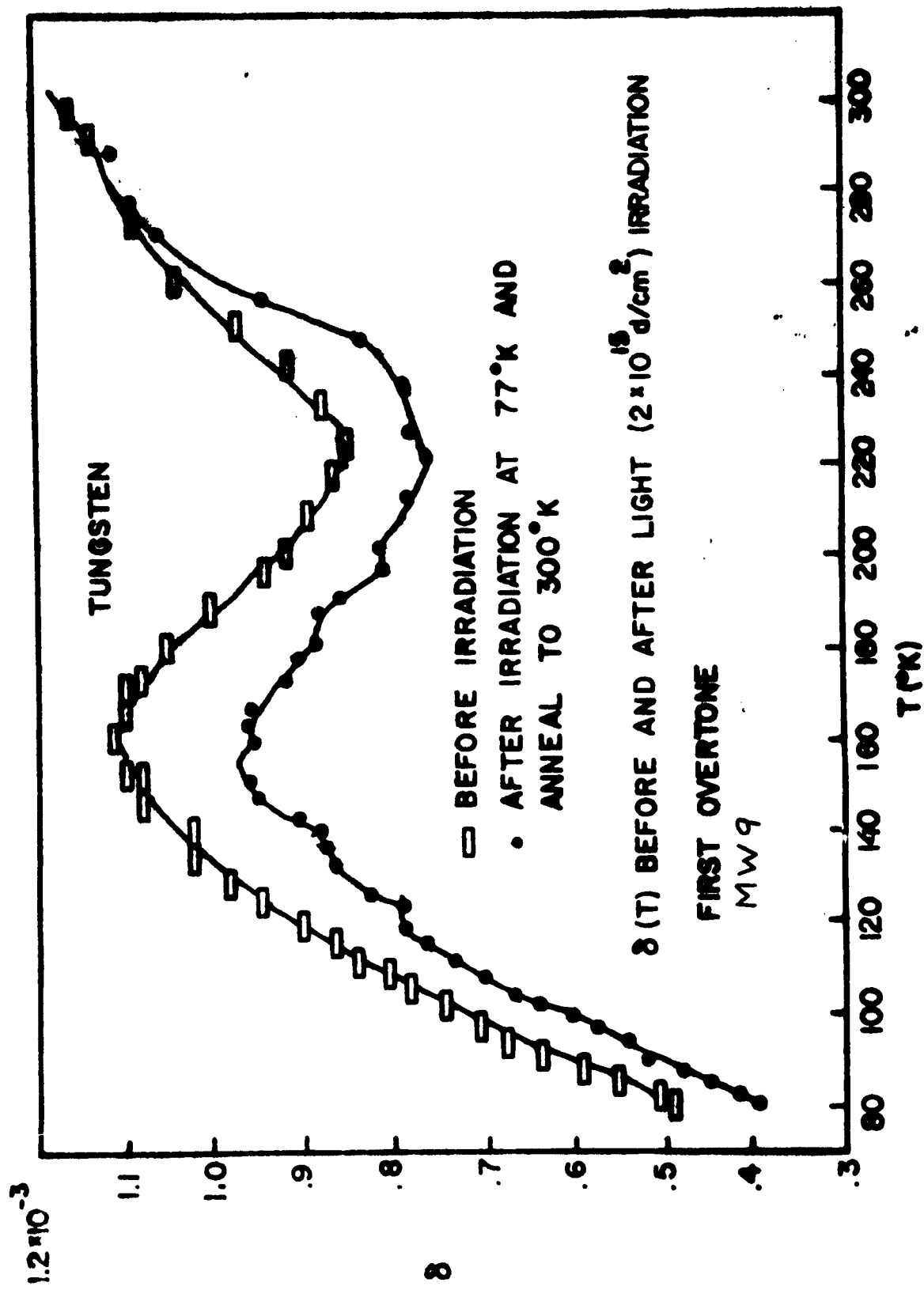
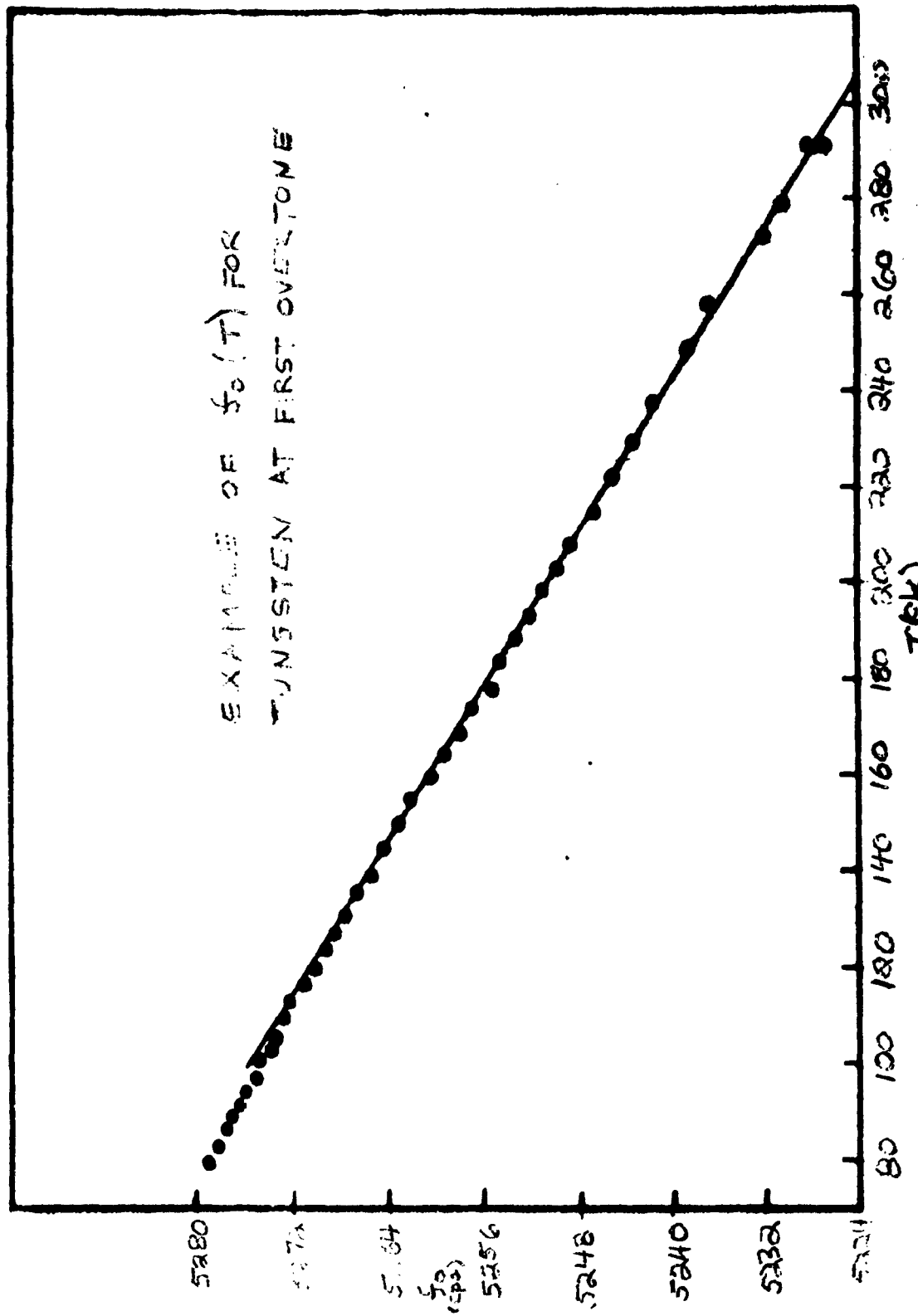


Figure 60

Figure 61



APPENDIX A

Vibration of a Cantilevered Rod

The homogeneous wave equation for a uniform rod vibrating in flexure is given by

$$\frac{\partial^4 y}{\partial x^4} + \frac{1}{\gamma^4} \frac{\partial^2 y}{\partial t^2} + g \frac{\partial y}{\partial t} = 0, \quad (1)$$

where x is the distance along the rod, y is the amplitude of flexure, g is a parameter proportional to the frictional force, and

$$\gamma^4 = \frac{\rho}{Y \kappa^2} \quad (2)$$

In equation (2) ρ is the density of the rod, Y is Young's modulus and κ , the radius of gyration for the cross sectional area, has the value $a/2$ for a circular rod of radius a . Equation (1) is separable using the relationship

$$y(x, t) = X(x) T(t). \quad (3)$$

Combining equations (3) and (1) we get that

$$\frac{1}{X} \frac{\partial^4 X}{\partial x^4} + \frac{1}{\gamma^4 T} \frac{\partial^2 T}{\partial t^2} + \frac{g}{T} \frac{\partial T}{\partial t} = 0.$$

Setting the term depending only on x equal to a constant μ^4 we get that

$$\frac{\partial^4 X}{\partial x^4} = \mu^4 X, \quad (4)$$

and

$$\frac{\partial^2 T}{\partial t^2} + g \gamma^4 \frac{\partial T}{\partial t} + \mu^4 \gamma^4 T = 0. \quad (5)$$

Morse³³ solves equation (4) for the case of a cantilevered rod of length l .

He gets allowed solutions subject to the following eigenvalue equation:

$$1 + \cos \mu_n l \cosh \mu_n l = 0. \quad (6)$$

The eigenvalues $\mu_n l$ are

$$\begin{aligned} \mu_1 l &= 1.8751, \\ \mu_2 l &= 4.6941, \quad \text{etc.} \end{aligned} \quad (7)$$

Turning to equation (5), we look for time dependent solutions of the form e^{at} , where $a = i\omega_n - \lambda$:

$$\alpha^2 + g \gamma^4 \alpha + \mu^4 \gamma^4 = 0. \quad (8)$$

The real part of equation (8) gives

$$-\omega_n^2 + \lambda^2 - \lambda g \gamma^4 + \mu_n^4 \gamma^4 = 0, \quad (9)$$

and the imaginary part gives

$$\lambda = g \gamma^4 / 2. \quad (10)$$

³³P. M. Morse, Vibration and Sound, McGraw-Hill Book Company, Inc., New York, 1948, p. 158.

Combining equations (9) and (10) we get that

$$\mu_m^4 = \frac{1}{\gamma^4} (\omega_m^2 + \lambda^2), \quad (11)$$

where $f_n = \omega_n/2\pi$ is the vibration frequency associated with the n^{th} allowed mode. For our system $\omega^2 \sim 10^7$ and $\lambda^2 \sim 1$. We therefore approximate equation (11) by

$$\mu_m^4 \gamma^4 = \omega_m^2. \quad (12)$$

Combining equations (2), (7) and (12) we get the allowed frequencies to be

$$f_1 = \frac{.55966}{\ell^2} \left(\frac{\gamma \omega^2}{4\rho} \right)^{1/2}, \quad (13)$$

$$f_2 = 6.267 f_1, \quad ,$$

$$f_3 = 17.548 f_1, \text{ etc.}$$

The logarithmic decrement (δ) is defined as the logarithm of the ratio of the amplitude of the j^{th} cycle to the amplitude of the $(j+1)^{\text{th}}$ cycle. Therefore

$$\delta = \ln \frac{e^{-\lambda j T_m}}{e^{-\lambda(j+1)T_m}} = \frac{2\pi\lambda}{\omega_m}. \quad (14)$$

We now consider the case of a sinusoidally driven rod.

Equation (1) is now written as

$$\frac{d^4 y}{dx^4} + \frac{1}{\gamma^4} \frac{d^2 y}{dt^2} + g \frac{dy}{dt} = C(x) e^{i\omega t}, \quad (15)$$

where $C(x)$ is proportional to the driving force. We now look for a solution of the form

$$y(x, t) = X(x) e^{i\omega t}. \quad (16)$$

Combining equations (15) and (16) we get that

$$\frac{d^4 X}{dx^4} - \frac{\omega^2}{\gamma^4} X + i\omega g X = C(x) \quad (17)$$

Morse³³ shows that the eigenfunction solutions X_n of the equation

$$\frac{d^4 X_n}{dx^4} = \mu_n^4 X_n \quad (18)$$

are orthogonal functions. We may therefore expand $X(x)$ and $C(x)$ in a series of characteristic eigenfunctions:

$$X(x) = \sum h_n X_n(x), \quad (19)$$

$$C(x) = \sum c_n X_n(x), \quad (20)$$

where

$$c_n = \int_0^L C(x) X_n(x) dx.$$

³³op. cit., P. M. Morse.

Combining equations (17), (18), (19) and (20) we get that

$$\sum h_m \mu_m^4 X_m - \frac{\omega^2}{\gamma^4} \sum h_m X_m + i\omega g \sum h_m X_m = \sum c_m X_m,$$

or

$$h_m = \frac{c_m}{\mu_m^4 - \omega^2/\gamma^4 + i\omega g} . \quad (21)$$

Therefore, equations (12), (16) and (21) give

$$y(x, t) = e^{i\omega t} \sum \frac{\gamma^4 c_m X_m(x)}{\omega_m^2 - \omega^2 + i\omega g \gamma^4} . \quad (22)$$

For ω near ω_n , only c_n will be important and the frequency dependence of y can be written

$$|y| = \frac{K}{[(\omega_n^2 - \omega^2)^2 + (\omega g \gamma^4)^2]^{1/2}} \quad (23)$$

We define Q as

$$Q = \frac{f_m}{f_2 - f_1} = \frac{\omega_m}{\omega_2 - \omega_1} ,$$

where ω_1 and ω_2 are such that $|y(\omega_1 \text{ or } 2)| = (1/\sqrt{2})|y(\omega_n)|$. Let $\delta\omega = \omega_2 - \omega_n = \omega_n - \omega_1$. Then, for $\delta\omega$ small compared with ω_n , equation (23) gives

$$2\omega_m \delta\omega_m = \omega_m g \gamma^4 ,$$

or

$$\frac{1}{Q} = \frac{g\gamma^4}{\omega_n^4} \quad (24)$$

Combining equations (10), (14) and (24) we get that

$$\delta = \frac{\pi}{Q} \quad . \quad (25)$$

For a system with small damping the resonance can be described by using the variable $\Delta\omega = \omega - \omega_n$, and equation (23) reduces to

$$|y| = \frac{A}{[(\Delta\omega)^2 + \lambda^2]^{1/2}} \quad) \quad (26)$$

where A depends on the amplitude of the driving force and the resonant frequency.

APPENDIX B

The Relaxation Process

Following Zener¹⁰ we note that the behavior of a solid shown in figure 4 is described by the following equation of motion:

$$\sigma + \tau_\epsilon \frac{d\sigma}{dt} = M_R (\epsilon + \tau_\sigma \frac{d\epsilon}{dt}) . \quad (1)$$

Here τ_ϵ is the relaxation time constant of the stress for constant strain, τ_σ is the relaxation time constant of the strain for constant stress, and M_R is the completely relaxed elastic modulus. We apply a stress $\sigma_0 e^{i\omega t}$ and expect the solution for ϵ to be of the form $\epsilon_0 e^{i\omega t}$. Equation (1) then gives

$$\sigma_0 (1 + i\omega \tau_\epsilon) = M_R \epsilon_0 (1 + i\omega \tau_\sigma).$$

The complex modulus $\tilde{M} = \sigma/\epsilon$ is just

$$\tilde{M} = M_R \frac{1 + i\omega \tau_\sigma}{1 + i\omega \tau_\epsilon} = M_R \frac{1 + \omega^2 \tau_\epsilon \tau_\sigma + i\omega(\tau_\sigma - \tau_\epsilon)}{1 + \omega^2 \tau_\epsilon^2} .$$

We know from equation (14) of the Introduction that the damping is given by

$$\phi = \frac{\text{imaginary part of } \tilde{M}}{\text{real part of } \tilde{M}} .$$

¹⁰ op. cit. C. Zener.

Therefore we may write that

$$\phi = \frac{\omega(\tau_\sigma - \tau_e)}{1 + \omega^2 \tau_\sigma \tau_e} . \quad (2)$$

Zener defines a quantity M_U which is the unrelaxed modulus, that is, $\Delta\sigma/\Delta\varepsilon$ for a time so short that no relaxation can take place. It can be seen by integrating equation (1) over a time δt and letting δt approach zero that $M_U/M_R = \tau_0/\tau_e$. We may define average values of M and τ such that

$$\bar{M} = (M_U M_R)^{1/2} ,$$

and

$$\bar{\tau} = (\tau_\sigma \tau_e)^{1/2} .$$

Equation (2) may then be written

$$\phi = \frac{M_U - M_R}{\bar{M}} \frac{\omega \bar{\tau}}{1 + (\omega \bar{\tau})^2} .$$

APPENDIX C

Low Temperature Vacuum Tight Seal for Aluminum Foil to Copper

The following procedure was used to cement aluminum foils over the beam entrance and exit windows in the copper sample can. These vacuum tight seals withstood pressure cycling between vacuum and one atmosphere, and temperature cycling between 77 and 300°K. The first foils used were pure aluminum. These could stand temperature cycling indefinitely, but they would leak after 3 or 4 pressure cycles. Later a commercial aluminum alloy Duraluminum was used that withstood temperature and pressure cycling indefinitely. The cement used was Araldite 502 epoxy resin with hardener Araldite HN951 supplied by Ciba Inc. The cementing technique went as follows.

(1) The window foils were cut to size and washed in acetone and then alcohol. The copper was buffed with steel wool and then washed with alcohol.

(2) About one gram of epoxy was weighed out to $\pm 1\%$ accuracy. (Let this weight be called W.) An amount of pure, finely milled talc, equal in weight to about .3 W, was added to the resin.

(3) The resin was warmed on a hot plate to about 50°C and the talc mixed with the resin. The mixture was then allowed to cool to room temperature.

(4) The hardener was then added to the resin-talc mixture in the range of weights .06 W to .10 W.

The hardener was stirred into the resin carefully to

minimize bubbling and the epoxy was ready for application. For this amount of epoxy, the pot life is about 1/2 hour.

(5) The epoxy was applied to the copper in a layer about .01 inches thick, and the foil was laid in place with tweezers. The foil was held firmly in place with commercial plastic insulating tape. (The length of tape bearing on the foil was made with the plastic tape back to back. Araldite will not adhere to polyvinyl chloride.)

(6) The sample can was then baked in air at 40-50°C for 12 hours. After baking, the can was cleaned with benzene and then alcohol to remove the tape adhesive.

The Araldite epoxy resin with a talc filler could withstand temperatures greater than 100°C. All soldering operations were done with Nichrome metal which melts at about 80%.

APPENDIX D

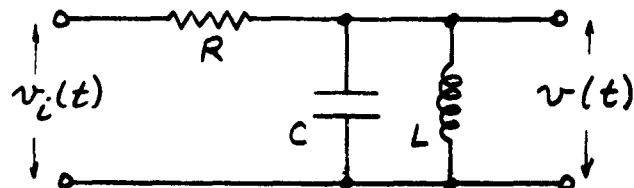
Effect of an RLC Filter on the Transient Signal

We know that when the sample vibration starts its decay the electrical signal from the transducer will be affected by the RLC filter which is tuned to pass the resonant frequency. The filter is expected to reject the higher frequency components of the input signal introduced by the discontinuity at the start of the transient. One also might expect that this filter effect will be negligible after a time $4\tau_f$, where τ_f is the time constant of the filter in a free decay. This in fact what is indicated by the following calculation.

Let us approximate the real filter by assuming that the inductance has zero resistance. The filter circuit shown is then described by

$$\alpha_f \ddot{v}_i(t) = \ddot{v}(t) + \alpha_f \dot{v}(t) + \omega_0^2 v(t), \quad (1)$$

where $\alpha_f = 1/\tau_f = 1/RC$, $\omega_0^2 = 1/LC$, and v and v_i are the output and input voltage signals respectively.



The input signal is

$$v_i(t) = \mathcal{V} e^{-\alpha t} \sin \omega_0 t, \quad (2)$$

and the boundary conditions are that at $t = 0$:

$$\begin{aligned} v_i(0) &= 0, & v(0) &= \bar{v}_i(0), \\ \dot{v}_i(0) &= \mathcal{V}\omega_0, & \dot{v}(0) &= \dot{\bar{v}}_i(0). \end{aligned} \quad (3)$$

Let $V(p)$ be the Laplace transform of $v(t)$. Then the transform⁴³ of equation (1) is

$$\begin{aligned} p^2 V(p) - p v(0) - \dot{v}(0) + \alpha_f p V(p) - \alpha_f v(0) \\ + \omega_0^2 V(p) = \alpha_f p \bar{V}_i(p) - \alpha_f \bar{v}_i(0) \end{aligned} \quad (4)$$

The transform⁴³ of the input signal is

$$\bar{V}_i(p) = \mathcal{V} \frac{\omega_0}{(p + \alpha_f)^2 + \omega_0^2}. \quad (5)$$

Combining equations (3), (4) and (5) we get the expression for the output voltage transform:

$$V(p) = \omega_0 \mathcal{V} \left\{ \frac{1}{p^2 + \alpha_f p + \omega_0^2} + \alpha_f \frac{p}{(p^2 + \alpha_f p + \omega_0^2)[(p + \alpha_f)^2 + \omega_0^2]} \right\} \quad (6)$$

⁴³G. Doetsch, Tabellen zur Laplace-Transformation und Anleitung zum Gebrauch, Springer-Verlag, Berlin, 1947.

A transform of the form

$$f(p) = \frac{\lambda_1 p^{n-1} + \lambda_2 p^{n-2} + \dots + \lambda_n}{(p+a_1)(p+a_2)\dots(p+a_n)} \quad (7)$$

has the inverse transform⁴³

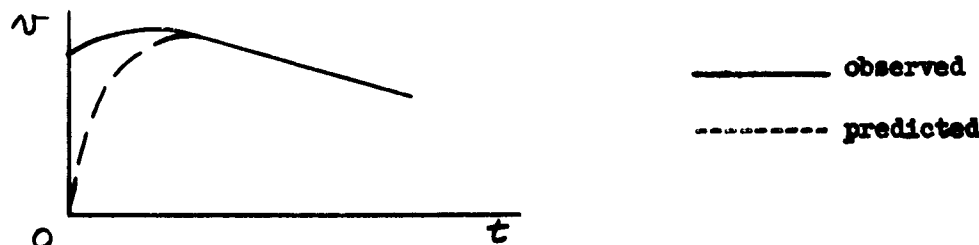
$$f(t) = \frac{\lambda_1(-a_1)^{n-1} + \lambda_2(-a_1)^{n-2} + \dots + \lambda_n}{(a_2-a_1)(a_3-a_1)\dots(a_n-a_1)} e^{-a_1 t} + \begin{matrix} (n-1) \text{ terms obtained} \\ \text{by cyclic} \\ \text{permutation of} \\ a_1 \dots a_n \end{matrix} \quad (8)$$

Equations (7) and (8) were used to find $v(t)$ from equation (6).

Using the fact that for our problem $a_f \sim 10^2$, $a \sim 1$ and $\omega_0 \sim 6 \times 10^3 \text{ sec}^{-1}$, we get simply that

$$v(t) = \mathcal{V} (e^{-\alpha t} - e^{-\alpha_f t}) \sin \omega_0 t. \quad (9)$$

The envelope of this result (equation (9)) is compared with the observed waveform in the sketch below



The lack of agreement near $t = 0$ is undoubtedly due to the approximation made in neglecting the resistance of the inductor. This result does show, however, that the effect of the filter is negligible after $t = 4/\tau_f$.

⁴³Op. cit., G. Doetsch.

APPENDIX E

Correction for the Energy Loss in the Sample

The quantity we measure in the energy dependence study is $\Delta R/R_0$, the fractional change in the electrical resistance of the sample wire. We assume that the resistivity of the sample material will change with bombardment according to

$$\rho = \rho_0 + \frac{\alpha}{E} , \quad (1)$$

where α depends on the incident flux and can be determined for the purposes of this correction from the uncorrected energy dependence data. The quantity E , the energy of the bombarding particle, will vary with position in the sample wire because of ionization losses. The conductance of a uniform wire is

$$\frac{1}{R} = \frac{1}{I} \int \frac{dA}{\rho} ,$$

where dA is an element of the wire's cross section. Then

$$\frac{\Delta R}{R_0} = \frac{R - R_0}{R_0} = \int \frac{\rho - \rho_0}{\rho \rho_0} dA / \int \frac{dA}{\rho} . \quad (2)$$

Using equation (1), equation (2) may be written

$$\frac{\Delta R}{R_0} = \int \frac{\alpha' dA}{E + \alpha'} / \int \frac{E dA}{E + \alpha'} , \quad (3)$$

where $\alpha' = \alpha/\rho_0$.

We define E_f as the energy that would produce this same fractional resistance change if the energy of the incident particle was constant in passing through the sample. From equation (3), for a constant energy E_f we get that

$$\frac{\Delta R}{R_0} = \frac{\alpha'}{E_f},$$

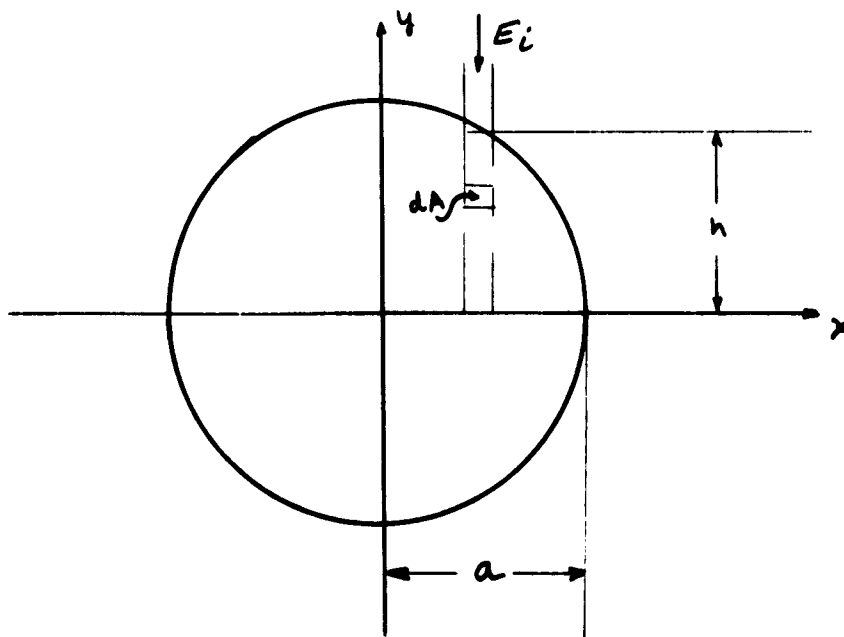
so that

$$E_f = \int \frac{E dA}{E + \alpha'} / \int \frac{dA}{E + \alpha'} = \frac{N}{D}. \quad (4)$$

For the case of a sample wire of circular cross section

$$E = E_i - \frac{dE}{dy} (h - y), \quad (5)$$

$$h = (a^2 - x^2)^{1/2}.$$



The denominator D of equation (4) is then

$$D = \int_{-a}^a \int_{-h}^h \frac{dx dy}{E_i + \alpha' - \frac{dE}{dy}(h-y)} . \quad (6)$$

Letting $\zeta = dE/dy$ and $E'_i = E_i + \alpha'$ we may write equation (6) as

$$D = \int_{-a}^a \int_{-h}^h \frac{dx dy}{E'_i - \zeta(h-y)} . \quad (7)$$

The numerator of equation (4) is

$$N = \int_{-a}^a \int_{-h}^h \frac{E'_i - \zeta(h-y) - \alpha'}{E'_i - \zeta(h-y)} dx dy . \quad (8)$$

Carrying out these integrals we get finally that

$$E_f = E_i \frac{1 - \frac{\alpha'}{E'_i} \Lambda}{1 + \Lambda} , \quad (9)$$

where

$$\Lambda = \frac{4}{3\pi} p + \frac{1}{4} p^2 + \dots , \quad (10)$$

and

$$p = \frac{2\zeta a}{E'_i} . \quad (11)$$

The quantity p is roughly the maximum fractional energy loss of the incident particle in passing through the sample wire. It has a value of about .15 for our problem, so that the two terms given in the expansion of equation (1) are sufficient for the purposes of this correction.

BIBLIOGRAPHY

Aron, W. A., Hoffman, B. G., and Williams, F. C., Rept. AECU-663,
UCRL-121 (1949).

Barnes, R. S., and Hancock, N. H., Phil. Mag. 3, 527 (1958).

Birnbaum, H. K., and Levy, M., Acta Met. 4, 84 (1956).

Bordoni, P. G., J. Acous. Soc. Amer. 26, 495 (1954).

Brown, E., and Goldecke, G. H., J. Appl. Phys. 31, 932 (1960).

Brunner, L. J., Phys. Rev. Letters 3, 411 (1959).

Caswell, H. L., J. Appl. Phys. 29, 1210 (1958).

Chambers, R. H., and Schultz, J., Phys. Rev. Letters 6, 273 (1961).

Cooper, H. G., Koehler, J. S., and Marx, J. W., Phys. Rev. 97, 599
(1955).

Corbett, J. W., Denney, J. M., Fiske, M. D., and Walker, R. M., Phys.
Rev. 108, 954 (1957).

Corbett, J. W., Smith, R. B., and Walker, R. M., Phys. Rev. 114, 1452,
1460 (1959).

Corbett, J. W., and Walker, R. M., Phys. Rev. 115, 67 (1959).

Cottrell, A. H., Dislocations and Plastic Flow in Crystals, Clarendon
Press, Oxford, 1953.

Cottrell, A. H., Report of a Conference on the Strength of Solids,
London: Phys. Soc., p. 30, 1948.

Dieckamp, H., and Sosin, A., J. Appl. Phys. 27, 1416 (1956).

Dienes, G. J., Phys. Rev. 86, 228 (1951).

Dienes, G. J., J. Appl. Phys. 24, 666 (1953).

Dienes, G. J., and Vineyard, G. H., Radiation Effects in Solids,
Interscience Publishers Inc., New York, 1957.

Doetsch, G., Tabellen zur Laplace-Transformation und Anleitung zum
Gebrauch, Springer-Verlag, Berlin, 1947.

Donth, H., Z. Phys. 131, 156 (1957).

Filmer, A. J., Hutton, G. J., and Hutchinson, T. S., *J. Appl. Phys.* 39, 146 (1958).

Harwood, J. J., Hausner, H. H., Morse, J. G., Rauch, W. G., The Effects of Radiation on Materials, Reinhold Publishing Co., New York, 1958.

Kinchin, G., and Thompson, M. W., *J. Nuclear Energy* 6, 275 (1958).

Koehler, J. S., *Bull. Am. Phys. Soc.* 5, 175 (1960).

Magnuson, G. D., Palmer, W., and Koehler, J. S., *Phys. Rev.* 109, 1990 (1958).

Morse, P. M., Vibration and Sound, McGraw-Hill Book Company, Inc., New York, 1948.

Miblett, D. H., and Wilks, J., *Adv. in Phys.* 9, 1 (1960).

Miblett, D. H., and Wilks, J., *Phil. Mag.* 3, 527 (1958).

Nowick, A. S., *Progress in Metal Physics* 4, 1 (1953).

Nowick, A. S., *Phys. Rev.* 82, 340(A) (1951).

Pearlstein, E. A., Ingraham, H., and Smoluchowski, R., *Phys. Rev.* 96, 1530(A) (1955).

Read, T. A., *Phys. Rev.* 58, 371 (1940).

Seeger, A., *Phil. Mag.* 1, 651 (1956).

Seitz, F., and Koehler, J. S., *Solid State Physics* 2, 316 (1956).

Thompson, D. O., and Holmes, D. K., *J. Appl. Phys.* 27, 713 (1956).

Thompson, D. O., and Holmes, D. K., *J. Appl. Phys.* 30, 525 (1959).

Thompson, M. W., *Phil. Mag.* 5, 278 (1960).

Vook, R. W., and Wert, C. A., *Phys. Rev.* 109, 1529 (1958).

Zener, C., Elasticity and Anelasticity of Metals, University of Chicago Press, Chicago, 1948.

Distribution List

<u>Code</u>	<u>Organization</u>	<u>No. of Copies</u>
AF 5	AFMTC (AFMTC Tech Library-Mu-135) Patrick AFB, Fla.	1
AF 18	AUL Maxwell AFB, Ala.	1
AF 32	OAR (PROS, Col. John R. Fowler) Tempo D 4th and Independence Ave., Wash. 25, D.C.	1
AF 43	ASD (ASAPRD - Dist) Wright-Patterson AFB, Ohio	1
AF 124	RADC (RAYLD) Griffiss AFB, New York Attn: Documents Library	1
AF 139	AF Missile Development Center (MDGRT) Holloman AFB, New Mexico	1
AF 314	Hq. OAR (PROSP, Maj. Richard W. Nelson) Washington 25, D.C.	1
AF 318	ARL (ARA-2) Library AFL 2292, Building 450 Wright-Patterson AFB, Ohio	1
Ar 5	Commanding General USASRDL Ft. Monmouth, N.J. Attn: Tech. Doc. Ctr. SIGRA/SL-ADT	1
Ar 9	Department of the Army Office of the Chief Signal Officer Washington 25, D.C. Attn: SIGRD-4a-2	1
Ar 50	Commanding Officer Attn ORDTL-012 Diamond Ordnance Fuze Laboratories Washington 25, D.C.	1
Ar 67	Redstone Scientific Information Center U.S. Army Missile Command Redstone Arsenal, Alabama	1

G 31	Office of Scientific Intelligence Central Intelligence Agency 2430 E. Street, N.W. Washington 25, D.C.	1
G 2	ASTIA (TIPAA) Arlington Hall Station Arlington 12, Virginia	30
G 68	Scientific and Technical Information Facility Attn: NASA Representative (S-K/DL) P.O. Box 5700 Bethesda, Maryland	1
G 109	Director Langley Research Center National Aeronautics and Space Administration Langley Field, Virginia	1
N 9	Chief, Bureau of Naval Weapons Department of the Navy Washington 25, D.C. Attn: DLW-31	2
N 29	Director (Code 2027) U.S. Naval Research Laboratory Washington 25, D.C.	2
I 292	Director, USAF Project RAND The Rand Corporation 1700 Main Street Santa Monica, California THRU. AF Liaison Office	1
M 6	AFCRL, OAR (CRXRA - Stop 39) L.G. Hanscom Field Bedford, Mass.	30
AF 253	Technical Information Office European Office, Aerospace Research Shell Building, 47 Centersteen Brussels, Belgium	1
Ar 107	U.S. Army Aviation Human Research Unit U.S. Continental Army Command P.O. Box 428, Fort Rucker, Alabama Attn: Maj. Arne H. Eliasson	1
G 8	Library Boulder Laboratories National Bureau of Standards Boulder, Colorado	2

M 63	Institute of the Aerospace Sciences, Inc. 2 East 64th Street New York 21, New York Attn: Librarian	1
M 84	AFCRL, OAR (CRXR, J.R. Marple) L.G. Hanscom Field Bedford, Mass.	1
N 73	Office of Naval Research Branch Office, London Navy 100, Box 39 F.P.O., New York, N.Y.	10
U 32	Massachusetts Institute of Technology Research Laboratory Building 26, Room 327 Cambridge 39, Massachusetts Attn: John H. Hewitt	1
U 431	Alderman Library University of Virginia Charlottesville, Virginia	1
G 9	Defence Research Member Canadian Joint Staff 2450 Massachusetts Avenue, N.W. Washington 8, D.C.	1
I 727	Texas Instruments, Inc. Central Research Laboratory P.O. Box 1079 Dallas 21, Texas Attn: Norman Uranson, Technical Info. Service	1
I 907	Raytheon Company - Semiconductor Division 150 California Street, Newton 58, Mass. Attn: Library	1
G 98	U.S. Atomic Energy Commission Office of Technical Information Extension P.O. Box 62 Oak Ridge, Tennessee	1